DISSERTATION

VISUALIZING DYNAMICS USING 100 KHZ 2D IR SPECTROSCOPY AND MICROSCOPY

Submitted by

Kathryn Marie Tracy

Department of Chemistry

In partial fulfillment of the requirements

For the Degree of Doctor of Philosophy

Colorado State University

Fort Collins, Colorado

Summer 2018

Doctoral Committee:

Advisor: Amber T. Krummel

Nancy E. Levinger
Grzegorz Szamel
David A. Krueger
John D. Fisk

ABSTRACT

VISUALIZING DYNAMICS USING 100 KHZ 2D IR SPECTROSCOPY AND MICROSCOPY

2D IR spectroscopy is a nonlinear optical method with the ability to characterize condensed phase chemical systems. It offers information regarding structure and dynamics of chemical systems. Recent efforts have been made to resolve spatially the molecular structure and dynamics of heterogeneous samples, which shows the feasibility of ultrafast 2D IR microscopy. To image more efficiently, we have moved away from the Ti:sapphire based laser systems and OPA systems that operate at one to several kHz typically used in 2D IR spectroscopy. Instead, for the first time we have demonstrated higher repetition rate, 2D IR spectroscopy at 100 kHz. Achieving this higher repetition rate was accomplished by utilizing advances in diode pumped ytterbium oscillators and amplifiers, and is based on an OPCPA utilizing Mg:PPLN followed by DFG in ZGP. Using this system, we have for the first time, demonstrated the interfacing of IR compatible microfluidics with 2D IR spectroscopy to examine the solvatochromic pseudo-halide anion, cyanate in cosolvent environments. This high repetition rate source also provided a path to 2D IR microscopy experiments that explore the dynamics of complex, heterogeneous, chemical systems. We have shown the chemical dynamics in a room temperature ionic liquid microdroplet. Spatially resolved time-dependent 2D IR signals reveal three regions with different chemical dynamics—the bulk, the interface, and a region between the bulk and interface. This demonstration provides proof-of-concept to use 2D IR microscopy on a wide array of additional chemical systems.

ACKNOWLEDGEMENTS

Graduate school has been quite the journey. There have been highs, lows, and some water bottles full of hexane. Through all the adventures of the past six years, I would not have survived without the incredible support of so many wonderful people.

First, I would like to thank Amber for her support and mentorship. Over my time in graduate school she has been both encouraging and motivating, pushing me to be a better scientist. Thank you for believing in me and helping me to thrive in graduate school.

A special thank you to the past and present members of the Krummel group, for the camaraderie, life lessons, and coffee breaks. Thank you for supporting me through this process, and helping to make this experience enjoyable. I'd especially like to thank Brad for his mentorship, advice, and his uncanny ability to fix the laser with his presence alone. I would also like to take this time to unacknowledged wavenumbers for being a non-intuitive and aggravating unit of measurement.

Thank you to my committee members for your guidance and sound advice throughout this process. Also, thank you to the Department of Chemistry support staff for all their help throughout the years, you have made this process so much easier and less stressful.

Thank you to all of the friends that I have made throughout my six years in Colorado. Your support has kept me sane, and I enjoyed all of the great experiences we have had together throughout these years. I would especially like to thank all of the people who have touched my life through music and theater during my graduate school career. In particular, thank you to Patrice for the beautiful music, wonderful conversations, and helping me stay sane every week. In the words of Albert Einstein, "After a certain high level of technical skill is achieved, science

and art tend to coalesce in esthetics, plasticity, and form. The greatest scientists are always artists as well." So I thank you all for balancing out all this science with beautiful art.

Finally, thank you to my family for all their love and support. My sister, Maura is wonderful and has always been the best "sister friend" I could ever ask for. Thank you for always reminding me that there are more important things than grad school. My parents have always been my best cheerleaders and support system. Thank you for coming to visit me, and the elk, in Colorado every year for my birthday, and for helping me run through the finish line. I hope you all don't mind visiting me in Switzerland next year.

TABLE OF CONTENTS

ABSTRACT ii

ACKNOWLEDGEMENTS iii

LIST OF TABLES ix

LIST OF FIGURES x

Chapter 1 1

Introduction 1

References 8

Chapter 2 17

Materials and Methods 17

2.1 Introduction 17

2.2 Processes and Concepts 17

2.2.1 Introduction to Optical Parametric Chirped Pulse Amplification (OPCPA) 17

2.2.2 Chirped Pulse Amplification (CPA) 18

2.2.3 Optical Parametric Amplification (OPA) 19

2.2.4 Choosing a Nonlinear Crystal 21

2.3 Overview of Experimental Setup 23

2.3.1 Ytterbium Fiber Source 23

2.3.2 Regenerative and Multi-pass Amplifiers 23

2.3.3 OPCPA in Periodically Poled Lithium Niobate (PPLN) 24

2.3.4 CPA of PPLN Stages 25

2.3.5 DFG in Zinc Germanium Phosphide (ZGP) 28

2.3.6 2D IR Spectrometer 30

2.3.7 2D IR Spectroscopy Interfaced with Microfluidics 32

2.3.8 2D IR Microscope 33

2.3.9 Linear IR Absorption Spectroscopy and Microscopy 35

2.4 Sample Preparation 35
2.5 Spectroscopy Methods and Concepts 36
2.5.1 Linear IR Absorption Spectroscopy 36
2.5.2 2D IR Spectroscopy 37
2.5.3 Deciphering a 2D IR Spectrum 38
2.5.4 Measuring Solvent Dynamics with 2D IR Spectroscopy 40
References 43
Chapter 3 46
2D IR Spectroscopy at 100 kHz Utilizing a Mid-IR OPCPA Laser Source 46
3.1 Introduction 46
3.2 Methods 47
3.2.1 Front End and Regenerative and Multi-Pass Amplifier 47
3.2.2 OPCPA 51
3.2.3 PPLN OPCPA Compression 55
3.2.4 ZGP DFG 57
3.2.5 Pulse Shaping and 2D IR measurements 58
3.3 Conclusion 60
3.4 Additional Notes 61
References 62
Chapter 4 68
High Throughput 2DIR Spectroscopy Achieved by Interfacing Microfluidic Technology with a High Repetition Rate 2D IR Spectrometer 68
4.1 Introduction 68
4.2 Results and Discussion 69
4.3 Conclusion 77
4.4 Experimental Methods 78
4.5 Additional Notes 80
References 81

Chapter 5 85
Visualizing Chemical Dynamics in an Ionic Liquid Microdroplet using Ultrafast 2D IR Microscopy 85
5.1 Introduction 85
5.2 Results and Discussion 86
5.3 Conclusion 96
5.4 Additional Notes 97
References 98
Chapter 6 104
Perspective: 2D IR Microscopy: A Path to Spatially Resolved Ultrafast Chemical Dynamics 104
6.1 Introduction 104
6.2 Implementation of 2D IR Microscopy 106
6.3 Moving to Higher Repetition Rates 110
6.4 Extracting Dynamics Information Using High Repetition Rate Sources 113
6.5 Conclusion 114
References 116
Chapter 7 119
Conclusions/Future Work 119
7.1 Conclusions 119
7.2 Future Work 121
Appendix I 123
Alignment Procedures 123
A1.1 Turning on the Laser 123
A1.2 Aligning the PPLN OPCPA Stages 125
A1.3 Aligning the Compression and ZGP DFG 127
A1.4 Aligning the Pump and Probe Beams for the 2D IR Microscope Experiment 128
A1.5 Overlapping the Pump and Probe Beams at the Sample 130
A1.6 Calibration Procedure for the FPAS 133

A1.7 Turning off the Laser 133
A1.8 Alignment of the Regenerative Amplifier 135
A1.9 Alignment of the Multi Pass Amplifier 136
1.10 Abridged Alignment Procedure for the OPCPA and DFG Stages 136
A1.11 Collecting 2D IR of Microfluidics 138
Appendix II 141
MATLAB Programs 141
A2.1 MATLAB Program Used to Plot 2D IR Spectra 141
A2.2 MATLAB Program Used to Extract CLS Data 142
A2.2.1 MATLAB Program Used to Fit Slices Used for CLS 145
A2.2.2 MATLAB Program SubVI for Fitting FTIR 146
A2.2.3 MATLAB Program Fitting Exponential Decay of CLS 150
A2.2.3 MATLAB SubVIs for Fitting Exponential Decay of CLS 151
A2.3 MATLAB Program Used to Plot 2D IR Microscope Image 154
Appendix III 158
Chapter 4 Supplemental Materials 158
References 162
Chapter 5 Supplemental Materials 163
S5.1 Experimental Methods 163
S5.1.1 Sample Preparation 163
S5.2 2D IR Microscopy 164
List of Abbreviations 167

LIST OF TABLES

Table 2.1 Description of Phase for CPA 26

Table 4.1 Anharmonicity Across Device 75

LIST OF FIGURES

Figure 1.1 FTIR Absorption of SCN^- in Different Solvent Environments....2
Figure 1.2 Structures of the RTILs in the Microdroplet Imaged....5
Figure 2.1 Optical Parametric Amplification....19
Figure 2.2 Layout of the Mid-IR OPCPA....22
Figure 2.3 Mid-IR Transmission of PPLN, ZGP, and GaSe....29
Figure 2.4 Layout for the 2D IR Spectrometer....31
Figure 2.5 Layout of the 2D IR Microscope....34
Figure 2.6 Homogenous vs Inhomogenous Conditions....37
Figure 2.7 Deciphering a 2D IR Spectrum....39
Figure 2.8 Illustration of Waiting Time Experimental Data....40
Figure 3.1 Layout of 2D IR Spectrometer....48
Figure 3.2 Regenerative Amplifier Output....50
Figure 3.3 Multi-Pass Amplifier Output....52
Figure 3.4 Third Stage PPLN Output....55
Figure 3.5 Measured FROG of Compressed Third Stage PPLN Output....56
Figure 3.6 Measured ZGP Idler Output....58
Figure 3.7 2D IR Spectra of KOCN in DMF....60
Figure 4.1 2D IR Spectra of KOCN Compared....70
Figure 4.2 Gradient Generation in Microfluidic Device....72
Figure 4.3 2D IR Spectra Collected in a Device....73
Figure 4.4 Dynamics Obtained on Chip....74
Figure 5.1 FTIR Microscopy of RTIL Microdroplet....87
Figure 5.2 2D IR Microscopy Image....89
Figure 5.3 Comparison of the Dynamics in Different Environments in a RTIL Microdroplet....92

Figure 6.1 2D IR Point-Scanning Microscopy 107
Figure 6.2 2D IR Wide-Field Microscopy 108
Figure 6.3 100 kHz, 2D IR Microscope Setup 111
Figure 6.4 Comparison of Yb vs Ti:sapphire Noise 113
Figure 6.5 100 kHz 2D IR Microscopy Image and Extracted Dynamics 114
Figure A1.1 Regenerative Amplifier Setup 134
Figure A1.2 Mapping Area of Pump Probe Overlap in a Microfluidic Device 138
Figure S4.1 The General Layout of the 2D IR Spectrometer 158
Figure S4.2 Characterization of Gradient Generation on Chip 159
Figure S4.3 2D IR Spectra of KOCN in Static Sample For Comparison 160
Figure S4.4 Calculated vs Measured FTIR of KOCN in a Range of Solvent Mixtures 161
Figure S5.1 2D IR Microscope Setup 166

Chapter 1

Introduction

Vibrational infrared (IR) molecular spectroscopy is an umbrella term used to encompass a range of techniques, from the widely used analytical technique, Fourier transform infrared (FTIR) spectroscopy, to the growing field of ultrafast infrared vibrational spectroscopy. IR spectroscopy measures molecular vibrations in condensed phase samples associated with chemical bonds stretching and bending. The molecular vibrations are specific to the groups of atoms within the molecule and sensitive to the solvent environment and the molecular structure. These vibrations are resonant with specific frequencies of mid-infrared (mid-IR) light. IR spectroscopy techniques use mid-infrared (mid-IR) light to irradiate a sample and the resulting absorption pattern is observed. Functional groups each have a characteristic absorption pattern, which give the techniques chemical specificity. The shape, frequency, peak intensity, and bandwidth of the absorption all can be observed and directly report on the molecular composition, structure, solvent environment, and interactions within a sample.

An FTIR spectrometer is a common benchtop analytical instrument that is routinely used in laboratories to characterize molecules. It is used in varying applications from determining the structure and species of organic and biochemical molecules, monitoring reactions, to performing quality control and assurance measurements. For example, FTIR spectroscopy experiments are used to observe the solvent shell surrounding a protein by monitoring changes in the fundamental vibrations of the protein. Pseudo halide anions, such as cyanate (OCN^-), thiocyanate (SCN^-), and selenocyanate ($SeCN^-$) can be used as vibrational tags to investigate the solvent environments of

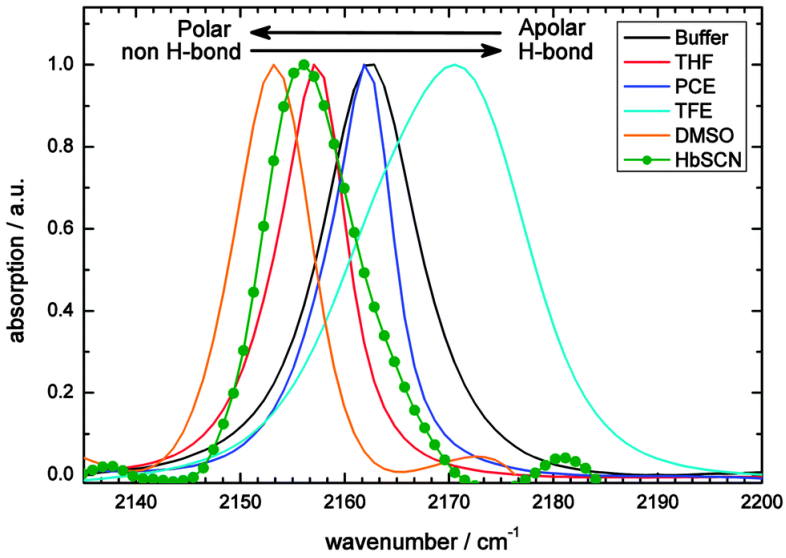

Figure 1.1 FTIR Absorption of SCN^- in Different Solvent Environments

Thiocyanate is used by the Hochstrasser Group to probe a range of solvent environments, and the resulting FTIR are compared.[2]

a protein in solution.[1,2] Specifically, the pseudo halide anion, thiocyanate SCN^-, has been demonstrated as a label for 2D IR spectroscopy of the bovine hemoglobin protein.[2] Pseudo halides absorb in an IR spectral region with limited interference from other functional groups and have a strong absorption in the mid-IR, making the peaks in their absorption spectra easy to decipher. The pseudo halide anions are also useful solvent probes because their vibrational frequencies are very sensitive to the solvent environment. For example, in Figure 1.1, peak shifts and a change in linewidth are observed with an increase in solvent hydrogen bonding. Differences in the structure, hydrogen bonding, and environments of the molecules in the ensemble can contribute to line shape differences in the resultant FTIR spectrum.

In samples where there is a spatial heterogeneity in the chemical composition, the combination of chemical and spatial resolution has made imaging a useful tool.[3] For this purpose FTIR microscopy imaging, adds spatial resolution as an observable and can be used for

exploring a range of applications from biological and biomedical engineering[4–11], to materials[12,13] and nanoscience[14]. However, both FTIR spectroscopy and microscopy experiments lack the time resolution necessary to uniquely determine and quantify dynamics and structural changes that take place within the samples.

In order to measure dynamics, a number of time resolved infrared IR spectroscopy techniques are performed with resolutions ranging from femtoseconds to milliseconds and beyond. Specifically, ultrafast infrared vibrational spectroscopies, such as 2D IR spectroscopy, directly observe molecular vibrations on the timescales that molecular motions occur. The field of 2D IR spectroscopy has developed rapidly over the past 20 years, and technological advances have allowed for a wide range of applications. Studies using 2D IR have investigated protein folding and aggregation[15–18], hydrogen bonding and water dynamics[19,20], transient photochemical dynamics[21,22], and chemical exchange kinetics[23], among others.

The femtosecond to picosecond time resolution of 2D IR spectroscopy expands the number of things measured in the experiment when compared to FTIR spectroscopy, also known as an increase in observables. [24–29] By adding observables, it is possible to observe and time resolve the interactions of molecules with their solvent environments, known as solvent dynamics. It is also possible to observe the time evolution of coupling interactions of functional groups within a molecule making the method sensitive to molecular structure and structural dynamics. Chemical reactions that influence the vibrational properties are also observed with 2D IR spectroscopy, and the rates of these reactions can be extracted in experiments measuring chemical exchange dynamics. As a result, 2D IR spectroscopy measures the structure and dynamics of a sample molecule itself, while also reporting on fluctuations in environment surrounding the molecule.

In order to spatially resolve molecular structure and dynamics of heterogeneous samples, efforts have been made to develop ultrafast 2D IR microscopy. Recently there have been two proof of concept experiments demonstrating the feasibility of ultrafast 2D IR microscopy.[30,31] However, due to long acquisition times associated with these 2D IR microscopy experiments of two to eight hours for a 200 by 200 μm sample window, extensive investigations of chemical dynamics requiring added time points and increased collection time are impractical.

The work completed in this thesis has resulted in more efficient 2D IR imaging, to access the vibrational dynamics information not previously available. Working toward accomplishing this goal, we developed a mid-IR laser source that operates at 100 kHz repetition rate.[32,33] This is a much higher repetition rate source when compared to the one to a few kHz available in commercial, high energy, sources, traditionally used for 2D IR spectroscopy. The source also took advantage of the improved signal-to-noise ratios over traditional sources. Both of these factors allowed us to carry out 2D IR microscopy experiments with much faster acquisition rates. Faster acquisition rates, gave us the ability to spatially resolve the time-dependent 2D IR signals of a heterogeneous system. Specifically, we resolved the dynamics present in a room temperature ionic liquid (RTIL) microdroplet, the chemical structures of which can be seen in Figure 1.2.

Recently, microemulsion and microdroplet technologies have received considerable attention because of their ability to confine a reaction in a very small volume (μL or nL), making previously difficult chemical reactions more favorable.[34–39] Chemical reactions can be accelerated by more than 10^6 times in microdroplets in comparison to bulk reaction conditions.[35] In addition, many researchers have found several important advantages of using RTILs as solvents when compared with organic liquids and have sought to compartmentalize room temperature ionic liquids (RTILs) as designer fluids in droplet microfluidics[40–43]. RTILs are low

melting temperature salts with unique properties such as having a wide electrochemical window, an extremely low vapor pressure, and structural microheterogeneity.[44–46] These properties make RTILs strong candidates for a wide variety of applications from biotechnology[47] to energy technology,[48–50] including as reaction media.[51,52]

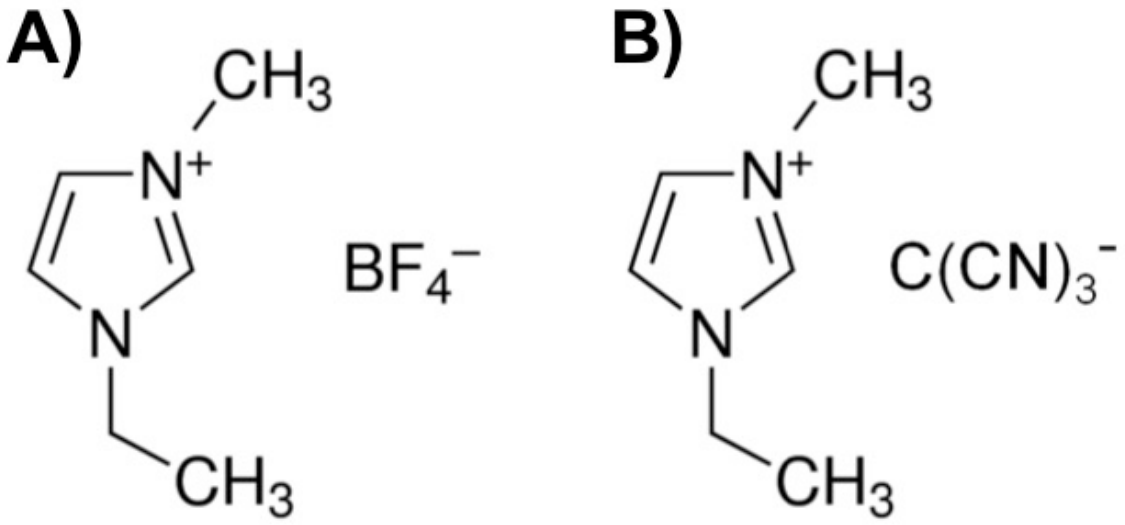

Figure 1.2 Structures of the RTILs in the Microdroplet Imaged

The structures of the room temperature ionic liquids (a) 1-ethyl-3-methylimidazolium tetrafluoroborate ($EmimBF_4$) and (b) 1-ethyl-3-methylimidazolium tricyanomethanide (EmimTCM).

Although RTILs can be tailored to specific purposes due to the ease of interchanging the counter ions involved, this is done in large part using empirical evidence rather than having the ability to predict the behavior of RTILs. Therefore, it is crucial to gain insights into the fundamental aspects of interactions within RTILs including structural dynamics, solute-solvent interactions, and solvation dynamics in order to better understand their behavior. Recently, investigators have turned to nonlinear optical spectroscopy techniques, including 2D IR spectroscopy[53–58], to characterize RTILs at interfaces and measure the dynamics that occur in

bulk RTIL environments. In order to advance the utility of RTILs in microdroplet chemistry, the length scales over which various dynamical behaviors exist are important.[55,59–63]

Although acceleration of reaction rates and many types of previously unknown reactions had been observed in miniaturized microdroplets[34–39], the physical mechanism of the acceleration phenomenon is not yet known. It has been proposed that a different chemical behavior of reactant molecules at the surface of the microdroplet may speed up and favor a reaction. However, the fundamental aspects of structure, ultrafast dynamics, and solvation, which are crucially important determinants in regulating reaction rates in such microdroplets, are entirely unknown.

This thesis details our efforts to develop and build a mid-IR source at high repetition rates for use in spatially resolved ultrafast vibrational dynamics with two-dimensional infrared (2D IR) spectroscopy and microscopy. In Chapter 2, the concepts behind the experimental techniques used in this thesis are described. This includes a description of the nonlinear process involved in the development of the high-repetition rate laser system and a description of 1D and 2D IR spectroscopy. The details and setup of the 100 kHz mid-IR source, 2D IR spectrometer and microscope are also laid out. Appendix I details the many different alignment procedures associated with these techniques. Appendix II includes examples of the MATLAB code used to analyze the data obtained.

Chapter 3 discusses our development and characterization of the 100 kHz, mid-IR OPCPA based laser source. It also demonstrates the first example of 2D IR spectroscopy performed at a100 kHz repetition rate.

Interfacing of 2D IR spectroscopy with IR compatible microfluidic devices comprises the subject of Chapter 4. High-throughput interfacing of 2D IR with microfluidics allows for the

efficient examination of the solvatochromic pseudo-halide anion, cyanate (OCN^-), in co-solvent environments.

Chapter 5 details the use of the high repetition rate source to provide a path to 2D IR microscopy experiments that explore the chemical dynamics within a room temperature ionic liquid microdroplet.

In Chapter 6, a perspective on 2D IR microscopy and the future directions of the field are outlined. This chapter discusses how 2D IR opens up a new avenue for the visualization of structure and dynamics in chemical systems, which is made experimentally feasible using high repetition mid-IR sources.

References

(1) Tucker, M. J.; Kim, Y. S.; Hochstrasser, R. M. 2D IR Photon Echo Study of the Anharmonic Coupling in the OCN Region of Phenyl Cyanate. *Chem. Phys. Lett.* **2009**, *470* (1-3), 80–84.

(2) Wilderen, L. J. G. W. van; Kern-Michler, D.; Müller-Werkmeister, H. M.; Bredenbeck, J. Vibrational Dynamics and Solvatochromism of the Label SCN in Various Solvents and Hemoglobin by Time Dependent IR and 2D-IR Spectroscopy. *Phys. Chem. Chem. Phys.* **2014**, *16* (36), 19643–19653.

(3) Bartick, E. G. Microscopy/Infrared Spectroscopy for Routine Sample Sizes. *Appl. Spectrosc.* **1985**, *39* (5), 885–889.

(4) Nallala, J.; Lloyd, G. R.; Shepherd, N.; Stone, N. High-resolution FTIR Imaging of Colon Tissues for Elucidation of Individual Cellular and Histopathological Features. *Analyst* **2016**, *141* (2), 630–639.

(5) Baker, M. J.; Trevisan, J.; Bassan, P.; Bhargava, R.; Butler, H. J.; Dorling, K. M.; Fielden, P. R.; Fogarty, S. W.; Fullwood, N. J.; Heys, K. A.; et al. Using Fourier Transform IR Spectroscopy to Analyze Biological Materials. *Nat. Protoc.* **2014**, *9* (8), 1771–1791.

(6) Salman, A.; Sebbag, G.; Argov, S.; Mordechai, S.; Sahu, R. K. Early Detection of Colorectal Cancer Relapse by Infrared Spectroscopy in “normal” Anastomosis Tissue. *J. Biomed. Opt.* **2015**, *20* (7), 075007.

(7) Fernandez, D. C.; Bhargava, R.; Hewitt, S. M.; Levin, I. W. Infrared Spectroscopic Imaging for Histopathologic Recognition. *Nat. Biotechnol.* **2005**, *23* (4), 469–474.

(8) Wald, N.; Bordry, N.; Foukas, P. G.; Speiser, D. E.; Goormaghtigh, E. Identification of Melanoma Cells and Lymphocyte Subpopulations in Lymph Node Metastases by FTIR Imaging Histopathology. *Biochim. Biophys. Acta BBA - Mol. Basis Dis.* **2016**, *1862* (2), 202–212.

(9) Großerueschkamp, F.; Kallenbach-Thieltges, A.; Behrens, T.; Brüning, T.; Altmayer, M.; Stamatis, G.; Theegarten, D.; Gerwert, K. Marker-free Automated Histopathological Annotation of Lung Tumour Subtypes by FTIR Imaging. *Analyst* **2015**, *140* (7), 2114–2120.

(10) Lasch, P.; Haensch, W.; Naumann, D.; Diem, M. Imaging of Colorectal Adenocarcinoma Using FT-IR Microspectroscopy and Cluster Analysis. *Biochim. Biophys. Acta BBA - Mol. Basis Dis.* **2004**, *1688* (2), 176–186.

(11) Vrančić, C.; Kröger, N.; Gretz, N.; Neudecker, S.; Pucci, A.; Petrich, W. A Quantitative Look Inside the Body: Minimally Invasive Infrared Analysis in Vivo. *Anal. Chem.* **2014**, *86* (21), 10511–10514.

(12) Bhargava, R.; Wang, S.-Q.; Koenig, J. L. FTIR Microspectroscopy of Polymeric Systems. In *Liquid Chromatography / FTIR Microspectroscopy / Microwave Assisted Synthesis*; Advances in Polymer Science; Springer, Berlin, Heidelberg; pp 137–191.

(13) Bhargava, R.; Wall, B. G.; Koenig, J. L. Comparison of the FT-IR Mapping and Imaging Techniques Applied to Polymeric Systems. *Appl. Spectrosc.* **2000**, *54* (4), 470–479.

(14) Cetiner, S.; Kalaoglu, F.; Karakas, H.; Sarac, A. S. Dielectric, FTIR Spectroscopic and Atomic Force Microscopic Studies on Polypyrrole-poly(acrylonitrile-co-vinyl Acetate) Composites. *Polym. Compos. 32* (4), 546–557.

(15) Jones, K. C.; Peng, C. S.; Tokmakoff, A. Folding of a Heterogeneous B-hairpin Peptide

from Temperature-jump 2D IR Spectroscopy. *Proc. Natl. Acad. Sci.* **2013**, *110* (8), 2828–2833.

(16) Buchanan, L. E.; Dunkelberger, E. B.; Tran, H. Q.; Cheng, P.-N.; Chiu, C.-C.; Cao, P.; Raleigh, D. P.; Pablo, J. J. de; Nowick, J. S.; Zanni, M. T. Mechanism of IAPP Amyloid Fibril Formation Involves an Intermediate with a Transient B-sheet. *Proc. Natl. Acad. Sci.* **2013**, *110* (48), 19285–19290.

(17) Moran, S. D.; Woys, A. M.; Buchanan, L. E.; Bixby, E.; Decatur, S. M.; Zanni, M. T. Two-dimensional IR Spectroscopy and Segmental 13C Labeling Reveals the Domain Structure of Human γD-crystallin Amyloid Fibrils. *Proc. Natl. Acad. Sci. U. S. A.* **2012**, *109* (9), 3329–3334.

(18) Chung, H. S.; Khalil, M.; Smith, A. W.; Ganim, Z.; Tokmakoff, A. Conformational Changes During the Nanosecond-to-millisecond Unfolding of Ubiquitin. *Proc. Natl. Acad. Sci.* **2005**, *102* (3), 612–617.

(19) Fayer, M. D. Water in a Crowd. *Physiology* **2011**, *26* (6), 381–392.

(20) Bakulin, A. A.; Liang, C.; la Cour Jansen, T.; Wiersma, D. A.; Bakker, H. J.; Pshenichnikov, M. S. Hydrophobic Solvation: A 2D IR Spectroscopic Inquest. *Accounts Chem. Res.* **2009**, *42* (9), 1229–1238.

(21) Lynch, M. S.; Slenkamp, K. M.; Khalil, M. Communication: Probing Non-equilibrium Vibrational Relaxation Pathways of Highly Excited C≡N Stretching Modes Following Ultrafast Back-electron Transfer. *J. Chem. Phys.* **2012**, *136* (24), 241101.

(22) Baiz, C. R.; McCanne, R.; Kubarych, K. J. Structurally Selective Geminate Rebinding Dynamics of Solvent-Caged Radicals Studied with Nonequilibrium Infrared Echo Spectroscopy. *J. Am. Chem. Soc.* **2009**, *131* (38), 13590–13591.

(23) Kwak, K.; Zheng, J.; Cang, H.; Fayer, M. D. Ultrafast Two-Dimensional Infrared Vibrational Echo Chemical Exchange Experiments and Theory. *J. Phys. Chem. B* **2006**, *110* (40), 19998–20013.

(24) Hochstrasser, R. M. Two-dimensional Spectroscopy at Infrared and Optical Frequencies. *Proc. Natl. Acad. Sci.* **2007**, *104* (36), 14190–14196.

(25) Zanni, M. T.; Hochstrasser, R. M. Two-dimensional Infrared Spectroscopy: a Promising New Method for the Time Resolution of Structures. *Curr. Opin. Struct. Biol.* **2001**, *11* (5), 516–522.

(26) Woutersen, S.; Hamm, P. Nonlinear Two-dimensional Vibrational Spectroscopy of Peptides. *J. Phys. Condens. Matter* **2002**, *14* (39), R1035.

(27) Fayer, M. D. Dynamics of Liquids, Molecules, and Proteins Measured with Ultrafast 2D IR Vibrational Echo Chemical Exchange Spectroscopy. *Annu. Rev. Phys. Chem.* **2009**, *60* (1), 21–38.

(28) Hamm, P.; Zanni, M. *Concepts and Methods of 2D Infrared Spectroscopy*; Cambridge University Press, 2011.

(29) Headley, J. V.; McMartin, D. W. A Review of the Occurrence and Fate of Naphthenic Acids in Aquatic Environments. *J. Environ. Sci. Heal. Part* **2004**, *39* (8), 1989–2010.

(30) Baiz, C. R.; Schach, D.; Tokmakoff, A. Ultrafast 2D IR Microscopy. *Opt. Express* **2014**, *22* (15), 18724–18735.

(31) Ostrander, J. S.; Serrano, A. L.; Ghosh, A.; Zanni, M. T. Spatially Resolved Two-Dimensional Infrared Spectroscopy via Wide-Field Microscopy. *ACS Photonics* **2016**, *3* (7), 1315–1323.

(32) Luther, B. M.; Tracy, K. M.; Gerrity, M.; Brown, S.; Krummel, A. T. 2D IR

Spectroscopy at 100 kHz Utilizing a Mid-IR OPCPA Laser Source. *Opt. Express* **2016**, *24* (4), 4117–4127.

(33) Tracy, K. M.; Barich, M. V.; Carver, C. L.; Luther, B. M.; Krummel, A. T. High-Throughput Two-Dimensional Infrared (2D IR) Spectroscopy Achieved by Interfacing Microfluidic Technology with a High Repetition Rate 2D IR Spectrometer. *J. Phys. Chem. Lett.* **2016**, *7* (23), 4865–4870.

(34) Bain Ryan M.; Sathyamoorthi Shyam; Zare Richard N. "On-Droplet" Chemistry: The Cycloaddition of Diethyl Azodicarboxylate and Quadricyclane. *Angew. Chem. Int. Ed.* **2017**, *56* (47), 15083–15087.

(35) Lee, J. K.; Banerjee, S.; Nam, H. G.; Zare, R. N. Acceleration of Reaction in Charged Microdroplets. *Q. Rev. Biophys.* **2015**, *48* (4), 437–444.

(36) Li Yafeng; Yan Xin; Cooks R. Graham. The Role of the Interface in Thin Film and Droplet Accelerated Reactions Studied by Competitive Substituent Effects. *Angew. Chem. Int. Ed.* **2016**, *55* (10), 3433–3437.

(37) Yan Xin; Cheng Heyong; Zare Richard N. Two-Phase Reactions in Microdroplets Without the Use of Phase-Transfer Catalysts. *Angew. Chem. Int. Ed.* **2017**, *56* (13), 3562–3565.

(38) Nam, I.; Lee, J. K.; Nam, H. G.; Zare, R. N. Abiotic Production of Sugar Phosphates and Uridine Ribonucleoside in Aqueous Microdroplets. *Proc. Natl. Acad. Sci.* **2017**, *114* (47), 12396–12400.

(39) Fallah-Araghi, A.; Meguellati, K.; Baret, J.-C.; Harrak, A. E.; Mangeat, T.; Karplus, M.; Ladame, S.; Marques, C. M.; Griffiths, A. D. Enhanced Chemical Synthesis at Soft Interfaces: A Universal Reaction-Adsorption Mechanism in Microcompartments. *Phys.*

Rev. Lett. **2014**, *112* (2), 028301.

(40) Barikbin, Z.; Rahman, M. T.; Parthiban, P.; Rane, A. S.; Jain, V.; Duraiswamy, S.; Lee, S. H. S.; Khan, S. A. Ionic Liquid-based Compound Droplet Microfluidics for "on-drop" Separations and Sensing. *Lab. Chip* **2010**, *10* (18), 2458–2463.

(41) Lazarus, L. L.; Riche, C. T.; Marin, B. C.; Gupta, M.; Malmstadt, N.; Brutchey, R. L. Two-Phase Microfluidic Droplet Flows of Ionic Liquids for the Synthesis of Gold and Silver Nanoparticles. *ACS Appl. Mater. Interfaces* **2012**, *4* (6), 3077–3083.

(42) Lazarus, L. L.; Yang, A. S.-J.; Chu, S.; Brutchey, R. L.; Malmstadt, N. Flow-focused Synthesis of Monodisperse Gold Nanoparticles Using Ionic Liquids on a Microfluidic Platform. *Lab. Chip* **2010**, *10* (24), 3377–3379.

(43) Malankowska, M.; Martins, C. F.; Rho, H. S.; Neves, L. A.; Tiggelaar, R. M.; Crespo, J. G.; Pina, M. P.; Mallada, R.; Gardeniers, H.; Coelhoso, I. M. Microfluidic Devices as Gas – Ionic Liquid Membrane Contactors for CO2 Removal from Anaesthesia Gases. *J. Membr. Sci.* **2018**, *545*, 107–115.

(44) Canongia Lopes, J. N. A.; Pádua, A. A. H. Nanostructural Organization in Ionic Liquids. *J. Phys. Chem. B* **2006**, *110* (7), 3330–3335.

(45) Samanta, A. Dynamic Stokes Shift and Excitation Wavelength Dependent Fluorescence of Dipolar Molecules in Room Temperature Ionic Liquids. *J. Phys. Chem. B* **2006**, *110* (28), 13704–13716.

(46) Jr, E. W. C.; Margulis, C. J.; Maroncelli, M.; Wishart, J. F. Ionic Liquids: Structure and Photochemical Reactions. *Annu. Rev. Phys. Chem.* **2011**, *62* (1), 85–105.

(47) Egorova, K. S.; Gordeev, E. G.; Ananikov, V. P. Biological Activity of Ionic Liquids and Their Application in Pharmaceutics and Medicine. *Chem. Rev.* **2017**, *117* (10), 7132–

7189.

(48) Tadesse, H.; Luque, R. Advances on Biomass Pretreatment Using Ionic Liquids: An Overview. *Energy Environ. Sci.* **2011**, *4* (10), 3913–3929.

(49) Watanabe, M.; Thomas, M. L.; Zhang, S.; Ueno, K.; Yasuda, T.; Dokko, K. Application of Ionic Liquids to Energy Storage and Conversion Materials and Devices. *Chem. Rev.* **2017**, *117* (10), 7190–7239.

(50) Lin, R.; Taberna, P.-L.; Fantini, S.; Presser, V.; Pérez, C. R.; Malbosc, F.; Rupesinghe, N. L.; Teo, K. B. K.; Gogotsi, Y.; Simon, P. Capacitive Energy Storage from −50 to 100 °C Using an Ionic Liquid Electrolyte. *J. Phys. Chem. Lett.* **2011**, *2* (19), 2396–2401.

(51) Plechkova, N. V.; Seddon, K. R. Applications of Ionic Liquids in the Chemical Industry. *Chem. Soc. Rev.* **2007**, *37* (1), 123–150.

(52) Smiglak, M.; Metlen, A.; Rogers, R. D. The Second Evolution of Ionic Liquids: From Solvents and Separations to Advanced Materials—Energetic Examples from the Ionic Liquid Cookbook. *Accounts Chem. Res.* **2007**, *40* (11), 1182–1192.

(53) Tamimi, A.; Fayer, M. D. Ionic Liquid Dynamics Measured with 2D IR and IR Pump–Probe Experiments on a Linear Anion and the Influence of Potassium Cations. *J. Phys. Chem. B* **2016**, *120* (26), 5842–5854.

(54) Tamimi, A.; Bailey, H. E.; Fayer, M. D. Alkyl Chain Length Dependence of the Dynamics and Structure in the Ionic Regions of Room-Temperature Ionic Liquids. *J. Phys. Chem. B* **2016**, *120* (30), 7488–7501.

(55) Shin, J. Y.; Yamada, S. A.; Fayer, M. D. Dynamics of a Room Temperature Ionic Liquid in Supported Ionic Liquid Membranes Vs the Bulk Liquid: 2D IR and Polarized IR Pump–Probe Experiments. *J. Am. Chem. Soc.* **2017**, *139* (1), 311–323.

(56) Ren, Z.; Brinzer, T.; Dutta, S.; Garrett-Roe, S. Thiocyanate as a Local Probe of Ultrafast Structure and Dynamics in Imidazolium-Based Ionic Liquids: Water-Induced Heterogeneity and Cation-Induced Ion Pairing. *J. Phys. Chem. B* **2015**, *119* (13), 4699–4712.

(57) Dutta, S.; Ren, Z.; Brinzer, T.; Garrett-Roe, S. Two-dimensional Ultrafast Vibrational Spectroscopy of Azides in Ionic Liquids Reveals Solute-specific Solvation. *Phys. Chem. Chem. Phys.* **2015**, *17* (40), 26575–26579.

(58) Ren, Z.; Ivanova, A. S.; Couchot-Vore, D.; Garrett-Roe, S. Ultrafast Structure and Dynamics in Ionic Liquids: 2D-IR Spectroscopy Probes the Molecular Origin of Viscosity. *J. Phys. Chem. Lett.* **2014**, *5* (9), 1541–1546.

(59) K. Kashyap, H.; J. Hettige, J.; R. Annapureddy, H. V.; J. Margulis, C. SAXS Anti-peaks Reveal the Length-scales of Dual Positive–negative and Polar–apolar Ordering in Room-temperature Ionic Liquids. *Chem. Commun.* **2012**, *48* (42), 5103–5105.

(60) Amith, W. D.; Hettige, J. J.; Castner, E. W.; Margulis, C. J. Structures of Ionic Liquids Having Both Anionic and Cationic Octyl Tails: Lamellar Vacuum Interface Vs Sponge-Like Bulk Order. *J. Phys. Chem. Lett.* **2016**, *7* (19), 3785–3790.

(61) Paredes, X.; Fernández, J.; Pádua, A. A. H.; Malfreyt, P.; Malberg, F.; Kirchner, B.; Pensado, A. S. Using Molecular Simulation to Understand the Structure of [C2C1im]+–Alkylsulfate Ionic Liquids: Bulk and Liquid–Vapor Interfaces. *J. Phys. Chem. B* **2012**, *116* (48), 14159–14170.

(62) Anaredy, R. S.; Shaw, S. K. Long-Range Ordering of Ionic Liquid Fluid Films. *Langmuir* **2016**, *32* (20), 5147–5154.

(63) Jurado, L. A.; Kim, H.; Arcifa, A.; Rossi, A.; Leal, C.; Spencer, N. D.; Espinosa-Marzal,

R. M. Irreversible Structural Change of a Dry Ionic Liquid Under Nanoconfinement. *Phys. Chem. Chem. Phys.* **2015**, *17* (20), 13613–13624.

Chapter 2

Materials and Methods

2.1 Introduction

The goal of the work reported here was to develop a laser system operating at 100 kHz repetition rates. In order to perform 2D IR experiments with system it must produce short pulses in the mid-IR on the 200 fs length scale and an output of μJ level pulse energies. These are the requirements necessary to perform 2D IR experiments on the time scales of interest. In this chapter, I first discuss the processes and concepts behind the experimental techniques used in this thesis. I then discuss the experimental design of the various components of the source and the experimental methods of the spectroscopy performed.

2.2 Processes and Concepts

2.2.1 Introduction to Optical Parametric Chirped Pulse Amplification (OPCPA)

Optical parametric chirped pulse amplification (OPCPA) is the nonlinear process that combines chirped pulse amplification (CPA) with optical parametric amplification (OPA).[1–6] In this process, two electric fields, the pump and seed, are overlapped in a nonlinear crystal, and energy is allowed to transfer between the two fields, thus generating a third field in the process, the idler. The energy transfer causes an amplification of the intensity of the seed, while depleting the intensity of the pump. The generated idler has a frequency dictated by difference frequency generation (DFG), where the idler frequency is the difference between the pump and seed frequencies. The optical parametric amplification (OPA) portion is combined with the CPA technique to utilize the relatively low thermal load in the gain material associated with OPA

processes, which allows the system to be operated at high repetition rates and high average powers in systems without exceeding the damage threshold of the nonlinear crystals.[1] In the next two sections, the process of CPA and OPA will be described in detail.

2.2.2 Chirped Pulse Amplification (CPA)

Chirped Pulse Amplification (CPA) is a method used to avoid damaging levels of pulse intensity in the light amplification process while maintaining high amplification efficiency.[7] CPA is accomplished by adding a temporal phase to the pulse before it is passed through the amplification medium. The temporal phase shift increases the length of the pulse and decreases the pulse intensity. Temporal phase, ϕ(t), contains frequency information as a function of time and can be written as a Taylor series expansion,

$$\phi(t) = \phi_0 + \phi_1' \frac{t}{1!} + \phi_2'' \frac{t^2}{2!} + \cdots \qquad (2.1)$$

The second order phase term, ϕ_2'', referred to as Group Delay Dispersion (GDD) creates a ramp of frequency as a function of time. Pulses with increasing frequency versus time are said to be "positively chirped" and pulses with decreasing frequency versus time are said to be "negatively chirped". In the case of positively chirped pulses, the red colors propagate through space before the blue colors.

Changing the phase terms will change the length of the pulse in time. The shortest pulse occurs when phase is a constant, or there are no higher order terms in the phase. Pulses with constant phase are referred to as transform limited. Stretching a pulse by adding chirp will both increase the length of the pulse in time and decrease the pulse intensity. CPA utilizes the decrease in pulse intensity to reduce the peak power of the pulse to avoid damaging the nonlinear crystal during amplification. After amplification, the pulse must be recompressed by countering

the phase terms added to the pulse with phase terms of the opposite sign. Using this method, a pulse will be generated that is the same length in time as the initial seed pulse but will have a much larger intensity.

2.2.3 Optical Parametric Amplification (OPA)

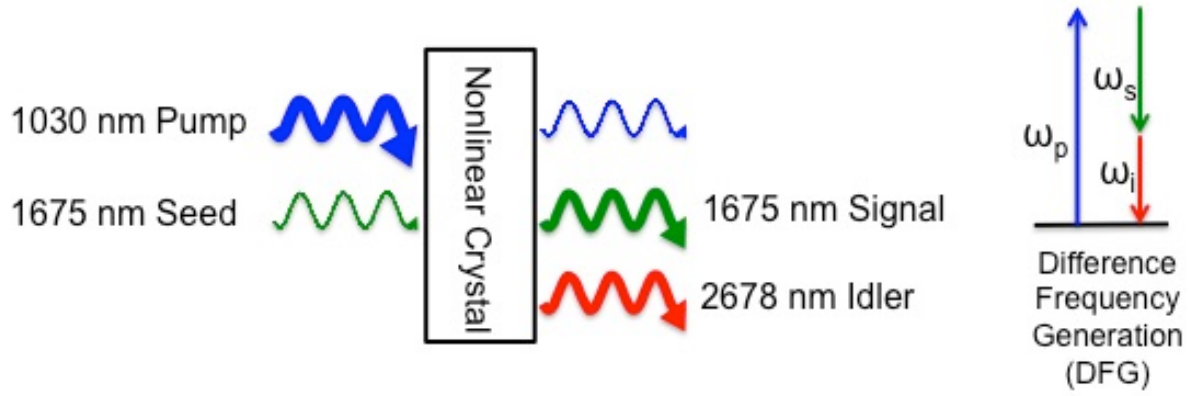

Figure 2.1 Optical Parametric Amplification

A block diagram describing general process of optical parametric generation. The difference frequency process, where the frequency of the idler is the difference between the pump and seed frequencies, $\omega_i = \omega_p - \omega_s$.

Optical parametric amplification (OPA) is a second order, nonlinear process involving the mixing of two electric fields to generate a third electric field, see Figure 2.1.[8,9] In an OPA, there are two incoming electric fields. The first field is referred to as the pump field, which has a high intensity relative to the second incoming field. The second field is referred to as the seed or signal field and is the field that is amplified in the nonlinear process. The pump and seed fields are overlapped in a nonlinear crystal. The transfer of energy between the two fields is only allowed when the two electric fields are phase matched, generating an amplification of the intensity of the seed and a new idler field. Depending on the phase matching conditions, different types of nonlinear processes may occur. The primary OPA process used in this system

is DFG, where the idler frequency is the difference between the pump and signal frequencies, see Figure 2.1.

The phase matching conditions that are utilized in the OPA dictate which type of nonlinear process occurs.[8,9] The goal of phase matching is to keep the nonlinear polarization generated by the pump and signal field in phase with the generated field of the idler. If the polarization is out of phase with the generated field, they will destructively interfere with each other and no light will be emitted at the idler frequency. In order to emit at the new idler frequency, the phase matching condition for the DFG of the three fields must be met. The phase matching condition dictates that the wave vector of the pump, k_p, minus the wave vectors of the signal, k_s, and idler, k_i, must be zero.

$$\Delta k = k_p - k_s - k_i = 0 \qquad (2.2)$$

Achieving the phase matching condition, $\Delta k = 0$, depends on various factors. The wave vectors are a function of the index of refraction and the wavelength. In cases where the dispersion in the material and the index of refraction are not the same for all the wavelengths of light, the $\Delta k = 0$ phase matching condition will not be met. However, when light propagates through some nonlinear crystals; the refractive index of the light depends on the direction it travels through the crystal, this is called birefringence. The birefringence of a crystal can be used to alleviate the problem of mismatched index of refraction. By sending the seed and the pump fields into the crystal in different acceptance angles it is possible to change the refractive index for each field, and use the orientation of the beams to minimize Δk. The type of phase matching that is occurring in the system depends on the orientation of these beams with respect to the crystal.

2.2.4 Choosing a Nonlinear Crystal

There are a number of different properties of the nonlinear crystal material that can affect the amplification efficiencies of an OPA. At a minimum, the crystal material must have a high level of transparency at all the wavelengths involved in the OPA. Other properties that will affect the types of phase matching used in the OPA are birefringence, chromatic dispersion, and the acceptance angle of the crystal for phase matching. Ideally, the magnitude of the effective nonlinear coefficient must be as large as possible in order to maximize gain and depends on the type of phase matching chosen. It is possible to model the behavior of a pulse within a nonlinear crystal and numerically simulate its evolution. This allows the parameters such as pulse length, pulse energy, beam size, and crystal length to be optimized for maximum amplification.[4]

Other factors need to be accounted for when designing an OPA stage. For example, crystal length is very important. If the chosen length for the crystal is too long, back conversion can take place, where the energy in the signal field will convert back to the pump field. It is also possible for background noise to be amplified leading to a lower level of amplification than desired. If the different frequencies of light travel at different velocities through the crystal as a result of having different group velocities, their temporal overlap can also be lost over the length of the crystal, a problem referred to as temporal walk off. To alleviate all of these issues, crystal lengths are kept as short as possible, while still allowing for adequate amplification.[4]

Maintaining the bandwidth of the pulses in these nonlinear processes is also a concern that needs to be accounted for in the design. If the center frequencies of a pulse are amplified more than the outer frequencies, also known as gain narrowing, the frequencies present in the pulse are effectively limited. Utilizing a long pump pulse and a short signal pulse in the crystal can reduce this problem. Gain bandwidth is another problem and is a function of the properties

of the chosen crystal. In some crystals, bandwidths that are able to generate gain in a pulse are small, therefore choosing a crystal with a large gain bandwidth is important. Minimizing crystal length will minimize this effect by limiting the phase velocity mismatch between the different wavelengths. When designing an OPA stage it is important that a nonlinear crystal be chosen where the strength of the nonlinear interactions is high so the nonlinear process occurs efficiently. This is typically chosen by utilizing crystals with high effective nonlinear coefficient, d_{eff}. The crystal also needs to be pumped at as high an intensity as is safe so that the crystal length can be minimized and the bandwidth will be maximized.

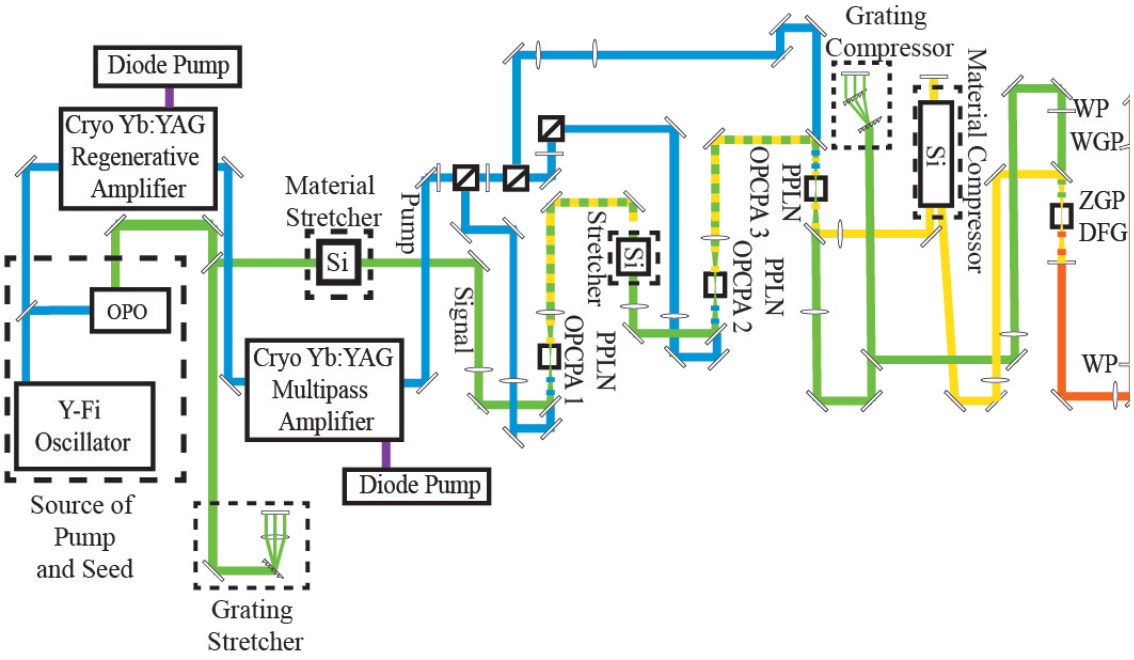

Figure 2.2 Layout of the Mid-IR OPCPA

The Y-Fi oscillator output seeds the regenerative amplifier generating the pump of the OPCPA stages. The rest of the oscillator output pumps a MgO:PPLN OPO, the output of which is stretched and seeds the three stages of MgO:PPLN. The resulting amplified signal and idler are compressed and used as the pump and signal beams in a ZGP DFG stage generating a 4.65 μm idler.[6]

2.3 Overview of Experimental Setup

The general layout of the high repetition rate system and 2D IR spectroscopy experiment can be seen in Figure 2.2 and is discussed in more detail in Chapter 3.[6] In this section, the components in the optical setup will be briefly discussed. Descriptions of the alignment procedures can be found in Appendix I.

2.3.1 Ytterbium Fiber Source

The common source of light for the entire system is an All Normal Dispersion (ANDi) Ytterbium-Fiber mode-locked oscillator (KM Labs, Y-Fi). The single source generates both the seed and pump for the OPCPA stages. The 63 MHz pulse train from the Y-Fi is divided down to 100 kHz and sent to a digital delay generator (Stanford Research Systems, DG645), thus forming the basis for all the timing in the system. The Y-Fi output generates chirped pulses centered at 1040 nm with a 20 nm FWHM at 8 nJ per pulse. The majority of the Y-Fi output is compressed and used to seed a MgO:PPLN based optical parametric oscillator (OPO) generating 170 fs pulses with ~200 pJ of energy per pulse centered at 1.68 μm.

2.3.2 Regenerative and Multi-pass Amplifiers

The remaining output of the Y-Fi is used to seed the cryogenically cooled Yb:YAG based regenerative amplifier generating the pump for the OPCPA. Yb:YAG crystals were chosen as the amplification medium, as opposed to Ti:sapphire amplifiers, which are the standard, in commercially available sources used in 2D IR. Ti:sapphire systems do not allow for the increased amplification or thermal performance needed to go to higher repetition rates. In the

regenerative amplifier, Yb:YAG is pumped with a 940 nm continuous wave diode laser. The 1030 nm pulses seeding the regenerative amplifier have picosecond pulse length due to the chirp on the Y-Fi output. However, this chirp becomes negligible due to the narrow emission line width and gain narrowing that occurs in the amplification process. The resulting amplified pulses are bandwidth limited to ~9 ps with sub-nm bandwidth. High repetition rate Pockels cells are used to remove post-pulses following the regenerative amplifier. Pulse energies up to 87 μJ (8.7 W) were obtained. In the multi pass amplifier, a cryogenically cooled, two pass, Yb:YAG power amplifier is used to amplify the regenerative amplifier output. Energies of 695 μJ (69.5 W) were obtained. The multi pass output is used as the pump beam for the OPCPA stages.

2.3.3 OPCPA in Periodically Poled Lithium Niobate (PPLN)

There are three stages of OPCPA amplification using MgO:PPLN crystals. In these stages, the 1.68 μm output from the OPO is used as the seed and is stretched and amplified. The 1.03 μm output of the multi pass amplifier is used as the pump for these stages. The pump and seed pulses are overlapped in space and time in three stages of PPLN crystals. PPLN crystals utilize quasi phase matching techniques. The nonlinear crystal used in quasi phase matching is spatially modulated, poled, so that the sign of the polarization is switched at specific intervals over the distance of the crystal. This poling allows for correction to some phase mismatch that occurs over the length of a crystal. The regions where back conversion would occur are corrected in a poled crystal so more gain is achieved. This raises the effective nonlinear coefficient of the crystal by using the largest susceptibility, which occurs when the three fields are aligned. Bandwidth is maintained in the three PPLN stages by using short, 3 mm long crystals.

In the first PPLN stage, the 1.2 ps chirped 1675 nm seed light is overlapped with the 9 ps 1030 nm pump pulse. This overlap allows an even gain across the different wavelengths of the seed pulse so gain narrowing is minimized. The seed pulse is stretched before the second PPLN stage from 1.2 ps to 4.6 ps to more closely match the 9 ps pump pulse duration. Better temporal overlap between the pump and signal pulse allows more efficient extraction from the pump. Following the third PPLN stage, the resulting idler is compressed in a material silicon compressor[18] resulting in ~235 fs FWHM pulses centered at 2.68 μm with 17.5 μJ of energy per pulse. The signal pulses are compressed in a transmission grating compressor resulting in a 210 fs pulse length for the 36 μJ pulse.

2.3.4 CPA of PPLN Stages

The compression of the 1.68 μm light in the OPCPA stages is more complicated than in typical CPA. In CPA alone, the pulse would be stretched with a grating stretcher and recompressed after amplification with a grating compressor. The phase in the grating stretcher will be equal and opposite to the phase in the grating compressor, canceling all three orders of phase. However, in this system not only must the 1.68 μm light be compressed, but the 2.68 μm idler must also be compressed. This creates an interesting problem for the third order dispersion (TOD) of the generated 2.68 μm pulses due to the fact that the phases of the signal (φ_s), idler (φ_i), and pump (φ_p), must follow,

$$\phi_i = \phi_p - \phi_s \qquad (2.3)$$

In the case of the PPLN stages, the pump is transform limited, thus, the phase of the pump is a constant. Therefore, the idler phase and signal phase will have opposite signs. The idler is generated with the opposite chirp than the signal chirp causing an inversion about the frequency

axis. This results in the group velocity dispersion (GVD) and fourth order dispersion (FOD) negating while the TOD remains the same. Table 2.1A outlines the sign of the second through fourth order phase added to a 1.68 μm pulse when it is sent through a stretcher, compressor, or positively and negatively dispersive materials. The effects of stretching the initial 1.68 μm pulse, on the phase of the 2.68 μm pulse must to be taken into account and can be seen in Table 2.1B. Finally, the sign of the second through fourth order phase of the 2.68 μm pulse can be seen in Table 2.1C. A solution for effectively compressing the idler in this system can be found by stretching the 1.68 μm pulse with a grating stretcher (Table 2.1A), which will generate negative GVD, TOD, and FOD for the generated 2.68 μm light (Table 2.1B). Subsequently, this pulse can be compressed in a material compressor (Table 2.1C). The ratio of GVD to TOD for the 1.68 μm beam was adjusted by adding material to the 1.68 μm stretcher, which increased GVD while reducing TOD.

The compressed idler is measured using frequency resolved optical gating (FROG) to determine the pulses length in time.[19] In the FROG measurement, the beam is split with each half traveling through separate path lengths and recombined on a doubling crystal so the spectrum of light can be measured as a function of time as the one of the two pulses is stepped through the other in time. From the measured FROG spectrum of the doubled light as a function of time, it is possible to extract temporal intensity as a function of time. The FROG measurement of the compressed idler is described in detail in Chapter 3 and can be seen in Figure 3.5. The measurement shows that idler 2.68 μm pulses were compressed to a FWHM of 235 fs and the signal 1.68 μm pulses were compressed to a FWHM of 210 fs. It is the length of these two compressed pulses, which dictate the length of the mid-IR pulses produced from the system.

Table 2.1 Description of Phase for CPA

Describes the signs of the phase added to the (A) 1.68 μm light stretch and (B) the resulting phase for the 2.68 μm idler generated from (A). (C) Describes the signs of the phase added to the 2.68 μm light.

A)

Generated 2.68 μm	GVD	TOD	FOD
Stretcher	-	-	-
Material (+)	-	+	-
Compressor	+	+	+
Material (-)	+	+	+

B)

At 1.68 μm	GVD	TOD	FOD
Stretcher	+	-	+
Material (+)	+	+	+
Compressor	-	+	-
Material (-)	-	+	-

C)

At 2.68 μm	GVD	TOD	FOD
Stretcher	+	-	+
Material (+)	+	+	+
Compressor	-	+	-
Material (-)	-	+	-

2.3.5 DFG in Zinc Germanium Phosphide (ZGP)

Zinc Germanium Phosphide (ZGP) was chosen as the nonlinear crystal for the final DFG OPA stage. It was important for the crystal to be transparent from the 1.68 μm pump to the 4.65 μm mid-IR pulses generated. The three crystals that were considered for this stage were ZGP, PPLN, and Gallium Selenide (GaSe). ZGP and GaSe both have high transparency over this range of wavelengths, and both are transparent at much higher wavelengths than the PPLN crystal used for the 3 OPCPA stages, as seen in Figure 2.3.

The behavior of a pulse within the three different nonlinear crystals was calculated using the software Select Non-Linear Optics (SNLO) in order to make a decision of which medium was best suited for the purposes of this OPA. Calculating the temporal walk off between the different pulses as a function of crystal length showed that even at very short crystal lengths, PPLN crystals experience a temporal walk off of the signal pulses with respect to the idler larger than the pulse lengths. The temporal walk off of the idler with respect to the pump pulse was also significant. This means that the pulses would not be overlapped in time after a certain propagation length through the PPLN crystal; therefore PPLN is not a viable option. ZGP and GaSe crystals both had some walk off in the pulses, but they could be minimized by using a 0.5 mm crystal length.

Although GaSe had the largest effective nonlinear coefficient of the three crystals, it was ruled out for a few different reasons. The GaSe crystal was much softer than the other crystals. Therefore, the crystal could not be coated with antireflection coatings so there would be significant losses due to reflections. The damage threshold of the GaSe was also of concern, as the crystal could not be pumped as hard as a ZGP crystal. Both, the lack of antireflection coating and lower pump energies would reduce the potential output.

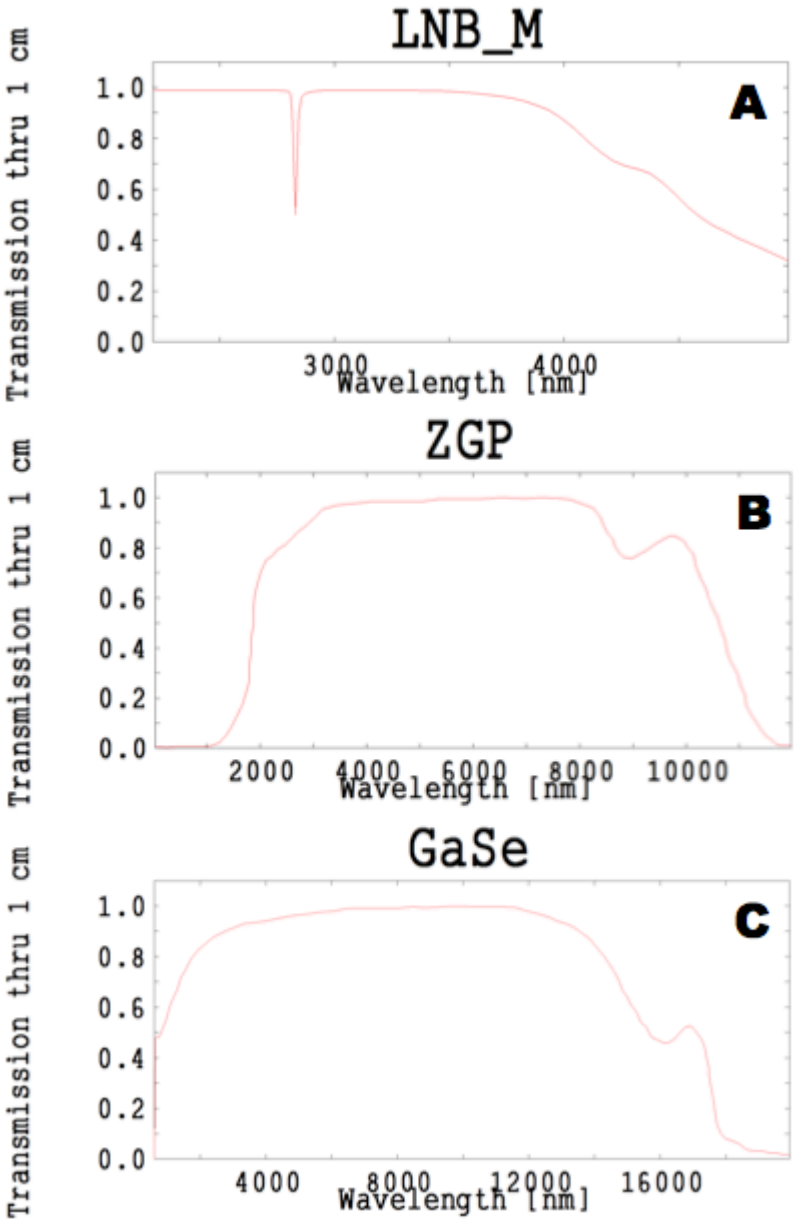

Figure 2.3 Mid-IR Transmission of PPLN, ZGP, and GaSe

Transmission spectrum a) PPLN (periodically poled $LiNbO_3$) and b) ZGP c) GaSe crystals from the SNLO program. It shows that PPLN crystals fall below a usable level of transmission past around 4.5 μm, while the ZGP and GaSe crystals are usable in the range of interest.

Based on the above considerations, a ZGP crystal was chosen for the OPA stage, and calculations were performed using the program SNLO to determine the important attributes of this stage. Type I phase matching is used in this crystal, where the pump and seed pulses are sent into the crystal at perpendicular polarizations and the idler wave is generated at the same polarization as the seed pulse. For these wavelengths the d_{eff} is 45.5 pm/V and the acceptance angle for phase matching 74.1° with the signal and idler along the extraordinary axis of the crystal and the pump along the ordinary axis. The compressed beams are recombined in 0.5 mm path length ZGP OPA generating 3 μJ of a 4.65 μm mid-IR idler output at 220 fs pulse lengths.

2.3.6 2D IR Spectrometer

The layout for the 2D IR spectrometer can be seen in Figure 2.4. The 2D IR spectrometer splits the mid-IR output into two lines utilizing a variable wavelength half-waveplate and wire-grid polarizer. One line is sent to a 100 kHz, mid-IR pulse shaper (PhaseTech Spectroscopy) to generate the pump pulse pair at 100 kHz with variable delay. In the pulse shaper, the pump pulse is dispersed in frequency space onto a germanium acousto-optic modulator (AOM) which is in the fourier plane of a 4f Martinez stretcher. A waveform is then generated in an arbitrary waveform generator (AWG), and sent to the AOM where it is converted to an acoustic wave using a piezoelectric transducer. Modulations in the amplitude and phase of the waveform allow the generation of pump pulse pairs at 100 kHz with variable delay and phase.[20–22] It is also possible to use the pulse shaper to vary the relative phase of the two pump pulses in the sequence used to collect 2D IR, in a procedure called phase cycling.[23] In the experiments described in this thesis, both two frame phase cycling (0,0) (0,π) and four frame phase cycling (0,0), (0, π), (π, π), and (π,0) schemes are used. Using the pulse shaper, the time separation between the pump

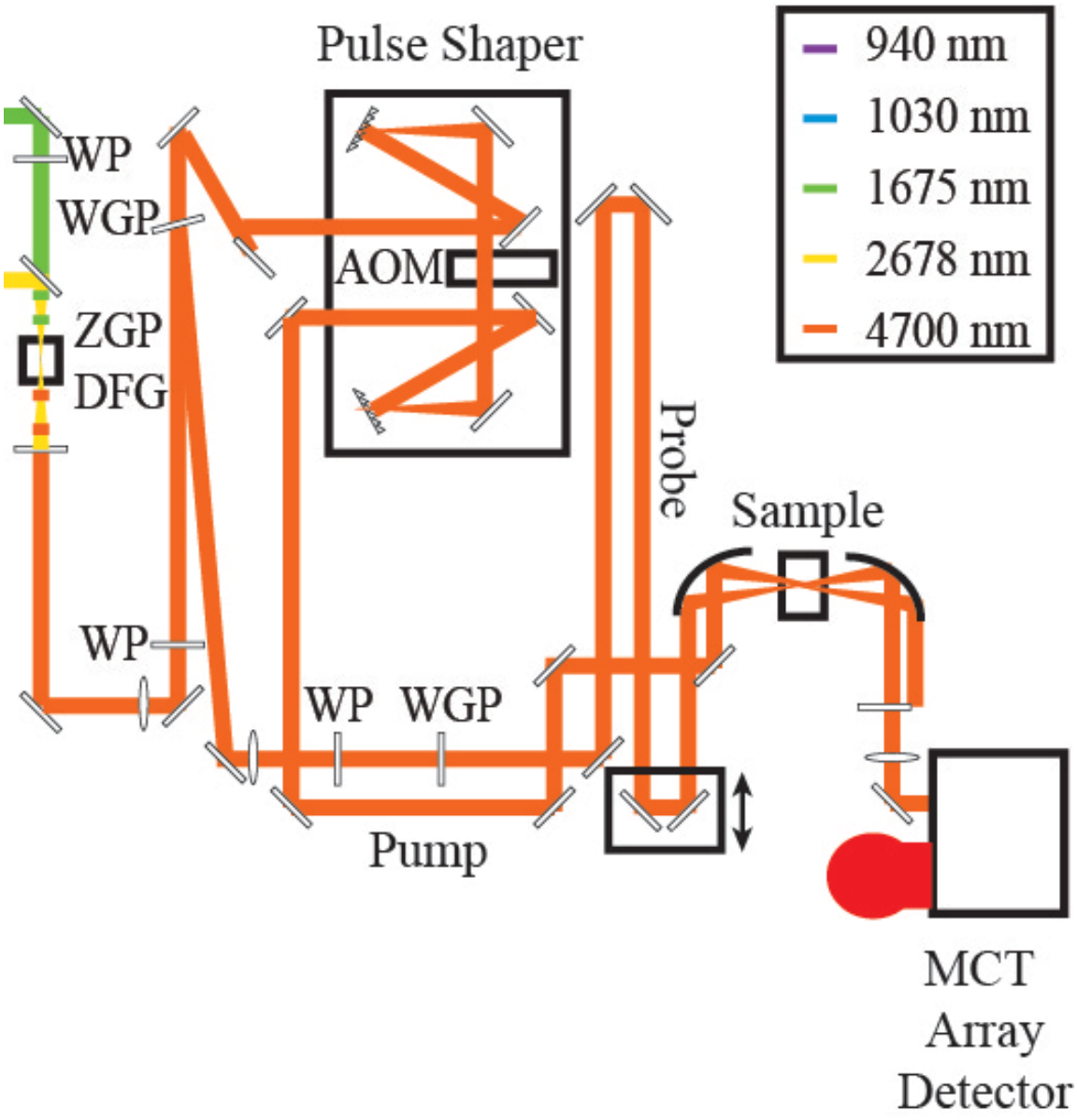

Figure 2.4 Layout for the 2D IR Spectrometer

The ZGP idler is split using a combination of a waveplate (WP) and wire grid polarizer (WGP). One line is sent to a pulse shaper to generate the pump pulse pair. The second line used as the probe line in a 2D IR spectrometer. The pump and probe pulses are focused using a parabolyic mirror onto the sample where they are overlapped in space. The pump pulse is then blocked and the probe and signal beams are detected on a MCT array detector.

pulses can be altered every shot, in a process called rotating frame[23], to further reduce the acquisition time by undersampling.[23]

The second line is sent through a second waveplate and polarizer giving polarization control and is used as the probe pulse, seen in Figure 2.4. The pump and probe pulses are focused onto a CaF_2 sample cell using a four inch focal length, 90° off axis parabola and the probe beam is sent to a 100 kHz, 1x64 element, gated mercury cadmium telluride (MCT) mid-IR spectrometer (Infrared Systems Development, FPAS). With the 100 kHz pulse shaping and MCT array detector, it is possible to collect each laser shot and generate 2D IR spectra on the millisecond timescale. With this set up we were the first group to ever successfully collect a 2D IR spectrum at 100 kHz.[6]

2.3.7 2D IR Spectroscopy Interfaced with Microfluidics

IR compatible, thin chip microfluidic devices were developed and fabricated by Dr. Michael Barich for use in measuring mixed solvent environments.[24] For the purposes of the studies in Chapter 4, the devices were fabricated using a standard photolithography technique in polydimethyl siloxane (PDMS, Sylgard 184, Dow Corning). The IR compatible microfluidic chips were comprised of four components: a support layer, microchannel layer, adhesion layer, and calcium fluoride backbone. To create the complete microfluidic device, all four components were individually prepared and then assembled by sealing the PDMS via the air plasma method.[24] In order to easily interface the microfluidic device with the 2D IR spectrometer using the same sample holder used for the traditional bulk samples, a custom acrylic case was used to encase each chip. Two syringe pumps (NE-500 Programmable OEM) were used to pump fluid in

10 mL syringes into the microfluidic devices. Typical flow rates used were 6.0 μL/min for both streams entering the device.

Interfacing the microfluidic devices with the 2D IR spectrometer was accomplished by 3D mapping both pump and probe scatter off the channel edges, the method is described in more detail in Appendix 1.11. The X and Z location of the scatter position at the channel walls for both edges of the channel were recorded, where the X direction is perpendicular to the direction of the beam propagation, the Y direction is vertical coming out of the table, and the Z direction is the direction of the beam propagation. This allowed the relative beam paths to be plotted and fitting each edge location to a line allowed the intersection of the beams to be calculated in 2D space with respect to the microfluidic channel. A 3-axis translational stage was used to sample locations in a slice across the channel.

2.3.8 2D IR Microscope

As seen in Figure 2.5 in the 2D IR microscope layout, the pump and probe pulses are split and separately sent to a mid-IR, high-speed pulse shaper to generate the pump pulse pair and sent through a delay path for the probe line. These two lines are recombined using a polarizer that transmits the pump pulses and reflects the probe pulse to create a collinear geometry. In collinear geometry the pump pulses are one polarization and the probe and signal are rotated by 90 degrees, so the spectra are collected in what is referred to as the cross polarization (XXYY) geometry.[23] The three pulses are focused into the sample by a Ge/Si Achromatic lens and then re-collimated using a Si lens. The signal and probe pulses are isolated from the pump pulses utilizing two wire grid polarizers and sent to a 100 kHz, 1x64 element, gated mercury cadmium telluride (MCT) mid-IR spectrometer (Infrared Systems Development,

FPAS). To collect an image, the sample was moved and steps were taken in the x and y direction using a nanopositioner and two micropositioners. The sample was scanned in the x-direction and then a step was taken in the y-direction and the x-direction scan was repeated; thus producing an acquisition rate of 1984 individual spectra per minute. More details are provided in Chapter 5.

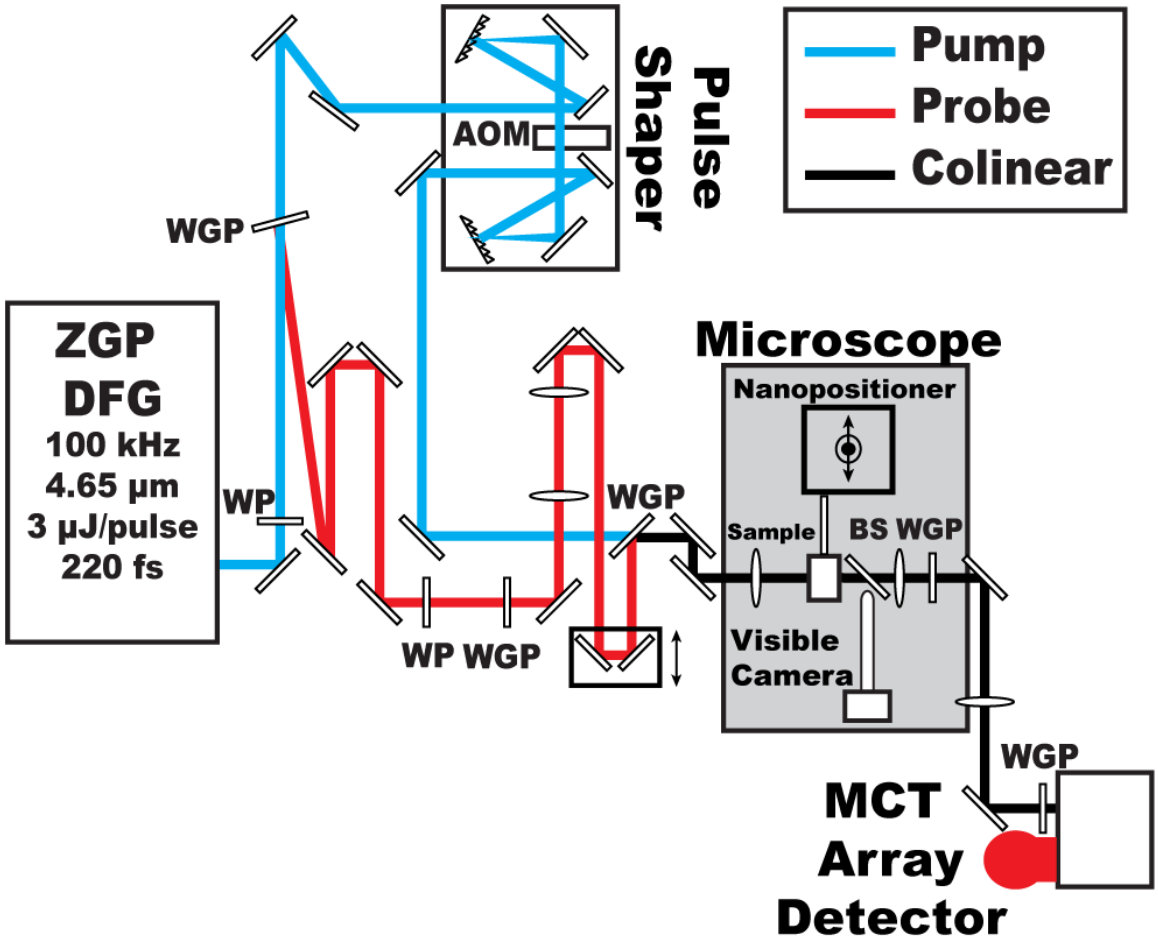

Figure 2.5 Layout of the 2D IR Microscope

The pump and probe pulses are generated in the same manner as in our 2D IR set up. A wave plate and wire grid polarier is used on the probe line to rotate the probe pulse perpendicular to the pump pulses for XXYY cross polarization geometry. The pump and probe pulses are recombined using a wire grid polarizer and focused onto the sample with a Ge/Si achromatic lens and recollomated using a Si lens. The pump pulses are eliminted using two wire grid polarizers and the probe and signal beams are detected on a MCT array detector.

2.3.9 Linear IR Absorption Spectroscopy and Microscopy

Linear IR absorption spectra were collected using a Hyperion 3000 FTIR spectrometer with OPUS software. The resolution was set to 1 cm^{-1} and 64 scans were averaged to produce each spectrum. The system was purged with dry air to remove water absorption and the spectra were processed using the atmosphere suppression corrections that are available in the OPUS software. The spectra were imported to MATLAB where background subtraction, baseline correction and normalization were performed with custom code. In order to obtain the peak positions, FWHM, and peak intensity, the spectra were fit with Gaussian line shapes also using MATLAB code.

FTIR microscopy is a tool that is used to spatially resolve linear IR absorption spectroscopy in order to observe the heterogeneous chemistry in samples. A Bruker Hyperion 3000 FTIR microscope was used to take the FTIR chemical image. It utilizes a 64 x 64 element FPA detector and a 15x objective to give a 7.6 x 7.6 μm^2 spatial resolution. A FTIR spectrum is recorded at each pixel of the image, and each of these IR spectra is integrated for a specific wavelength range and the associated absorbance is plotted as the color scale. Using the FTIR microscope images it is possible to map the presence of different chemical environments throughout the sample. The FTIR microscope image was taken in transmission mode and was processed using OPUS software (Bruker Optics).

2.4 Sample Preparation

The samples utilizing KOCN in both the static and microfluidic device experiments were 50 mM KOCN in dimethylformamide (DMF) and 50 mM KOCN in methanol. All of the molecules used for experiments in this thesis were commercially available. The KOCN, HPLC

grade N,N-Dimethylformamide (DMF), and ACS grade methanol were all used without further purification and were purchased from Sigma Aldrich. The optical densities of the samples were 0.1 and 0.56 for 50 mM KOCN in DMF and methanol, respectively. These were then combined to create a range of ratios of the different solvent environments. All experiments were performed at room temperature and the samples were placed in custom sample cells between two calcium fluoride (CaF_2) plates using 50-μm or 100-μm thick Teflon spacers in all instances that did not use microfluidic devices.

The samples utilized in the 2D IR microscopy experiments were RTIL microdroplets in silicon oil. The 1-ethyl-3-methylimidazolium tetrafluoroborate ($EmimBF_4$) and 1-ethyl-3-methylimidazolium tricyanomethanide (EmimTCM) room temperature ionic liquids (RTILs) were obtained from Iolitec and dried under vacuum for 24 hours. The dimethyl silicone oil was obtained from Thomas Scientific, SF96/50. The EmimTCM is doped into the EmimBF4 in a 1:500 volume ratio where TCM^- acts as a vibrational probe. A roughly spherical droplet is formed when a very small amount of RTIL (10-20 nL) is dropped onto silicon oil on the CaF_2 plate. The droplet becomes a pancake in shape when placed in between two CaF_2 substrates. The oil is used for stabilization of the RTIL microdroplet as well as removing scatter from the interface because the refractive index of the silicon oil is similar to the RTIL microdroplet.

2.5 Spectroscopy Methods and Concepts

2.5.1 Linear IR Absorption Spectroscopy

Linear IR spectroscopy experiments are a tool that can be used to examine complex environments by monitoring the fundamental vibrations associated with a molecule. Differences in the structure, hydrogen bonding, and solvent environments of the molecules in the ensemble

can contribute to the differences in the line shape of the absorption spectrum. For example, the line width of a linear IR absorption spectrum is determined by the homogeneous and inhomogeneous contributions to the line shape.[10] A cartoon example of homogenous and inhomogeneous contributions to linear IR absorption spectra can be seen in Figure 2.6. In homogeneous conditions, a molecular probe can sample all possible configurations of solvent arrangements in the vibrational lifetime of the probe. If a solution is completely homogenous, the absorption spectrum linewidth is narrow at an intrinsic width dictated by the vibrational lifetime. An example of this is having a probe molecule that is not interacting with the surrounding solvent environment and which quickly rearranges around the probe molecule. If the molecules do not sample all possible configurations within the vibrational lifetime of the probe, there is a distribution of frequencies. If the probe is sampling a number of different solvent configurations, which cause the frequency of the probe to fluctuate, the result is a broader absorption peak.

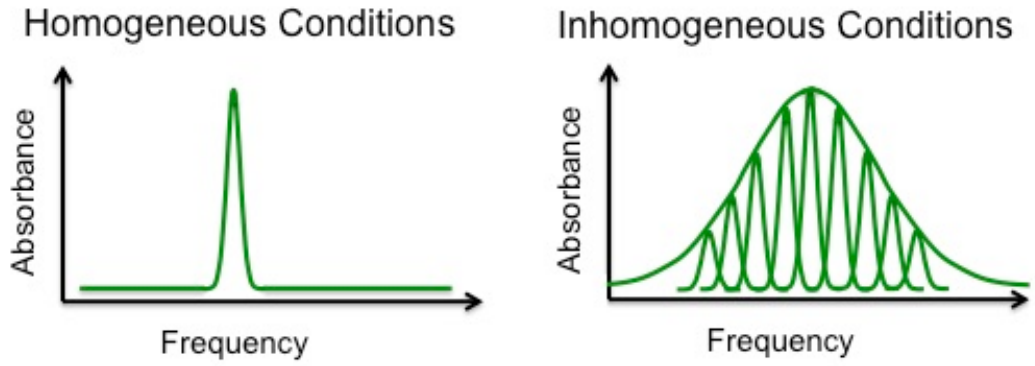

Figure 2.6 Homogenous vs Inhomogenous Conditions
Homogenous and inhomogeneous contributions to linear IR absorption spectra.

2.5.2 2D IR Spectroscopy

2D IR spectroscopy utilizes a three-pulse sequence in which three ultrafast, mid-IR pulses interact with the sample, emitting a third order signal, as seen in Figure 2.7. The first two

pump pulses, E_1 and $E_{2,}$, in the sequence are separated by time τ, while the second pump pulse and third probe pulse, E_3, are separated by a waiting time, T_w. These three fields interact with the sample to generate a signal, E_{sig}, as a function of time.[11]

A 2D IR spectrum presents as a 3D plot with two frequency axes and signal intensity. The X-axis, or probe frequency axis ω_{probe}, in the spectrum is obtained from the absorption spectrum of the probe by spectrally resolving the signal pulses using a monochromator. The Y-axis, or the pump frequency axis, ω_{pump}, is obtained by scanning the time τ and then taking the Fourier transform of the collected signal. The Fourier transform moves the signal from the time domain to the frequency domain. Thus, the 2D IR spectrum is plotted as ω_{pump} as a function of ω_{probe} and is a three dimensional plot where intensity information is held in the z-axis. An example of a 2D IR spectrum can be seen in Figure 2.3. Each individual spectrum is measured for one fixed waiting time, T_w, and the entire process is performed again for subsequent T_w measurements.[11]

2.5.3 Deciphering a 2D IR Spectrum

In order to decipher the resulting 2D IR spectrum, the example spectrum in Figure 2.7 will be used as a reference. The first pulse, E_1, interacts with the vibrational oscillators in the sample whose vibrational modes are located within the frequency range of the pulse. The interaction of E_1 puts those oscillators into a coherent superposition state consisting of the vibrational ground state (0) and first vibrational excited state (1). All of the oscillators in the

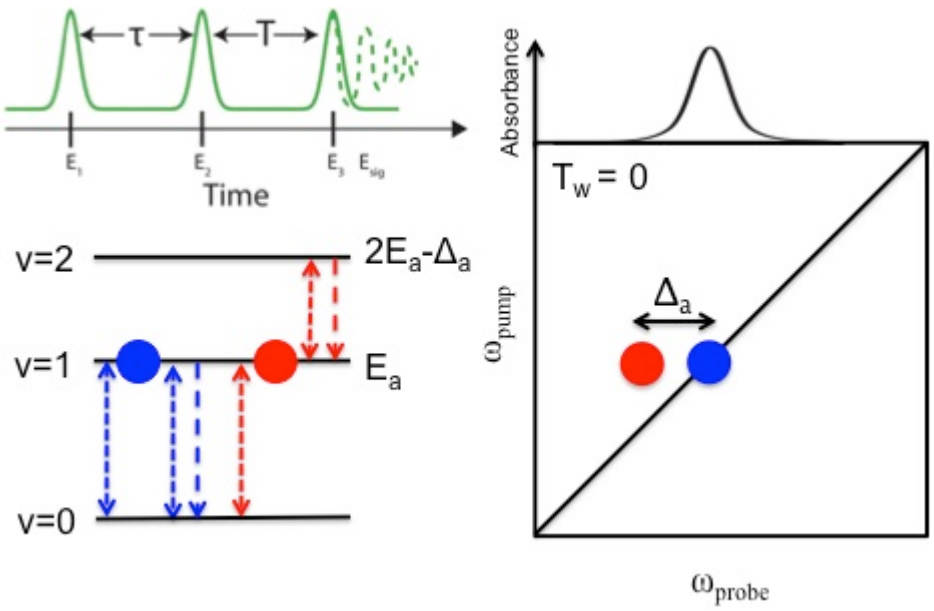

Figure 2.7 Deciphering a 2D IR Spectrum

The sequence of pulses sent into a sample in a 2D IR experiment as a function of time and a cartooned energy level diagram and 2D IR spectrum illustrating the pathways that lead to the on diagonal and off diagonal peaks.

system start by oscillating in phase, but the phase relation between them will rapidly decay over time τ. The second pulse, E_2, arrives after the delay time, τ, and takes the oscillators from a coherent superposition of vibrational states to a population of vibrational states. This means that the vibrational oscillators are either in the ground or first excited vibrational state.[12] The third pulse, E_3, will put the vibrational oscillators into a coherent superposition of states and the signal will be emitted.[11] A coherence state between the ground and first excited vibrational state after E_3, leads to a stimulated emission shown as an on diagonal peak. A coherence state between the first and second excited vibrational state can also be created. In this case the signal is emitted at a probe frequency that is slightly lower than the pump frequency. The difference in frequency between the two peaks is what is known as the diagonal anharmonic frequency, and it comes from the anharmonicity of the potential energy surface.

T waiting experiments, where multiple spectra are taken at a series of T_w steps, are exemplary of the time resolution inherent in 2D IR experiments. Steps will typically be taken in 100 - 200 fs steps out to length scales of 1 to 10s of picoseconds. Having access to femtosecond and picosecond time scales allows for the extraction of dynamics information measurable with 2D IR. This allows the quantitative measurement of things such as solvent dynamics, chemical exchange, hydrogen bonds breaking, and forming and vibrational coherence transfer.

2.5.4 Measuring Solvent Dynamics with 2D IR Spectroscopy

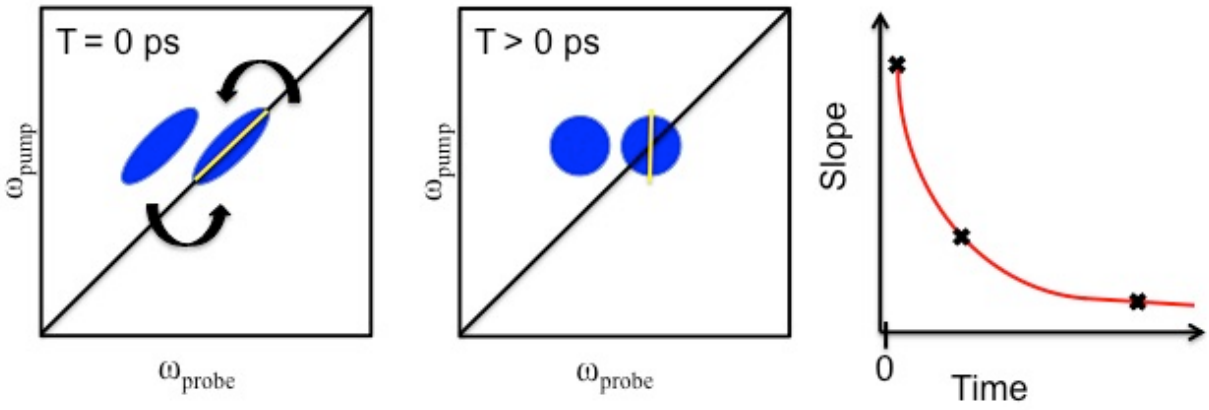

Figure 2.8 Illustration of Waiting Time Experimental Data
A cartoon illustration of the evolution of a 2D IR spectrum as a function of waiting time and the resulting decay in slope plotted as a function of time.

In order to measure dynamics with 2D IR, waiting time experiments are performed that vary T_w. A cartoon illustration of these experiments can be seen in Figure 2.8. At T_w of zero, no time is allowed for the solvent environments to rearrange following the pump pulses. In a bulk system, there are a large number of probe molecules in the laser focus sitting in different environments with different instantaneous frequencies. Measuring a bulk system at early T_w results in a 2D IR spectrum with a number of overlapping cross peak pairs, which combine to

form an elongated peak along the diagonal. As T_w is scanned out to times greater than zero, the solvent environments are allowed time to evolve after the pumping of the system, thus the probe molecules can sample the different environments present. Therefore, a vibrational mode that was pumped at one frequency may be probed at another frequency due to the rearrangement of the solvent environment, thus causing a reorientation of the 2D IR spectrum towards a circular shape of the diagonal peak pair. By measuring this reorientation at different T-waiting times one is able to quantitatively measure the spectral diffusion dynamics present in the system. From this information parameters such as correlation times and the fluctuation amplitudes of the frequency-frequency correlation function (FFCF) can be defined. These parameters can directly reveal the time-scale of the motion of the solvent molecules directly influencing the vibrational probe.[13–15]

A number of different methods can be used to characterize the reorientation of the spectral shape in T-waiting experiments, including nodal line slope and center line slope (CLS) analysis[10,14–17]. In nodal line slope analysis, the values of the slope of the nodal line between the positive and negative peaks in the 2D IR spectra are plotted as a function of T_w. In CLS analysis, slices are made along the probe frequency axis. The points of maximum value of the intensity on the diagonal peak or the off diagonal peak are measured and recorded for each lice over the FWHM region of the peak. These points are fit to a line, and the resulting slope is plotted as a function of T_w. These decays can then fit to exponential or biexponential functions following the model,

$$C(T_W) = a_1 exp(-T_W/\tau_1) + a_2 exp(-T_W/\tau_2) + b \qquad (2.4)$$

Spectral diffusion describes the process where the movement of solvent molecules surrounding the vibrational probe changes the distribution of vibrational frequencies. The time components found in the waiting time experiments indicate the dynamics of spectral diffusion.

References

(1) Erny, C.; Gallmann, L.; Keller, U. High-repetition-rate Femtosecond Optical Parametric Chirped-pulse Amplifier in the Mid-infrared. *Appl. Phys. B* **2009**, *96* (2-3), 257–269.

(2) Thai, A.; Hemmer, M.; Bates, P. K.; Chalus, O.; Biegert, J. Sub-250-mrad, Passively Carrier–envelope-phase-stable Mid-infrared OPCPA Source at High Repetition Rate. *Opt. Lett.* **2011**, *36* (19), 3918.

(3) Moses, J.; Huang, S.-W.; Hong, K.-H.; Mücke, O. D.; Falcão-Filho, E. L.; Benedick, A.; Ilday, F. ö.; Dergachev, A.; Bolger, J. A.; Eggleton, B. J.; et al. Highly Stable Ultrabroadband mid-IR Optical Parametric Chirped-pulse Amplifier Optimized for Superfluorescence Suppression. *Opt. Lett.* **2009**, *34* (11), 1639.

(4) Heese, C.; Phillips, C. R.; Mayer, B. W.; Gallmann, L.; Fejer, M. M.; Keller, U. 75 MW Few-cycle Mid-infrared Pulses from a Collinear Apodized APPLN-based OPCPA. *Opt. Express* **2012**, *20* (24), 26888–26894.

(5) Chalus, O.; Bates, P. K.; Smolarski, M.; Biegert, J. Mid-IR Short-pulse OPCPA with micro-Joule Energy at 100kHz. *Opt. Express* **2009**, *17* (5), 3587.

(6) Luther, B. M.; Tracy, K. M.; Gerrity, M.; Brown, S.; Krummel, A. T. 2D IR Spectroscopy at 100 kHz Utilizing a Mid-IR OPCPA Laser Source. *Opt. Express* **2016**, *24* (4), 4117–4127.

(7) Backus, S.; Iii, C. G. D.; Murnane, M. M.; Kapteyn, H. C. High Power Ultrafast Lasers. *Rev. Sci. Instrum.* **1998**, *69* (3), 1207–1223.

(8) Powers, P. E. *Fundamentals of Nonlinear Optics*; CRC Press, 2011.

(9) Koechner, W. *Solid-State Laser Engineering*; Springer, 2006.

(10) Hamm, P.; Zanni, M. *Concepts and Methods of 2D Infrared Spectroscopy*; Cambridge University Press, 2011.

(11) Zheng, J.; Kwak, K.; Fayer, M. D. Ultrafast 2D IR Vibrational Echo Spectroscopy. *Accounts Chem. Res.* **2007**, *40* (1), 75–83.

(12) Zheng, J.; Fayer, M. D. Hydrogen Bond Lifetimes and Energetics for Solute/solvent Complexes Studied with 2D-IR Vibrational Echo Spectroscopy. *J. Am. Chem. Soc.* **2007**, *129* (14), 4328–4335.

(13) Shin, J. Y.; Yamada, S. A.; Fayer, M. D. Dynamics of a Room Temperature Ionic Liquid in Supported Ionic Liquid Membranes Vs the Bulk Liquid: 2D IR and Polarized IR Pump–Probe Experiments. *J. Am. Chem. Soc.* **2017**, *139* (1), 311–323.

(14) Roberts, S. T.; Loparo, J. J.; Tokmakoff, A. Characterization of Spectral Diffusion from Two-dimensional Line Shapes. *J. Chem. Phys.* **2006**, *125* (8), 084502.

(15) Kwac, K.; Cho, M. Molecular Dynamics Simulation Study of N-methylacetamide in Water. II. Two-dimensional Infrared Pump–probe Spectra. *J. Chem. Phys.* **2003**, *119* (4), 2256–2263.

(16) Kuroda, D. G.; Singh, P. K.; Hochstrasser, R. M. Differential Hydration of Tricyanomethanide Observed by Time Resolved Vibrational Spectroscopy. *J. Phys. Chem. B* **2013**, *117* (16), 4354–4364.

(17) Koziński, M.; Garrett-Roe, S.; Hamm, P. Vibrational Spectral Diffusion of CN− in Water. *Chem. Phys.* **2007**, *341* (1-3), 5–10.

(18) Lin, Q.; Zhang, J.; Piredda, G.; Boyd, R. W.; Fauchet, P. M.; Agrawal, G. P. Dispersion of Silicon Nonlinearities in the Near Infrared Region. *Appl. Phys. Lett.* **2007**, *91* (2), 021111.

(19) Rick Trebino. *Frequency-Resolved Optical Gating: The Measurement of Ultrashort Laser Pulses*; Kluwer Academic Publishers: Norwell, Massachusetts, 2000.

(20) Hillegas, C. W.; Tull, J. X.; Goswami, D.; Strickland, D.; Warren, W. S. Femtosecond Laser Pulse Shaping by Use of Microsecond Radio-frequency Pulses. *Opt. Lett.* **1994**, *19* (10), 737–739.

(21) Kaindl, R. A.; Wurm, M.; Reimann, K.; Hamm, P.; Weiner, A. M.; Woerner, M. Generation, Shaping, and Characterization of Intense Femtosecond Pulses Tunable from 3 to 20 Mm. *J. Opt. Soc. Am. B, JOSAB* **2000**, *17* (12), 2086–2094.

(22) Shim, S.-H.; Strasfeld, D. B.; Fulmer, E. C.; Zanni, M. T. Femtosecond Pulse Shaping Directly in the mid-IR Using Acousto-optic Modulation. *Opt. Lett.* **2006**, *31* (6), 838–840.

(23) Shim, S.-H.; Zanni, M. T. How to Turn Your Pump–probe Instrument into a Multidimensional Spectrometer: 2D IR and Vis Spectroscopiesvia Pulse Shaping. *Phys. Chem. Chem. Phys.* **2009**, *11* (5), 748–761.

(24) Barich, M. V.; Krummel, A. T. Polymeric Infrared Compatible Microfluidic Devices for Spectrochemical Analysis. *Anal. Chem.* **2013**, *85* (21), 10000–10003.

Chapter 3

2D IR Spectroscopy at 100 kHz Utilizing a Mid-IR OPCPA Laser Source

This chapter is a publication from 2015 and is published in Optics Express.[1] I contributed to this work by helping with build the 100 kHz mid-IR OPCPA laser source and 2D IR spectrometer, data collection for the FROGs and 2D IR spectra, and sample preparation. In this publication we presented for the first time a 2D IR spectrometer operating at 100 kHz.

3.1 Introduction

The generation of ultrafast pulses in the mid-infrared (mid-IR) is of interest for many applications including spectroscopy, microscopy, and high harmonic generation (HHG)[2–9]. More specifically, nonlinear optical spectroscopies, including vibrational sum frequency generation (VSFG) spectroscopy, two-dimensional infrared (2D IR) spectroscopy, and three dimensional infrared (3D IR) spectroscopy continue to provide important information regarding chemical structure and chemical dynamics of molecules in the condensed phase[2–5,10–12]. Recently, efforts have been made to spatially resolve third order signals produced during a 2D IR spectroscopy experiment, thus demonstrating the feasibility of ultrafast 2D IR microscopy[6]. Currently these experiments rely on Ti:sapphire laser systems and optical parametric amplification to produce ultrafast optical pulses in the mid-IR. While one to several kHz optical parametric amplifiers (OPAs) based on Ti:sapphire have been the workhorse for mid-IR ultrafast pulse generation[13–16], advances in diode pumped ytterbium (Yb) oscillators and amplifiers can provide more cost effective, efficient, and space saving solutions as well as providing much needed higher repetition rates[17–20]. Advances in periodically poled nonlinear crystals have allowed for the

availability of high gain OPAs and optical parametric oscillators (OPOs) that can be pumped in the near IR[21–28]. In this paper we demonstrate 2D IR spectroscopy at 100 kHz for the first time. The 100 kHz 2D IR spectrometer is based on an optical parametric chirped-pulse amplifier (OPCPA) utilizing magnesium doped periodically poled lithium niobate (MgO:PPLN) followed by difference frequency generation (DFG) in zinc germanium diphosphide (ZGP). The system design features diode pumping of a Yb fiber oscillator and cryocooled Yb: yttrium aluminum garnet (Yb:YAG) amplifiers. A single oscillator source generates both the seed and pump beams for the OPCPA stages allowing for low jitter operation of the system. Cryocooling of the regenerative amplifier allows for high efficiency, high repetition rate operation of the OPCPA. The system takes advantage of the high efficiency and simple operation of quasiphase matched MgO:PPLN as the OPO and OPCPA gain mediums. The 1.68 μm output from the MgO:PPLN OPO is amplified in three stages and the resulting signal and idler beams are compressed. The compressed OPCPA signal and idler beams are used for DFG in ZGP generating 4.65 μm mid-IR output. The 2D IR spectrometer uses high speed pulse shaping and data collection to generate 2D IR spectra in millisecond timescales.

3.2 Methods

3.2.1 Front End and Regenerative and Multi-Pass Amplifier

The general layout for the OPCPA system is shown in Figure 3.1. The system begins with an All Normal Dispersion (ANDi)[17] Ytterbium-Fiber mode locked oscillator (KM Labs Y-Fi). The Y-Fi acts as the common source in the system, used to generate both the pump and seed pulses for the OPCPA stages. The timing for the system is based on the 63 MHz Y-Fi pulse train,

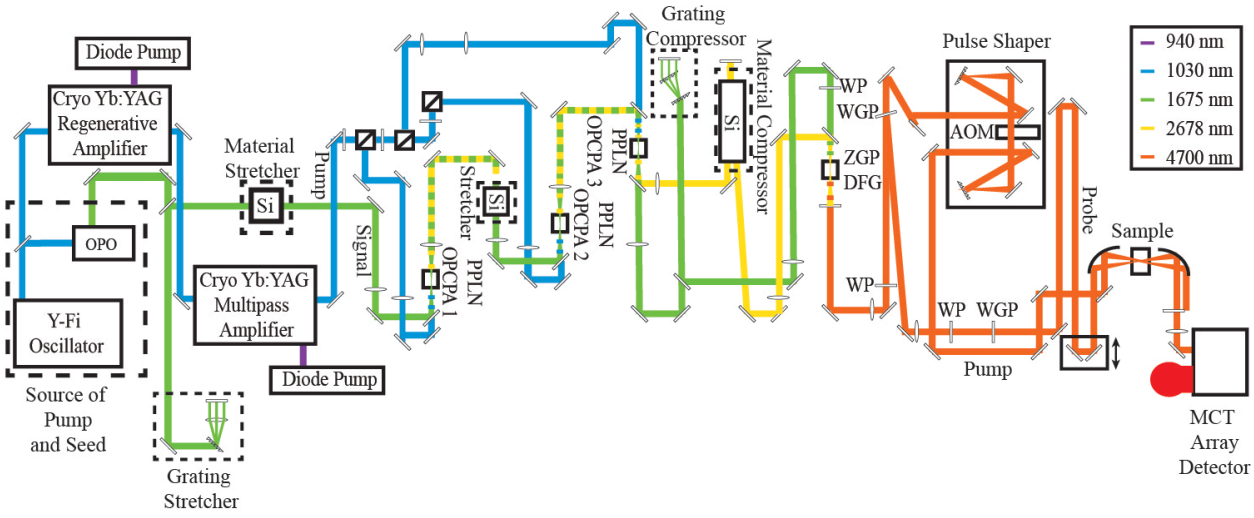

Figure 3.1 Layout of 2D IR Spectrometer

The output from the Y-Fi oscillator seeds the regenerative amplifier and pumps a MgO:PPLN OPO generating the pump and signal beams of the OPCPA respectively. The OPO output is stretched and amplified in three stages of MgO:PPLN and the resulting signal and idler are compressed in a grating and Si compressor, respectively. The compressed beams are then used as the pump and signal beams in a ZGP DFG stage generating a 4.65 μm idler. The ZGP idler is split with one line sent to a pulse shaper to generate the pump pulse pair and the second line used as the probe line in a 2D IR spectrometer.

which is divided to 50 or 100 kHz and sent to a digital delay generator to control the timing of the rest of the OPCPA system. The Y-Fi produces chirped picosecond pulses with approximately 8 nJ per pulse and 20 nm FWHM centered at 1040 nm. Approximately 7.5 nJ of the Y-Fi output is compressed to 200 fs using an 84% efficient transmission grating compressor and sent to pump a MgO:PPLN based optical parametric oscillator (OPO). The OPO contains a 3 mm long, 0.5 mm aperture MgO:PPLN crystal (Covesion Ltd.) designed for the generation of signal beams in the 1400 nm to 1700 nm range. A quarter inch thick UV fused silica window is used in the OPO cavity at Brewster's angle to provide dispersion compensation, and a PID controlled piezoelectric mirror is used to maintain cavity length stability. Using a 15% output coupler and centering the OPO at 1.68 μm results in pulses that are 170 fs in duration and ~200 pJ of energy

per pulse. The use of an OPO to generate seed pulses for the OPCPA amplifiers results in a ~10 to 20 times increase in seed power compared to the use of difference frequency generation; this approach is useful for decreasing optical parametric generation (OPG)[21,29,30].

The remaining uncompressed ~500 pJ pulses from the Y-Fi are amplified in a cryogenically cooled Yb:YAG based regenerative amplifier. The advantages of cryogenically cooled Yb:YAG are well known and include increased gain, decreased saturation fluence, and improved thermal performance allowing for high repetition rate operation[31,32] as well as allowing for the future scaling of OPCPA systems to higher average powers[33,34]. The increased gain comes at the expense of reduced emission line width, which is approximately 1 nm FWHM. The narrow emission line width coupled with gain narrowing from the ~$2x10^5$ amplification can be exploited to remove the need for stretching and recompression of the OPCPA pump pulses[20]. The output of a 940 nm continuous wave diode laser that is fiber coupled through a 400 μ m diameter fiber is focused onto the Yb:YAG using a f = 15 mm spherical collimating lens at the fiber output and a 2 inch diameter f = 100 mm aspheric focusing lens. The resulting pump beam has a FWHM of ~600 μm in the Yb:YAG. The pump beam is sent through a 2 inch dichroic mirror that reflects the 1030 nm cavity beam while transmitting the 940 nm pump beam. A 5 mm long, AR coated, 8% doped Yb:YAG crystal is cooled to −243°C using a cryorefrigerator (Cryomech Inc.). The crystal is held in a copper cold finger inside of an evacuated cell (1 μTorr) pumped by a 2 L/s ion pump. The cavity is a folded confocal "X" design with two f = 500 mm lenses separated by 1300 mm giving a calculated TEM_{00} ω_0 of 433 μm. A high repetition rate Pockels cell (Bergmann Meßgeräte Entwicklung KG) is used to switch the seed pulses in and out of the regenerative amplifier. The blue edge of the Y-Fi spectrum is overlapped with the gain of

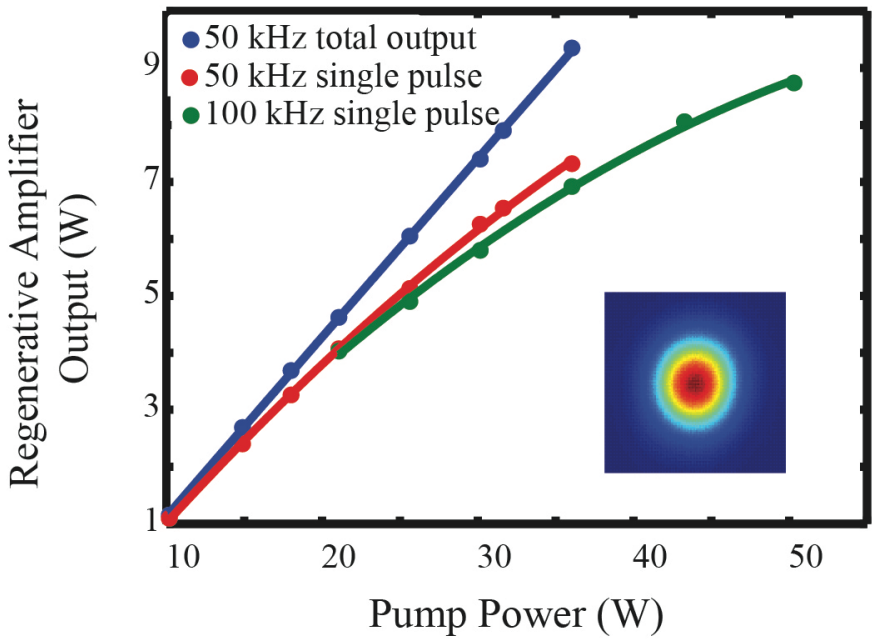

Figure 3.2 Regenerative Amplifier Output

Output energies vs. pump power for the cryocooled Yb:YAG regenerative amplifier. The blue curve shows 50 kHz operation including the main and post pulses, while the red curve shows the output power at 50 kHz in the main pulse alone after the cleanup Pockels cell. The green curve shows the output power in the main pulse alone for 100 kHz. The inset shows the spatial profile of the regenerative amplifier taken at 30 W pump.

the cryogenically cooled Yb:YAG by tuning the birefringent filter in the free space section of the Y-Fi[17].

Amplification to 60 μJ/pulse results in bandwidth limited 10 ps output pulses from the regenerative amplifier. Period doubling is observed from the regenerative amplifier, but single pulse operation is obtained by reducing the number of cavity round trips while increasing the pump power[35,36]. Post-pulses from the regenerative amplifier are removed with a high repetition rate Pockels cell following the regenerative amplifier. Output energies versus pump power for 50 and 100 kHz operation utilizing 22 round trips are shown in Figure 3.2 along with an inset showing the output spatial mode. The total output energy, including post pulses, at 50 kHz is

linear with pump energy, while the energy making it through the cleanup Pockels cell falls as a function of pump power due to increasing post pulse buildup at high pump powers. This is likely due to the increased gain and depolarization at high pump powers. Pulse energies up to 146 μJ (7.3W) and 87 μJ (8.7 W) were obtained at 50 kHz and 100 kHz, respectively.

The output from the clean-up Pockels cell is amplified in a cryogenically cooled, two pass, Yb:YAG power amplifier. The Yb:YAG cryo-head is identical to the one used in the regenerative amplifier described above. A two times down telescope is used to collimate the input seed beam to 1 mm FWHM. The output of a 250 W, fiber coupled, 940 nm continuous wave diode laser is imaged onto the Yb:YAG crystal, the 2.5 magnification of the 400 μm diameter fiber results in a 1mm flat-top pump profile. The pump beam is sent through a 2 inch dichroic mirror that reflects the 1030 nm beam while transmitting the 940 nm pump beam. The amplified beam double passes a quarter waveplate and is ejected using a cube polarizer.

The results for the output of the two pass amplifier at 100 kHz as a function of pump power are shown in Figure 3.3. Output energies of up to 695 μJ (69.5 W) are obtained with the output beam divergence increasing with pump power due to thermal lensing in the Yb:YAG crystal. The output of the power amplifier is sent to a one to one telescope for re-collimation before being sent to the OPCPA.

3.2.2 OPCPA

The OPCPA design utilizes three stages of amplification with 3 mm long, 1 mm aperture MgO:PPLN crystals (Covesion Ltd.) for the first two stages and a 3 mm long, 3 mm x 5mm aperture MgO:PPLN crystals (HCP) for the third stage. The 1.68 μm output from the OPO is

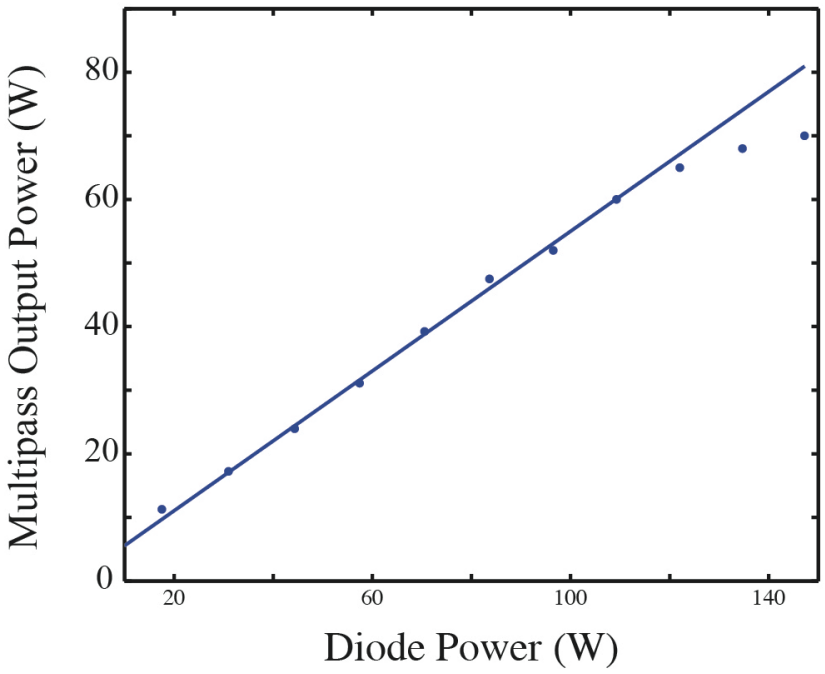

Figure 3.3 Multi-Pass Amplifier Output

Output energies vs. pump power for the cryocooled Yb:YAG multi-pass amplifier. The blue curve shows 100 kHz operation. A linear fit to the low energy points is included to show loss of efficiency due to thermal lensing.

used as the seed beam in the first stage amplifier. The amplified 1.68 μm signals from the first and second stage amplifiers are kept and sent to seed the next stage amplifiers, while the idlers are discarded. The signal and idler from the third stage amplifier are separated with a dichroic mirror and sent for compression. The 1 mm aperture MgO:PPLN crystals have discrete poling periods ranging from 29.52 μm to 31.59 μm and are AR coated for the pump, signal and idler beams. The 30.49 μm MgO:PPLN period was used at 115° C for amplification at 1.68 μm. The 3 x 5 mm aperture MgO:PPLN crystal had two poling periods equal to 30.5 μm and 30.8 μ m. Output bandwidths from periodically poled crystals decrease with crystal length and 3 mm lengths were chosen to optimize the amplification bandwidth of the 1.68 μm OPO pulses. Output

bandwidths are also controlled by the temporal overlap of the pump and chirped seed pulses as well as by gain saturation and back conversion[21].

During the OPCPA amplification process the 2.67 μm idler is generated with a phase that is opposite in sign from the 1.68 μ m signal beam for the group velocity dispersion (GVD) and fourth order dispersion (FOD) while the same in sign for the third order dispersion (TOD)[37]. This creates a problem when using standard grating stretchers as all three orders will be negative for the generated idler and use of a positive GVD grating compressor will result in the TODs being additive[38]. The use of a material compressor with all positive orders is a possible solution but cancelation of the third order is difficult due to the higher ratio of TOD to GVD in gratings versus materials. In order to tune the TOD to GVD ratio of the 1.68 μm seed to match the TOD to GVD ratio of a 2.67 μm material compressor we used a combination grating and material stretcher. In this way the 1.68 μm material and grating GVDs are both positive giving the desired 2.7 ps stretch, while the negative TOD of the grating stretcher is partially cancelled by the positive TOD of the Si material stretcher. The final design uses a folded double pass grating stretcher along with 125 mm of silicon to stretch the 1.68 μm signal pulses and 500 mm silicon to compress the 2.67 μm idler pulses. In this way tunability is maintained for the stretcher GVD while taking advantage of high throughput of the silicon compressor for the OPCPA idler. The stretcher utilizes an uncoated 940 l/mm transmission grating (LightSmyth Technologies) with a 51.9° input angle and 1.5 mm path length. The 1.68 μm signal pulses are compressed with a traditional transmission grating stretcher using a lower groove density (600 l/mm) to match the TOD to GVD ratio generated by the combination grating and material stretcher.

For the first stage OPCPA 6.5 μJ of the 1029.7 nm amplified output is split off using a half waveplate and polarizing cube. The pump beam is focused to a 90 μm FWHM spot size on

the MgO:PPLN resulting in a 6 GW/cm^2 pump intensity. The 1.68 μm OPO output is sent through the grating stretcher and 100 mm of silicon prior to being collinearly overlapped with the pump using a dichroic mirror. The 1.68 μm output from the first stage amplifier is removed with a dichroic mirror and then sent to the second stage for further amplification. The ~150 pJ seed beam is amplified to ~0.5 μJ in the first stage OPCPA resulting in a gain of 3333.

In order to maximize the second stage pump energy we set the 99% intensity to 1.1 mm, slightly overfilling the 1 mm square PPLN aperture, giving a 400 μm FWHM for the 1029.7 nm pump beam. The second stage is pumped with 45 μJ (2.3 GW/cm^2), which is again split off with a half waveplate and polarizer. The amplified signal beam is again removed with a dichroic mirror resulting in a 6 μ J output and a gain of 12.

The remaining pump beam is sent to a final waveplate and polarizer that allows control of the pump power to the third stage MgO:PPLN crystal. In order to maximize the pump power on third stage we set the 99% intensity to match the 3 mm vertical clear aperture resulting in a 1 mm FWHM. While pump powers of up to 60 W are available from the multipass amplifier we did not observe significant improvements in output power from the third stage with energies higher than 35 W (2.9 GW/cm2) due to thermal effects in the MgO:PPLN crystal. The 1 mm FWHM, 6 μJ seed beam was collinearly overlapped with the pump beam using a dichroic mirror and the signal and idler beams were separated using dichroic mirrors. Amplified signal and idler output energies are shown in Figure 3.4 as a function of pump power. The third stage amplifier is pumped with 30 W resulting in 58 μJ in the seed beam at 1.68 μm and 32 μJ in the idler at 2.67 μm.

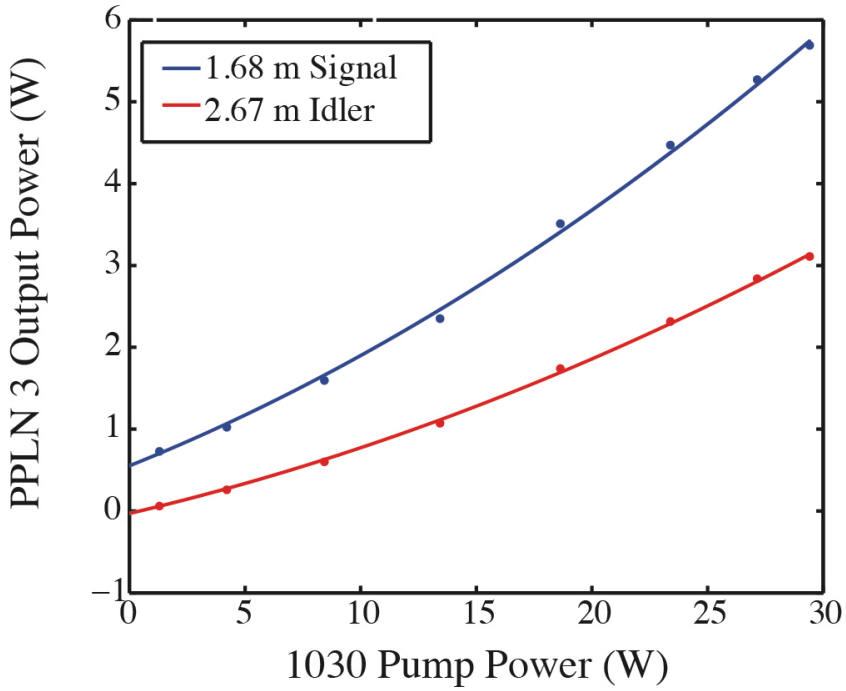

Figure 3.4 Third Stage PPLN Output

100 kHz output powers for the third stage PPLN versus 1030 nm pump power.

3.2.3 PPLN OPCPA Compression

The compressed signal and idler pulse widths were measured using a lithium niobate based FROG. The 2.67 μm idler from the third stage amplifier was collimated and double passed through an AR coated 250 mm silicon compressor with 86% single pass transmission efficiency. Silicon was chosen for its availability, low two photon absorption (above 2.2 μm), high transmission, as well as its low nonlinear index which prevents high B integrals in the compressor[39]. Compression of the 2.67 μm idler resulted in ~235 fs FWHM pulses with 17.5 μJ per pulse. The measured FROG and recovered temporal intensity and phase are shown in Figures 3.5(a) and 3.5(b), respectively.

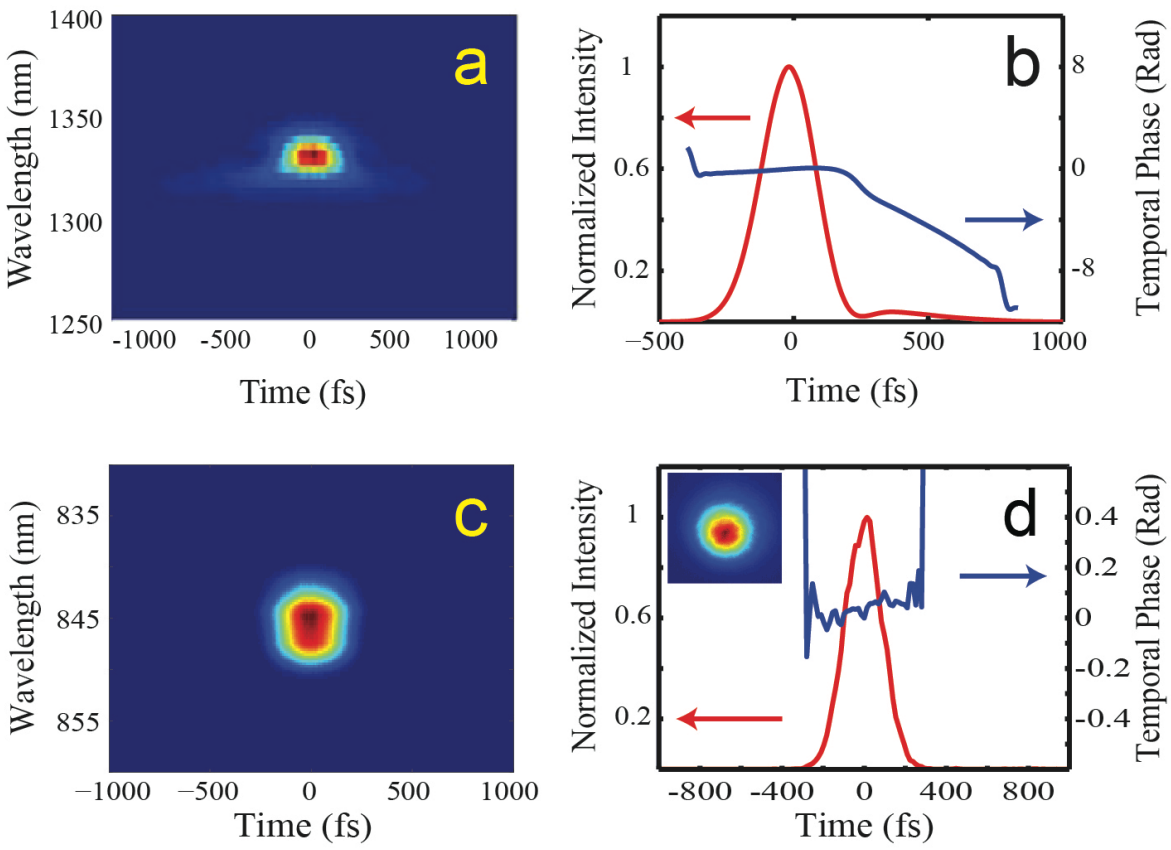

Figure 3.5 Measured FROG of Compressed Third Stage PPLN Output

a) Measured FROG of the compressed 2.67 μm idler. b) Recovered 235 fs, 2.67 μm intensity and temporal phase. c) Measured FROG of the compressed 1.68 μm signal. d) Recovered 210 fs, 1.68 μm intensity and temporal phase. Inset shows the 1.68 μm signal beam's spatial profile as observed by two photon absorption on a silicon CCD camera.

The 1.68 μm seed pulses were sent to a transmission grating compressor with an output efficiency of 60.5%. The compressor uses 600 l/mm transmission gratings (Wasatch Photonics) that can effectively compensate the GVD and TOD of the material-grating stretcher. The measured 1.68 μm FROG trace is shown in Figure 3.5(c). The recovered temporal intensity and phase are shown in Figure 3.5(d) with a 210 fs pulse length for the 36 μJ pulse. Figure 3.5(d)

includes an inset of the 1.68 μm seed beam two-photon absorption on a silicon CCD camera showing a high quality spatial mode.

3.2.4 ZGP DFG

The compressed signal and idler pulses from the MgO:PPLN OPCPA are recombined in a Zinc Germanium Diphosphide (ZGP) DFG. ZGP is of great interest due to its high damage threshold, high thermal conductivity and large nonlinear coefficient[40,41]. The pump beam at 1.68 μm is slightly bluer than the usual ~2 μm pump used in ZGP and absorption of the pump beam along with temporal walkoff are potential problems. The ZGP crystal is limited to 0.5 mm path length for the reasons given above resulting in a 150 fs walkoff for the pump and idler beams over the length of the crystal. The measured total transmission loss for the AR/AR coated crystal at 1.68 μm was 10.7% while the power in the back reflections from the AR coatings was measured at ~9.7% of the input pump beam. The 73° cut ZGP crystal is used in a type I configuration which is accomplished by rotating the pump beam with a variable wavelength half waveplate (Alphalas) to "p" polarization while leaving the 2.67 μm beam in its original "s" polarization. The pump and signal beams are collinearly overlapped with a dichroic mirror and reduced to 750 and 790 μm spot sizes respectively, giving peak intensities of 1.9×10^{10} W/cm^2 for the 27 μJ pump and 6.8×10^{9} W/cm^2 for the 12 μJ seed. The idler at 4.65 μm is removed with a long pass filter giving 3 μJ output shown in Figure 3.6(a). The idler from the ZGP is sent to a pulse shaper and 2D IR spectrometer described below. A collinear second harmonic generation FROG[42], shown in Figure 3.6(b), was collected using the pulse shaper and a silver gallium sulfide crystal (type I, theta = 32°, phi = 45°, Eksma) resulting in 220 fs reconstructions shown in Figure 3.6(c).

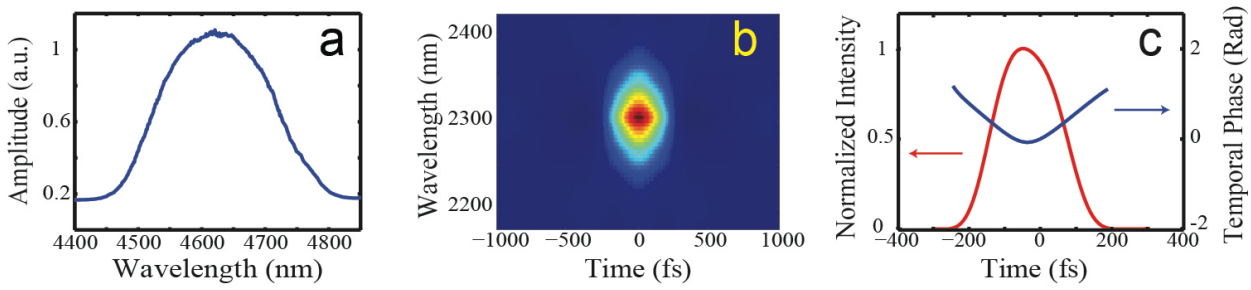

Figure 3.6 Measured ZGP Idler Output

a) Measured ZGP idler spectrum b) Measured collinear FROG of the 4.65 μm ZGP idler. c) Recovered 220fs, 4.65 μm intensity and temporal phase with a 220 fs FWHM.

3.2.5 Pulse Shaping and 2D IR measurements

The idler from the ZGP DFG is collimated and sent to a 2D IR spectrometer shown in Figure 3.1. A variable wavelength half waveplate (Alphalas) and wire grid polarizer are used to generate the probe and pump lines. The reflected beam from the polarizer is sent to the probe line of the 2D IR spectrometer while the transmitted beam is sent to a mid-IR pulse shaper (PhaseTech Spectroscopy). Rotation of the waveplate allows variable control of the power sent to the probe and pump lines. The pulse shaper uses a germanium acusto-optic modulator in the Fourier plane of a 4f Martinez stretcher to generate pump pulse pairs at 100 kHz with variable delay and phase[43–45]. The shaper has 40% efficiency at 4.65 μm and the 275 nJ pump pulses were reduced to 40 nJ by reducing the amplitude of the acoustic wave in the shaper. This was done in order to find the lowest pump energy that provided high signal to noise in the 2D IR spectra and is of interest for future experiments where the tunability of the ZGP DFG stage will be examined based on continuum generation of the 2.67 μm idler pulses. It is also of interest for the investigation of thermal effects that will limit the repetition rate available for 2D IR

spectroscopy. We note that the average power used in these experiments is not higher than 1 kHz 2D IR experiments using 300 nJs per pulse or greater. The probe pulse energy was set to 30 nJ using the half waveplate. The pump pulse pairs are generated using a two phase cycle S($\Delta\varphi_{12}$ = 0)–S($\Delta\varphi_{12}$ = π) pump scheme[46] and sent to a four inch focal length, 90° off axis parabola that focuses the beam into a CaF_2 sample cell. The probe beam is sent through a second waveplate and polarizer to allow the probe pulse polarization orientation to be chosen before being overlapped in the sample cell with the pump pulse pair. The pump and probe polarizations were both set to "p" for the 2D IR experiments.

After leaving the sample cell, the probe beam is sent to a 100 kHz, linear 64 element, gated mercury cadmium telluride (MCT) mid-IR spectrometer (Infrared Systems Development, FPAS). The high speed of the MCT array and shaper allows for continuous collection of each laser shot. 2D IR experiments were preformed using a 100-μm-thick CaF_2 cell filled with 12.5 mM potassium cyanate (KOCN) in HPLC grade N,N-dimethylformamide (DMF) resulting in a OD of 0.38 at 2136 cm^{-1}. The experiments were performed at room temperature. Both the KOCN and DMF were purchased from Sigma-Aldrich and used without purification. Figure 3.7 shows the 2D IR spectra of KOCN in DMF for a single spectrum (Figure 3.7(a)), a 20 spectrum average (Figure 3.7(b)), and a 100 spectrum average (Figure 3.7(c)). The spectra were collected with a series of 358 pump pulse pairs delayed from 0 to 2.5 ps in 7 fs steps, using a two-step phase cycling scheme. Collection of a single spectrum requires only 7.16 ms while a 100 spectra average takes only 716 ms. This acquisition time can be potentially reduced further by utilizing a rotating frame pulse shaping sequence[46].

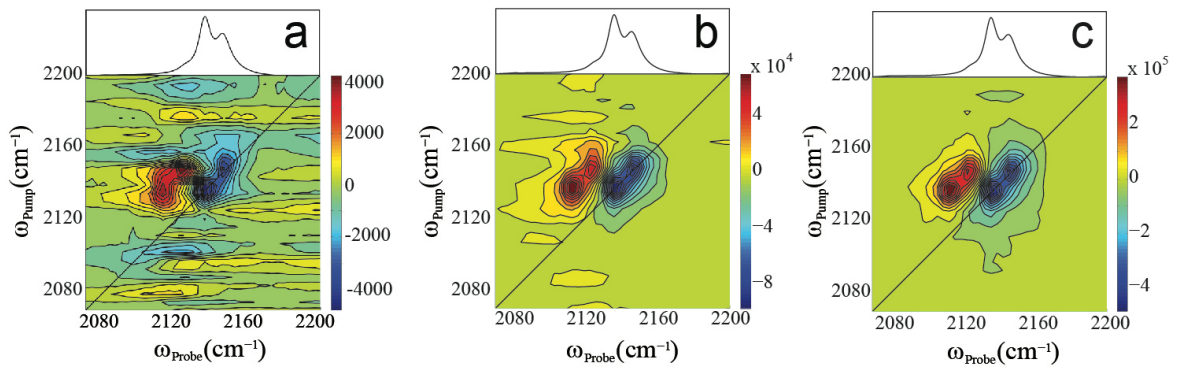

Figure 3.7 2D IR Spectra of KOCN in DMF

a) Single 2D spectrum of KOCN in DMF b) 20 spectra average. c) 100 spectra average.

3.3 Conclusion

In conclusion we have demonstrated for the first time a 100 kHz, 2D IR spectrometer. The system is based on diode pumped Yb gain materials, a three stage MgO:PPLN based OPCPA, and a ZGP DFG stage. The system utilizes an ANDi Yb fiber oscillator as the source for both the seed and pump beams of a two stage OPCPA. The cryogenically cooled Yb:YAG regenerative amplifier takes advantage of gain narrowing to allow the use of the ANDi as a seed source removing the need for electronic timing control or the use of chirped pulse amplification for the generation of the OPCPA pump. The MgO:PPLN OPCPA generates ~210 and 235 fs pulses for the seed and idler, respectively with energies suitable for IR spectroscopy at 100 kHz. The OPCPA should also allow for shorter pulse lengths with improved compression of the Y-Fi bandwidth, which supports sub-100 fs pulses. DFG between the signal and idler pulses of the OPCPA in ZGP allows for generation of mid-IR at 4.65 μm. Continuum generation using the 2.67 μm MgO:PPLN idler should allow for tunability and larger output bandwidths from the ZGP DFG in the future. We note that pulse walkoff times in the ZGP are fairly consistent out to 6 μm and improve as the idler goes from 6 to 10 μm while the ZGP deff almost doubles going

from 4.6 to 10 μm. The Ge AOM coatings of the pulse shaper should allow for tuning in the 3-8 μm range with ZGP phase matching supporting wavelengths out to 10 μm. The use of 100 kHz pulse shaping and data collection was demonstrated resulting in millisecond 2D IR spectral acquisition times. The high repetition rate 2D IR spectrometer reported here will allow for interesting experiments including 2D IR microscopy and nanoscopy.

3.4 Additional Notes

This research was supported by BP Exploration Operating Company Ltd. and the National Science Foundation (Grant No. CHE-1255658). The authors would like to acknowledge the contributions of Sterling Backus to the system design and of Matt Kirchner for contributions to the OPO design.

References

(1) Luther, B. M.; Tracy, K. M.; Gerrity, M.; Brown, S.; Krummel, A. T. 2D IR Spectroscopy at 100 kHz Utilizing a Mid-IR OPCPA Laser Source. *Opt. Express* **2016**, *24* (4), 4117–4127.

(2) Fayer, M. D. Dynamics of Liquids, Molecules, and Proteins Measured with Ultrafast 2D IR Vibrational Echo Chemical Exchange Spectroscopy. *Annu. Rev. Phys. Chem.* **2009**, *60* (1), 21–38.

(3) Hochstrasser, R. M. Two-dimensional Spectroscopy at Infrared and Optical Frequencies. *Proc. Natl. Acad. Sci.* **2007**, *104* (36), 14190–14196.

(4) Zanni, M. T.; Hochstrasser, R. M. Two-dimensional Infrared Spectroscopy: a Promising New Method for the Time Resolution of Structures. *Curr. Opin. Struct. Biol.* **2001**, *11* (5), 516–522.

(5) Woutersen, S.; Hamm, P. Nonlinear Two-dimensional Vibrational Spectroscopy of Peptides. *J. Phys. Condens. Matter* **2002**, *14* (39), R1035.

(6) Baiz, C. R.; Schach, D.; Tokmakoff, A. Ultrafast 2D IR Microscopy. *Opt. Express* **2014**, *22* (15), 18724–18735.

(7) Lewenstein, M.; Balcou, P.; Ivanov, M. Y.; L'Huillier, A.; Corkum, P. B. Theory of High-harmonic Generation by Low-frequency Laser Fields. *Phys. Rev.* **1994**, *49* (3), 2117–2132.

(8) Popmintchev, T.; Chen, M.-C.; Cohen, O.; Grisham, M. E.; Rocca, J. J.; Murnane, M. M.; Kapteyn, H. C. Extended Phase Matching of High Harmonics Driven by Mid-infrared Light. *Opt. Lett.* **2008**, *33* (18), 2128–2130.

(9) Cyran, J. D.; Krummel, A. T. Probing Structural Features of Self-assembled

Violanthrone-79 Using Two Dimensional Infrared Spectroscopy. *J. Chem. Phys.* **2015**, *142* (21), 212435.

(10) Garrett-Roe, S.; Hamm, P. Purely Absorptive Three-dimensional Infrared Spectroscopy. *J. Chem. Phys.* **2009**, *130* (16), 164510.

(11) Ding, F.; Zanni, M. T. Heterodyned 3D IR Spectroscopy. *Chem. Phys.* **2007**, *341* (1–3), 95–105.

(12) Perakis, F.; Borek, J. A.; Hamm, P. Three-dimensional Infrared Spectroscopy of Isotope-diluted Ice Ih. *J. Chem. Phys.* **2013**, *139* (1), 014501.

(13) Gruetzmacher, J. A.; Scherer, N. F. Few-cycle Mid-infrared Pulse Generation, Characterization, and Coherent Propagation in Optically Dense Media. *Rev. Sci. Instrum.* **2002**, *73* (6), 2227–2236.

(14) Holtom, G. R.; Crowell, R. A.; Xie, X. S. High-repetition-rate Femtosecond Optical Parametric Oscillator–amplifier System Near 3 Mm. *J. Opt. Soc. Am. B, JOSAB* **1995**, *12* (9), 1723–1731.

(15) Fecko, C. J.; Loparo, J. J.; Tokmakoff, A. Generation of 45 Femtosecond Pulses at 3 Mm with a KNbO3 Optical Parametric Amplifier. *Opt. Commun.* **2004**, *241* (4-6), 521–528.

(16) Petrov, V.; Rotermund, F.; Noack, F. Generation of High-power Femtosecond Light Pulses at 1 kHz in the Mid-infrared Spectral Range Between 3 and 12 Mm by Second-order Nonlinear Processes in Optical Crystals. *J. Opt. Pure Appl. Opt.* **2001**, *3* (3), R1.

(17) Chong, A.; Buckley, J.; Renninger, W.; Wise, F. All-normal-dispersion Femtosecond Fiber Laser. *Opt. Express* **2006**, *14* (21), 10095–10100.

(18) Brauch, U.; Giesen, A.; Karszewski, M.; Stewen, C.; Voss, A. Multiwatt Diode-pumped Yb:YAG Thin Disk Laser Continuously Tunable Between 1018 and 1053 Nm. *Opt. Lett.*

1995, *20* (7), 713–715.

(19) Kawanaka, J.; Yamakawa, K.; Nishioka, H.; Ueda, K. 30-mJ, Diode-pumped, Chirped-pulse Yb:YLF Regenerative Amplifier. *Opt. Lett.* **2003**, *28* (21), 2121–2123.

(20) Akahane, Y.; Aoyama, M.; Ogawa, K.; Tsuji, K.; Tokita, S.; Kawanaka, J.; Nishioka, H.; Yamakawa, K. High-energy, Diode-pumped, Picosecond Yb:YAG Chirped-pulse Regenerative Amplifier for Pumping Optical Parametric Chirped-pulse Amplification. *Opt. Lett.* **2007**, *32* (13), 1899–1901.

(21) Erny, C.; Gallmann, L.; Keller, U. High-repetition-rate Femtosecond Optical Parametric Chirped-pulse Amplifier in the Mid-infrared. *Appl. Phys. B* **2009**, *96* (2-3), 257–269.

(22) Thai, A.; Hemmer, M.; Bates, P. K.; Chalus, O.; Biegert, J. Sub-250-mrad, Passively Carrier–envelope-phase-stable Mid-infrared OPCPA Source at High Repetition Rate. *Opt. Lett.* **2011**, *36* (19), 3918.

(23) Moses, J.; Huang, S.-W.; Hong, K.-H.; Mücke, O. D.; Falcão-Filho, E. L.; Benedick, A.; Ilday, F. ö.; Dergachev, A.; Bolger, J. A.; Eggleton, B. J.; et al. Highly Stable Ultrabroadband mid-IR Optical Parametric Chirped-pulse Amplifier Optimized for Superfluorescence Suppression. *Opt. Lett.* **2009**, *34* (11), 1639.

(24) Heese, C.; Phillips, C. R.; Mayer, B. W.; Gallmann, L.; Fejer, M. M.; Keller, U. 75 MW Few-cycle Mid-infrared Pulses from a Collinear Apodized APPLN-based OPCPA. *Opt. Express* **2012**, *20* (24), 26888–26894.

(25) Galvanauskas, A.; Hariharan, A.; Harter, D.; Arbore, M. A.; Fejer, M. M. High-energy Femtosecond Pulse Amlification in a Quasi-phase-matched Parametric Amplifier. *Opt. Lett.* **1998**, *23* (3), 210–212.

(26) Myers, L. E.; Bosenberg, W. R. Periodically Poled Lithium Niobate and Quasi-phase-

matched Optical Parametric Oscillators. *IEEE J. Quantum Electron.* **1997**, *33* (10), 1663–1672.

(27) Mayer, B. W.; Phillips, C. R.; Gallmann, L.; Fejer, M. M.; Keller, U. Sub-four-cycle Laser Pulses Directly from a High-repetition-rate Optical Parametric Chirped-pulse Amplifier at 3.4 μm. *Opt. Lett.* **2013**, *38* (21), 4265–4268.

(28) Baudisch, M.; Hemmer, M.; Pires, H.; Biegert, J. Performance of MgO:PPLN, KTA, and $KNbO_3$ for Mid-wave Infrared Broadband Parametric Amplification at High Average Power. *Opt. Lett.* **2014**, *39* (20), 5802–5805.

(29) Erny, C.; Moutzouris, K.; Biegert, J.; Kühlke, D.; Adler, F.; Leitenstorfer, A.; Keller, U. Mid-infrared Difference-frequency Generation of Ultrashort Pulses Tunable Between 3.2 and 4.8 μm from a Compact Fiber Source. *Opt. Lett.* **2007**, *32* (9), 1138–1140.

(30) Chalus, O.; Bates, P. K.; Smolarski, M.; Biegert, J. Mid-IR Short-pulse OPCPA with micro-Joule Energy at 100kHz. *Opt. Express* **2009**, *17* (5), 3587.

(31) Dong, J.; Bass, M.; Mao, Y.; Deng, P.; Gan, F. Dependence of the Yb^{3+} Emission Cross Section and Lifetime on Temperature and Concentration in Yttrium Aluminum Garnet. *J. Opt. Soc. Am. B, JOSAB* **2003**, *20* (9), 1975–1979.

(32) Brown, D. C. The Promise of Cryogenic Solid-state Lasers. *IEEE J. Sel. Top. Quantum Electron.* **2005**, *11* (3), 587–599.

(33) Hong, K.-H.; Huang, S.-W.; Moses, J.; Fu, X.; Lai, C.-J.; Cirmi, G.; Sell, A.; Granados, E.; Keathley, P.; Kärtner, F. X. High-energy, Phase-stable, Ultrabroadband kHz OPCPA at 2.1 μm Pumped by a Picosecond Cryogenic Yb:YAG Laser. *Opt. Express* **2011**, *19* (16), 15538–15548.

(34) Reagan, B. A.; Wernsing, K. A.; Curtis, A. H.; Furch, F. J.; Luther, B. M.; Patel, D.;

Menoni, C. S.; Rocca, J. J. Demonstration of a 100 Hz Repetition Rate Gain-saturated Diode-pumped Table-top Soft X-ray Laser. *Opt. Lett.* **2012**, *37* (17), 3624–3626.

(35) Dörring, J.; Killi, A.; Morgner, U.; Lang, A.; Lederer, M.; Kopf, D. Period Doubling and Deterministic Chaos in Continuously Pumped Regenerative Amplifiers. *Opt. Express* **2004**, *12* (8), 1759–1768.

(36) Metzger, T.; Schwarz, A.; Teisset, C. Y.; Sutter, D.; Killi, A.; Kienberger, R.; Krausz, F. High-repetition-rate Picosecond Pump Laser Based on a Yb:YAG Disk Amplifier for Optical Parametric Amplification. *Opt. Lett.* **2009**, *34* (14), 2123–2125.

(37) Ross, I. N.; Matousek, P.; Towrie, M.; Langley, A. J.; Collier, J. L. The Prospects for Ultrashort Pulse Duration and Ultrahigh Intensity Using Optical Parametric Chirped Pulse Amplifiers. *Opt. Commun.* **1997**, *144* (1-3), 125–133.

(38) Backus, S.; Iii, C. G. D.; Murnane, M. M.; Kapteyn, H. C. High Power Ultrafast Lasers. *Rev. Sci. Instrum.* **1998**, *69* (3), 1207–1223.

(39) Lin, Q.; Zhang, J.; Piredda, G.; Boyd, R. W.; Fauchet, P. M.; Agrawal, G. P. Dispersion of Silicon Nonlinearities in the Near Infrared Region. *Appl. Phys. Lett.* **2007**, *91* (2), 021111.

(40) Boyd, G. D.; Buehler, E.; Storz, F. G. Linear and Nonlinear Optical Properties of $ZnGeP_2$ and CdSe. *Appl. Phys. Lett.* **1971**, *18* (7), 301–304.

(41) Barnes, N. P.; Williams-Byrd, J. A. Average Power Effects in Parametric Oscillators and Amplifiers. *J. Opt. Soc. Am. B* **1995**, *12* (1), 124.

(42) Amat-Roldán, I.; Cormack, I. G.; Loza-Alvarez, P.; Gualda, E. J.; Artigas, D. Ultrashort Pulse Characterisation with SHG collinear-FROG. *Opt. Express* **2004**, *12* (6), 1169–

1178.

(43) Hillegas, C. W.; Tull, J. X.; Goswami, D.; Strickland, D.; Warren, W. S. Femtosecond Laser Pulse Shaping by Use of Microsecond Radio-frequency Pulses. *Opt. Lett.* **1994**, *19* (10), 737–739.

(44) Kaindl, R. A.; Wurm, M.; Reimann, K.; Hamm, P.; Weiner, A. M.; Woerner, M. Generation, Shaping, and Characterization of Intense Femtosecond Pulses Tunable from 3 to 20 Mm. *J. Opt. Soc. Am. B, JOSAB* **2000**, *17* (12), 2086–2094.

(45) Shim, S.-H.; Strasfeld, D. B.; Fulmer, E. C.; Zanni, M. T. Femtosecond Pulse Shaping Directly in the mid-IR Using Acousto-optic Modulation. *Opt. Lett.* **2006**, *31* (6), 838–840.

(46) Shim, S.-H.; Zanni, M. T. How to Turn Your Pump–probe Instrument into a Multidimensional Spectrometer: 2D IR and Vis Spectroscopiesvia Pulse Shaping. *Phys. Chem. Chem. Phys.* **2009**, *11* (5), 748–761.

Chapter 4

High Throughput 2DIR Spectroscopy Achieved by Interfacing Microfluidic Technology with a High Repetition Rate 2D IR Spectrometer

This chapter is a publication from 2016 and is published in the Journal of Physical Chemistry Letters,[1] focusing on work performed in cooperation with Dr. Michael Barich. For this work, I worked on sample preparation, developed the process of interfacing the microfluidic devices with the 2D IR system, and performed the data analysis of the 2D IR data and FTIR microscope data.

4.1 Introduction

Pseudo-halide anions are of particular interest due to their potential as site-specific markers in proteins and their utility as a model system to investigate the formation of contact ion pairs in bulk solvent environments.[2–11] They are ideal vibrational probes for the protein folding process because they exhibit long vibrational lifetimes and are sensitive to their local environments.[2,3,6–12] Using 2D IR spectroscopy, the local solvation environment around the pseudo-halide probe can be determined through monitoring the relaxation rate of the XCN stretch, where X = O, S, or Se.[2,5,6,9–14] However, research on pseudo-halide anions has been limited to their vibrational response in pure solvent environments. Investigating the vibrational response of the probe in a full range of mixed solvent conditions, even mixtures containing only two components, is an arduous task if standard 2D IR spectroscopy methods are used. For example, if five mixed solvent conditions are produced and the study includes the pure solvents for a total of seven solvent conditions to be explored, an investigator will need to prepare seven

sample solutions and collect upwards of 100 fully averaged 2D IR spectra or more if the investigator seeks to characterize the vibrational lifetime and reorientational dynamics of the probe in each solvent condition. The sample preparation time can be significantly reduced if experiments can be performed on-chip; as such the investigator would only be limited by the repetition rate of their spectrometer.

Microfluidic technology provides a platform for high-throughput spectroscopy experiments.[15–17] However, microfluidic devices have never been interfaced with 2D IR spectroscopy techniques. In part, this is due to the limited availability of IR compatible microfluidic devices. Nevertheless, the combination of 2D IR spectroscopy and microfluidic technology will allow access to the quantitative information available from 2D IR spectroscopy, regarding solvent dynamics, chemical exchange kinetics[18,19], and molecular structures[20,21] observed in chemical environments easily accessible through the precision sample control offered by microfluidic device technology. In this work we present the first demonstration of merging microfluidic device technology with 2D IR spectroscopy. More specifically, our IR compatible microfluidic devices are interfaced with a high repetition rate 2D IR spectrometer, thus producing a high-throughput 2D IR spectroscopy platform. In doing so, the complex nature of solvation surrounding the pseudo-halide vibrational probe, cyanate, is revealed.

4.2 Results and Discussion

The pseudo-halide anion, cyanate, is a solvatochromic anion which has an absorption highly sensitive to both the solvent and counter ion present in the system. The central frequency of the pseudo halide probe is particularly sensitive to the hydrogen bonding and polarity of the

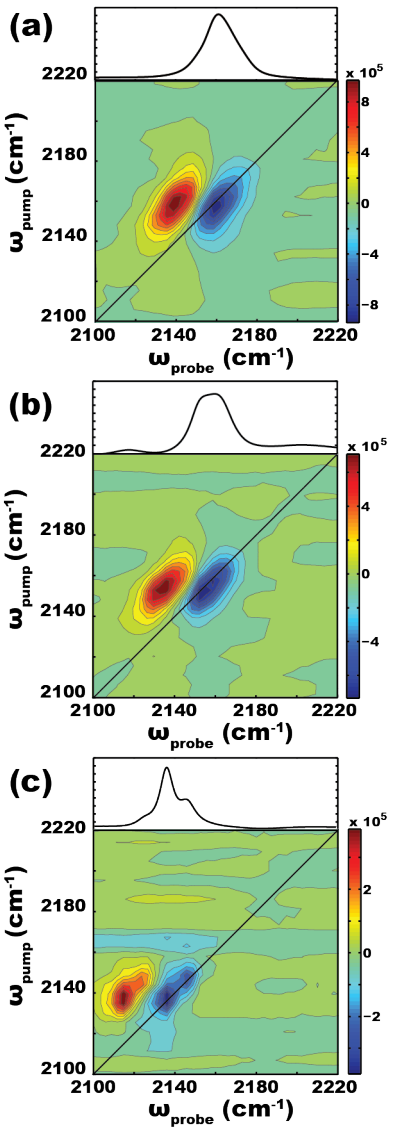

Figure 4.1 2D IR Spectra of KOCN Compared

The 2D IR spectra of (a) 50 mM KOCN in methanol (OD = 0.56), (b) 50 mM KOCN in a 50%methanol/50% DMF mixture (v/v%), and (c) 50 mM KOCN in DMF (OD = 0.10).

solvent.[2,6,8] For example, linear IR spectroscopy measurements of potassium cyanate (KOCN) in the protic solvent, methanol, yield a single peak centered at 2166 cm^{-1}, Figure 4.1a. Whereas in the aprotic solvent dimethyl formamide (DMF), two features are present as a main peak with a shoulder at the center frequencies of 2136 cm^{-1} and 2146 cm^{-1}, respectively, Figure 4.1c. In

DMF, the main peak is associated with the unbound cyanate ion, while the shoulder is associated with the contact ion pair of the cyanate anion with the potassium cation.[7] The central frequency of the unbound cyanate peak in DMF is at a lower frequency than in methanol due to the decrease in polarity of methanol and increase in hydrogen bonding environment associated with methanol as compared with DMF. The sensitivity of the cyanate absorption features to changes in solvent environment make cyanate a useful vibrational probe to report on the local solvent environment in more complex systems, such as the protein solvation shell.[2,3] However, the interpretation of the vibrational response of these vibrational probes may not be entirely straightforward. For example, in a 50% DMF/50% methanol (v/v%) solvent mixture the vibrational response of cyanate yields a spectrum that is not simply the result of the addition of the two pure solvent environments, Figure 4.1b. Using 2D IR spectroscopy to observe this phenomenon, it is possible to characterize the cyanate vibrational response associated with specific mixed solvent environments.

The local environments surrounding proteins are highly variable and in order to use pseudo-halide vibrational probes to report on these heterogeneous solvation environments it is necessary to perform studies observing the pseudo-halide vibrational probes themselves in mixed solvent environments. The vibrational response of cyanate to their local solvent environments were measured in a high-throughput manner by incorporating microfluidic devices specifically designed to generate a tunable solvent gradient into the sample platform of a 100 kHz 2D IR spectrometer. The microfluidic device was used to generate a stable, tunable solvent gradient of methanol to DMF laterally across the channel. The specific geometry, shown in Figure 4.2a, exploits a serpentine pattern in which the channels are 300 μm wide and 49 μm tall to generate secondary flows, thus enhancing the diffusive mixing process.[15] The channel then straightens

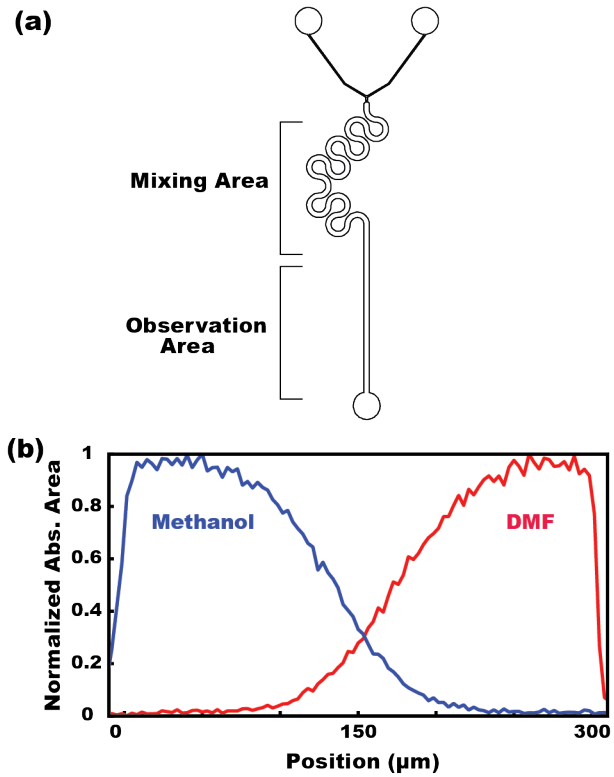

Figure 4.2 Gradient Generation in Microfluidic Device

(a) The photomask used to create the IR transparent microfluidic devices for gradient generation. (b) The solvent profile used in this work measured within the observation area.

into an observation area, where the gradient is maintained. Within the observation area, the tunable gradient of the two incoming fluids can be spatially sampled across the channel; the gradient produced across the device in the observation area is shown in Figure 4.2b. The tunability of the solvent gradient using flow rates is described in the supporting information. The percentage of methanol across the gradient was determined by integrating the IR microscopy images from 3136 to 3189 cm^{-1} for the solvent methanol and 1720 to 1728 cm^{-1} for the solvent DMF. The gradient affords multiplexed sample preparation, thus significantly reducing the time and chemical usage required to map the chemical interaction as a function of solvent environment. Given the flow rates of 6.0 μL/min in this work, a 1.0 mL sample will yield 2.8

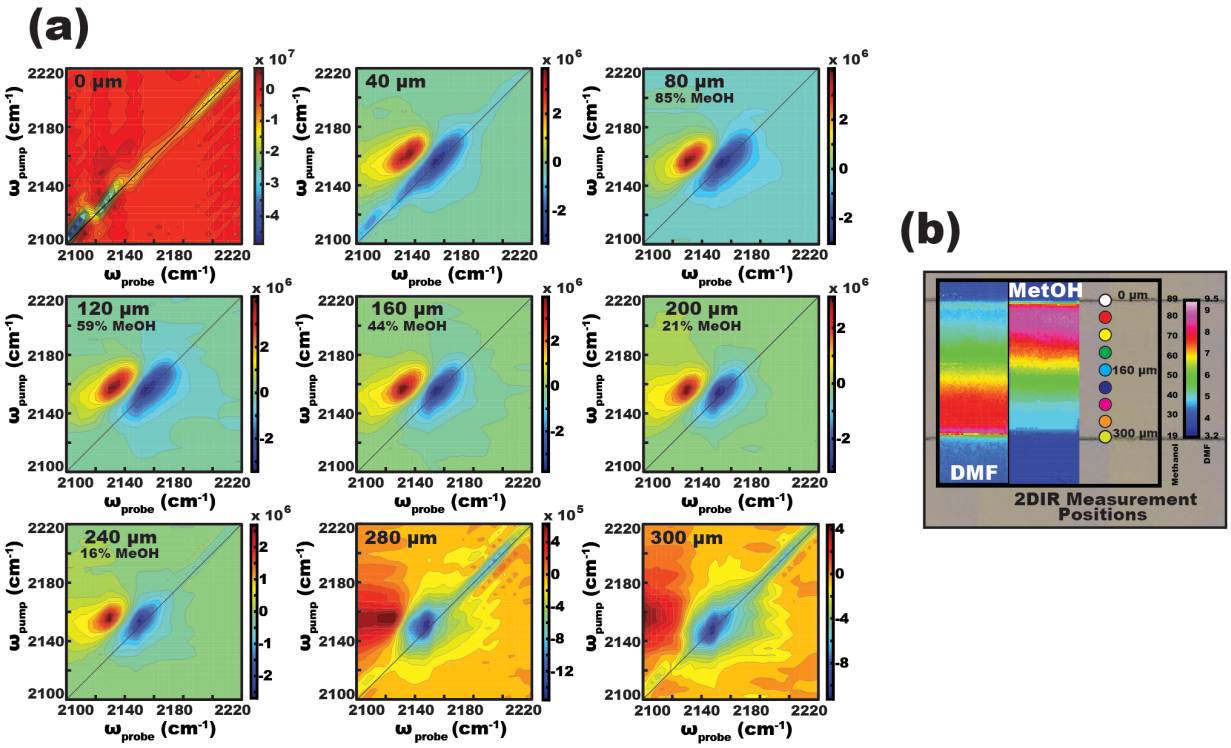

Figure 4.3 2D IR Spectra Collected in a Device

(a) The 2D IR spectra collected across the microfluidic channel moving from 100% methanol to 100% DMF by volume. (b) The IR chemical map images integrated from 3136 to 3189 cm^{-1} for the solvent methanol and 1720 to 1728 cm^{-1} for the solvent DMF. The dots indicate the locations of 2D IR measurements across the channel.

hours of spectrometer time under continuous flow conditions. The observed 2D IR spectra are depicted in Figure 4.3a. At the edge of the channel scatter is present in the spectrum and thus the position of the measurement is confirmed. Moving in 40 μm steps across the channel, changes are observed as the methanol composition by volume changes: 85%, 59%, 44%, 21%, and 16% methanol at 80 μm, 120 μm, 160 μm, 200 μm, and 240 μm, respectively. There is significant distortion in the 2D IR spectra from scatter at the positions, x = 0, 40, 280, and 300 μm, therefore these spectra are not included in the analysis of the vibrational response of cyanate in methanol:DMF mixed solvent conditions. At the other positions, the 2D IR spectra collected on-chip are comparable to spectra collected in a standard CaF_2 sample cell. The full series of 2D IR

spectra collected in a standard sample cell are included in the supplemental material associated with this work. In Figure 4.4b and 4.4c, 2D IR spectra collected in a standard sample cell are compared directly to spectra collected on-chip. In order to produce 2D IR spectra on-chip that are scatter-free, irises were placed to spatially filter scatter that was not fully removed by utilizing a rotating frame in the pulse-shaper.

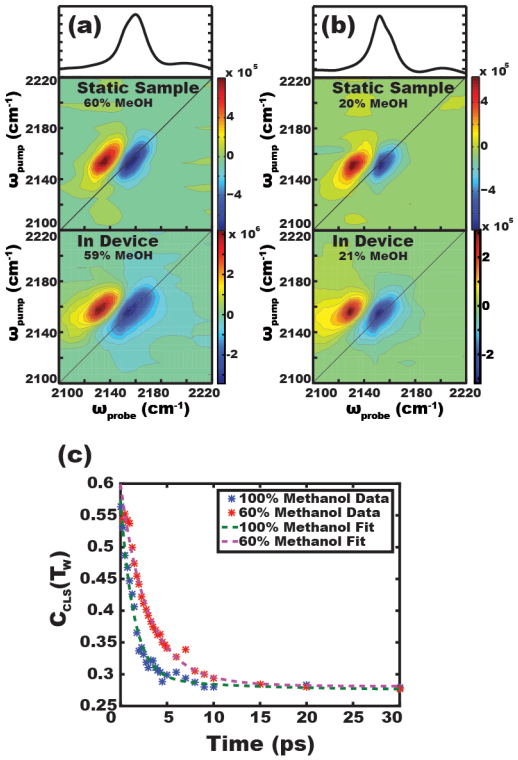

Figure 4.4 Dynamics Obtained on Chip

The comparison of 2D IR spectra collected in a static sample and on-chip with a) 60% and 59% methanol, respectively, and b) 20% and 21% methanol, respectively. (c) The inverse center line slopes, CLS, plotted as a function of T_w, for the potassium cyanate in 100% methanol (blue) compared with the 60% methanol/40% DMF mixture (red) obtained on-chip. The experimental data appear as the individual points on the plot and the dashed line is the biexponential fit of the data.

The vibrational response of cyanate to different solvent mixtures can be characterized by resolving the 2D IR spectra spatially across the microfluidic devices. For example,

anharmonicity of the cyanate can be extracted from the 2D IR spectra collected. The measured anharmonicity associated with different solvent mixtures are given in Table 4.1. The change in anharmonicity of the cyanate probe in mixed solvent environments are minimal and are comparable to the anharmonicities measured previously.[7] These results indicate there is not a significant variability in the curvature of the potential energy surface of cyanate in these mixed solvent conditions. However, comparing the peak positions from linear IR spectra across a range of methanol:DMF mixtures shows a clear difference in the vibrational response of the cyanate ion.

Table 4.1 Anharmonicity Across Device

Percent Methanol	*Anharmonicity (cm^{-1})*
85%	24.4
59%	24.3
44%	24.2
21%	23.5
16%	22.2

The linear IR spectra of 50 mM KOCN as a function of methanol concentration (v/v%), with 100% methanol, 80% methanol, 60% methanol, 40% methanol, 20% methanol, and 0% methanol, respectively were measured and are provided in the supplemental information where

they are compared to the weighted summation of the two pure solvent environments. In the case of two distinct solvent environments being present, the observed spectra could be deconvolved into a simple sum of contributions from the spectra observed when the cyanate probe is in pure methanol or pure DMF. However, it is observed in the measured FTIR that the addition of methanol perturbs the two DMF peaks in a way that the experimental spectra cannot be reproduced by weighted sums. These results suggest the cyanate probe are not merely existing in methanol-like or DMF-like environments. Instead, the spectra observed in this work indicate the presence of a local solvent environment that has different attributes from the pure methanol or pure DMF solvent environments. The solvent dynamics surrounding the cyanate vibrational probes can be compared using the experimentally extracted centerline slope data. In Figure 4.4c, the inverse of the centerline slope values are plotted as a function of T_w for the 60% methanol/40% DMF solvent mixture and the 100% methanol solvent condition. The extracted inverse of the center line slope points, are fit to a biexponential function,

$$C_{CLS}(T_W) = a_1 exp(-T_W/\tau_1) + a_2 exp(-T_W/\tau_2) \qquad (4.1)$$

This biexponential fit of the 100% methanol solvent condition gives an a_1 of 0.529, $\tau_1$of 1.41 ps, a_2 of 0.144, and $\tau_2$of 11.84 ps, while the biexponential fit of the 60/40 methanol DMF mixture gives an a_1 of 0.503, $\tau_1$of 2.64 ps, a_2 of 0.255, and $\tau_2$of 11.84 ps. These results indicate that the mixed methanol and DMF environment has a slightly slower vibrational relaxation than a pure methanol enviornment. The nature of the local solvent environments reported by the vibrational response of the cyanate probe and the details giving rise to these vibrational dynamics are the subject of ongoing investigations and will be addressed in future 2D IR spectroscopy experiments.

4.3 Conclusion

In summary, we have for the first time, demonstrated high throughput 2D IR data acquisition that can be accomplished by integrating IR compatible microfluidic device technology with a high repetition rate 2D IR spectrometer[13]. To be clear, the microfluidic devices employed in this work can easily be interfaced with a 1 to few kHz 2D IR spectrometer. However, it is the combination of using microfluidic technology with a 100 kHz spectrometer that creates a true high throughput 2D IR platform. For reference, in addition to the data presented in this work, we used this platform to perform a series of T-waiting experiments consisting of 320 time steps in $T_{waiting}$, for the five mixed solvent conditions presented in this work; the complete series is comprised of a data set of 1600 fully averaged 2D IR spectra collected with 100 nJ pulse energies, 358 time delays in τ, and a four-frame phase cycling scheme with a rotating frame. Under these conditions the complete data set was acquired in 125 minutes; thus producing an acquisition rate just over 12 fully averaged spectra per minute. The accessibility of these acquisition rates in the multidimensional IR community will extend the scope of possible experiments in multidimensional IR spectroscopy and microscopy applications[22,23]. In these experiments, the sensitivity of the cyanate vibrational response in mixed solvent environments was efficiently mapped. The results revealed the complex nature of the methanol:DMF solvent environments. It is clear from this work that the vibrational response of cyanate vibrational probe is sensitive to the details of the local solvent structure surrounding the cyanate anion.

4.4 Experimental Methods

The fabrication of the PDMS IR compatible microfluidic device used has been described previously.[24] Briefly, the devices were fabricated using a standard photolithography technique in polydimethyl siloxane (PDMS, Sylgard 184, Dow Corning). Each of the IR compatible microfluidic chips is comprised of four components: a support layer, microchannel layer, adhesion layer, and calcium fluoride backbone. To create the complete microfluidic device, all four components are individually prepared and then assembled by sealing the PDMS with an air plasma. Two NE-500 Programmable OEM syringe pumps are used to pump fluid, in 10 mL syringes, into the microfluidic devices. The flow rates used for this experiment were 6.0 μL/min for both streams entering the device.

A Bruker Hyperion 3000 FTIR microscope was used to take the infrared microscope images. The FTIR microscope utilizes a 64 x 64 element FPA detector and a 15x objective to give a 7.6 μm^2 spatial resolution. All FTIR microscope images were taken in transmission mode, and were processed using OPUS software (Bruker Optics).

The 2D IR spectroscopy was performed with a 100 kHz 2D IR spectrometer, which has been described in previous work.[13] The setup can be seen in the supporting information. Briefly, this spectrometer is based on optical parametric chirped-pulse amplification (OPCPA) in magnesium doped periodically poled lithium niobate (MgO:PPLN) and difference frequency generation (DFG) in zinc germanium diphosphide (ZGP). Both the pump and seed beams for the OPCPA stages are generated in an All Normal Dispersion (ANDi)[25] Ytterbium-Fiber (Y-Fi) mode locked oscillator source. Most of the Y-Fi output is separated and compressed to pump an optical parametric oscillator (OPO) generating 170 fs pulses centered at 1.68 μm light. This is the seed for the OPCPA stages. The remaining uncompressed output centered at 1 μm is amplified in the

cryogenically cooled Yb:YAG based regenerative amplifier and the two pass Yb:YAG based amplifier. This is the pump for the OPCPA stages. Three stages of OPCPA amplification in MgO:PPLN crystals are utilized to amplify the stretched 1.68 μm and generate a 2.67 μm idler. The signal and idler are compressed in a transmission grating compressor and a material silicon compressor, respectively. This signal and idler are recombined in a ZGP DFG stage, which generates 3 μJ of 4.65 μm mid-IR output with 220 fs pulse durations. A long pass filter is used to separate and collimate this mid-IR light to be sent to the 2D IR spectrometer. This output is split into two lines, one of which is sent to a high speed, mid-IR pulse shaper to generate the pump pulse pair with a variable delay at 100 kHz.[26] The second line is used as the probe pulse. The pump and probe pulses are focused on the sample cell to a spot size of 130 μm FWHM using a four inch focal length 90° off axis parabolic mirror. The probe beam is then collected on a 1 x 64 element, mercury cadmium telluride (MCT) mid-IR spectrometer operating at 100 kHz. The 2D spectra are all collected using a series of 358 pump pulse pairs delayed from 0 to 2.5 ps in 7 fs steps. In order to reduce scatter, a four-step phase cycling scheme with 2000 cm^{-1} rotating frame collection was used in combination with an iris to spatially filter scatter remaining in the probe line.

The two sample solutions utilized in both the static and microfluidic device experiments were 50 mM KOCN in HPLC grade N,N-Dimethylformamide (DMF) and 50 mM KOCN in ACS grade methanol; the optical densities of the samples were 0.1 and 0.56 for 50 mM KOCN in DMF and methanol, respectively. The KOCN, DMF, and methanol were all used without further purification and were purchased from Sigma Aldrich. All experiments were performed at room temperature. The FTIR and static 2D IR experiments were performed by placing the sample between two CaF_2 plates using a 50-μm-thick Teflon spacer. Experiments performed in the

microfluidic device were accomplished by flowing the KOCN in DMF and methanol through the 49-μm tall channel, and centering on the channel was accomplished by 3D mapping both pump and probe scatter off the channel edges. The device was translated using a 3-axis translational stage to sample different locations in the channel.

4.5 Additional Notes

This research was supported by BP Exploration Operating Company Ltd. and the National Science Foundation (Grant No. CHE-1255658).

References

(1) Tracy, K. M.; Barich, M. V.; Carver, C. L.; Luther, B. M.; Krummel, A. T. High-Throughput Two-Dimensional Infrared (2D IR) Spectroscopy Achieved by Interfacing Microfluidic Technology with a High Repetition Rate 2D IR Spectrometer. *J. Phys. Chem. Lett.* **2016**, *7* (23), 4865–4870.

(2) Wilderen, L. J. G. W. van; Kern-Michler, D.; Müller-Werkmeister, H. M.; Bredenbeck, J. Vibrational Dynamics and Solvatochromism of the Label SCN in Various Solvents and Hemoglobin by Time Dependent IR and 2D-IR Spectroscopy. *Phys. Chem. Chem. Phys.* **2014**, *16* (36), 19643–19653.

(3) Park, S.; Park, J.; Lin, H.-W.; Lim, M. Vibrational Relaxation of Cyanate or Thiocyanate Bound to Ferric Heme Proteins Studied by Femtosecond Infrared Spectroscopy†. *Bull. Korean Chem. Soc.* **2014**, *35* (3), 758–764.

(4) Tucker, M. J.; Kim, Y. S.; Hochstrasser, R. M. 2D IR Photon Echo Study of the Anharmonic Coupling in the OCN Region of Phenyl Cyanate. *Chem. Phys. Lett.* **2009**, *470* (1-3), 80–84.

(5) Park, S.; Ji, M.; Gaffney, K. J. Ligand Exchange Dynamics in Aqueous Solution Studied with 2DIR Spectroscopy. *J. Phys. Chem. B* **2010**, *114* (19), 6693–6702.

(6) Sun, Z.; Zhang, W.; Ji, M.; Hartsock, R.; Gaffney, K. J. Contact Ion Pair Formation Between Hard Acids and Soft Bases in Aqueous Solutions Observed with 2DIR Spectroscopy. *J. Phys. Chem. B* **2013**.

(7) Son, H.; Jin, H.; Choi, S. R.; Jung, H. W.; Park, S. Infrared Probing of Equilibrium and Dynamics of Metal–Selenocyanate Ion Pairs in N,N-Dimethylformamide Solutions. *J.*

Phys. Chem. B **2012**, *116* (30), 9152–9159.

(8) Lenchenkov, V.; She, C.; Lian, T. Vibrational Relaxation of CN Stretch of Pseudo-Halide Anions (OCN-, SCN-, and SeCN-) in Polar Solvents†. *J. Phys. Chem. B* **2006**, *110* (40), 19990–19997.

(9) Park, K.-H.; Choi, S. R.; Choi, J.-H.; Park, S.; Cho, M. Real-Time Probing of Ion Pairing Dynamics with 2DIR Spectroscopy. *ChemPhysChem* **2010**, *11* (17), 3632–3637.

(10) Yuan, R.; Yan, C.; Tamimi, A.; Fayer, M. D. Molecular Anion Hydrogen Bonding Dynamics in Aqueous Solution. *J. Phys. Chem. B* **2015**, *119* (42), 13407–13415.

(11) Sun, Z.; Zhang, W.; Ji, M.; Hartsock, R.; Gaffney, K. J. Aqueous Mg2+ and Ca2+ Ligand Exchange Mechanisms Identified with 2DIR Spectroscopy. *J. Phys. Chem. B* **2013**, *117* (40), 12268–12275.

(12) Levin, D. E.; Schmitz, A. J.; Hines, S. M.; Hines, K. J.; Tucker, M. J.; Brewer, S. H.; Fenlon, E. E. Synthesis and Evaluation of the Sensitivity and Vibrational Lifetimes of Thiocyanate and Selenocyanate Infrared Reporters. *RSC Adv.* **2016**, *43* (6), 36231–36237.

(13) Luther, B. M.; Tracy, K. M.; Gerrity, M.; Brown, S.; Krummel, A. T. 2D IR Spectroscopy at 100 kHz Utilizing a Mid-IR OPCPA Laser Source. *Opt. Express* **2016**, *24* (4), 4117–4127.

(14) Rodgers, J. M.; Zhang, W.; Bazewicz, C. G.; Chen, J.; Brewer, S. H.; Gai, F. Kinetic Isotope Effect Provides Insight into the Vibrational Relaxation Mechanism of Aromatic Molecules: Application to Cyano-phenylalanine. *J. Phys. Chem. Lett.* **2016**, *7* (7), 1281–1287.

(15) Barich, M. V.; O'Connell, K.; Carver, C. L.; Krummel, A. T. Infrared Compatible

Microfluidics Tailored Towards Monitoring Chemical Interactions and Kinetics with Vibrational Spectroscopy. *J. Phys. Chem. B* **2016**.

(16) Dertinger, S. K. W.; Chiu, D. T.; Jeon, N. L.; Whitesides, G. M. Generation of Gradients Having Complex Shapes Using Microfluidic Networks. *Anal. Chem.* **2001**, *73* (6), 1240–1246.

(17) Mao, H.; Yang, T.; Cremer, P. S. A Microfluidic Device with a Linear Temperature Gradient for Parallel and Combinatorial Measurements. *J. Am. Chem. Soc.* **2002**, *124* (16), 4432–4435.

(18) Fayer, M. D. Dynamics of Liquids, Molecules, and Proteins Measured with Ultrafast 2D IR Vibrational Echo Chemical Exchange Spectroscopy. *Annu. Rev. Phys. Chem.* **2009**, *60* (1), 21–38.

(19) Kim, Y. S.; Hochstrasser, R. M. Chemical Exchange 2D IR of Hydrogen-bond Making and Breaking. *Proc. Natl. Acad. Sci.* **2005**, *102* (32), 11185–11190.

(20) Zanni, M. T.; Hochstrasser, R. M. Two-dimensional Infrared Spectroscopy: a Promising New Method for the Time Resolution of Structures. *Curr. Opin. Struct. Biol.* **2001**, *11* (5), 516–522.

(21) Woutersen, S.; Hamm, P. Nonlinear Two-dimensional Vibrational Spectroscopy of Peptides. *J. Phys. Condens. Matter* **2002**, *14* (39), R1035.

(22) Baiz, C. R.; Schach, D.; Tokmakoff, A. Ultrafast 2D IR Microscopy. *Opt. Express* **2014**, *22* (15), 18724–18735.

(23) Ostrander, J. S.; Serrano, A. L.; Ghosh, A.; Zanni, M. T. Spatially Resolved Two-Dimensional Infrared Spectroscopy via Wide-Field Microscopy. *ACS Photonics* **2016**, *3* (7), 1315–1323.

(24) Barich, M. V.; Krummel, A. T. Polymeric Infrared Compatible Microfluidic Devices for Spectrochemical Analysis. *Anal. Chem.* **2013**, *85* (21), 10000–10003.

(25) Chong, A.; Buckley, J.; Renninger, W.; Wise, F. All-normal-dispersion Femtosecond Fiber Laser. *Opt. Express* **2006**, *14* (21), 10095–10100.

(26) Shim, S.-H.; Zanni, M. T. How to Turn Your Pump–probe Instrument into a Multidimensional Spectrometer: 2D IR and Vis Spectroscopiesvia Pulse Shaping. *Phys. Chem. Chem. Phys.* **2009**, *11* (5), 748–761.

Chapter 5

Visualizing Chemical Dynamics in an Ionic Liquid Microdroplet using Ultrafast 2D IR Microscopy

This chapter is based on a manuscript from 2018, which has been submitted to the Journal of Physical Chemistry Letters, focusing on work performed in cooperation with Dr. Biswajit Guchhait. For this work, I built and characterized the 2D IR microscope set up and developed the LabView code that interfaced the stages and visible camera with the code used to collect 2D IR spectroscopy data. The process of collecting and analyzing the 2D IR microscopy data was accomplished through joint effort between Biswajit and myself.

5.1 Introduction

Recently, investigators have turned to nonlinear optical spectroscopy techniques including sum frequency generation spectroscopy[1] and two-dimensional infrared (2D IR) spectroscopy[2–7] to characterize RTILs at interfaces and measure the dynamics that occur in bulk RTIL environments, respectively. In order to advance the utility of RTILs in microdroplet chemistry, the length scales over which various dynamical behaviors exist are important.[4,8–12] In this work, we characterize ultrafast structural dynamics of a RTIL microdroplet using 2D IR microscopy with a high acquisition rate. Microdroplet chemistry is an emerging field and the present 2D IR imaging studies of a RTIL microdroplet illuminate details of dynamics and long range effects, which pave the way for a more detailed exploration of this new field.

Recent efforts have focused on spatially resolving molecular structure and dynamics of heterogeneous samples. Important experiments demonstrating the feasibility of ultrafast 2D IR

microscopy have been performed;[13,14] however, a major impediment to extensive practical implementation of 2D IR microscopy is the long acquisition time. Recently we demonstrated high throughput 2D IR spectroscopy utilizing a mid-IR optical parametric chirp pulse amplifier (OPCPA) laser system operating at a 100 kHz repetition rate.[15,16] In order to study the structural dynamics in a microdroplet, we perform 2D IR microscopy utilizing our Yb-based, 100 kHz mid-IR OPCPA laser source. Taking advantage of the high repetition rate and improved signal-to-noise ratios over Ti:sapphire laser sources, 2D IR microscopy experiments are carried out with much faster acquisition rates. Here we have studied a microdroplet formed with the RTIL, 1-ethyl-3-methylimidazolium tetrafluoroborate ($EmimBF_4$). Spatially resolving the time-dependent 2D IR signals reveals distinctly different dynamic behavior, including differences in homogeneous and inhomogeneous contributions to the spectral line shape at the bulk and interface of the RTIL microdroplet. In addition, intermediate regions between the interface and bulk regions are investigated.

5.2 Results and Discussion

The microdroplets consisted of 1-ethyl-3-methylimidazolium tetrafluoroborate ($EmimBF_4$) and 1-ethyl-3-methylimidazolium tricyanomethanide (EmimTCM) RTILs and are formed by casting 10-20 nL of the RTIL mixture into dimethyl silicon oil. The EmimTCM is doped into the EmimBF4 in a 1:500 volume ratio where TCM^- acts as a vibrational probe. The oil is used for stabilization of the RTIL microdroplet as well as removing scatter from the interface because the refractive index of the silicon oil is similar to the RTIL microdroplet. Further details of the sample preparation are provided in the supplemental information. The tricyanomethanide

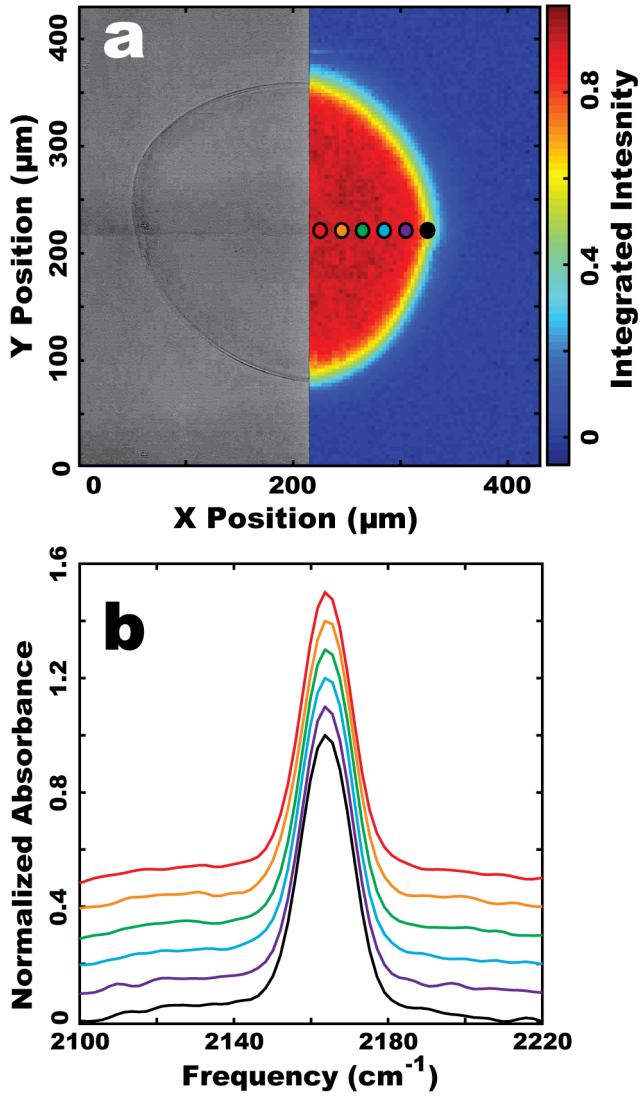

Figure 5.1 FTIR Microscopy of RTIL Microdroplet

(a) Bright-field and FTIR microscopy image of the RTIL microdroplet. The intensity values on the chemical map are generated by integrating the FTIR spectra of each point from 2146 cm^{-1} to 2186 cm^{-1}. (b) Comparison of FTIR spectra extracted for the set of points across the droplet, indicated in the chemical map above. The FTIR spectra are offset for ease of viewing.

(TCM^-), a trigonal planar anion, is evenly dispersed within the microdroplet and used as a molecular probe for all of these experiments. In order to probe the vibrational response of TCM^- in a microdroplet, a FTIR microscope image of an Emim-BF_4/Emim-TCM RTIL microdroplet in silicone oil was collected and is shown in Figure 5.1. The FTIR spectra were compared at

different locations across the droplet, indicated by the points denoted in Figure 5.1a; the spectra corresponding to each point are plotted in Figure 5.1b. The linear IR spectra of TCM^- exhibits an absorption band in the 2100-2200 cm^{-1} region with a peak appearing at 2164 cm^{-1} corresponding to the degenerate asymmetric stretching vibrations of TCM^-. It can be seen in the chemical map generated from FTIR microscopy that the TCM^- is homogenously distributed throughout the droplet, as there are no fluctuations of the intensity of the peak associated with the TCM^- throughout the microdroplet. The FTIR spectra at each point have the same FWHM linewidth of 15.5 ± 0.04 cm^{-1} and center frequency of 2164.0 ± 0.07 cm^{-1}. Thus, any underlying solute-solvent interactions in the RTIL microdroplet remain hidden in FTIR microscopy. However, utilizing 2D IR microscopy, such interactions can be extracted by studying the chemical dynamics across the microdroplet.

In order to quantify the dynamics across the RTIL microdroplet, 2D IR microscopy was performed. The 2D IR microscope is fully detailed in the supplemental information. Briefly, the 2D IR spectra were collected in a collinear geometry under the <XXYY> polarization condition, and detected on a 1x64 element MCT detector operating at the speed limit of detection of 100 kHz. The spectra used to produce the 2D IR images were collected in a point scanning fashion. The full width at half maximum (FWHM) beam diameter was measured to be 19.5 μm in the Y direction and 14.2 μm in the X direction. The Rayleigh range of focus in the direction of propagation is approximately 140 μm. Considering the physical dimensions of the monochromator, MCT element dimensions, and the gratings, the resolution along the probe axis (ω_{probe}) of the 2D IR spectra collected is 3.3 cm^{-1}. The 2D IR spectra were all collected using a series of 510 pump pulse pairs delayed from 0 to 3.57 ps in 7 fs steps. Thus, the spectral

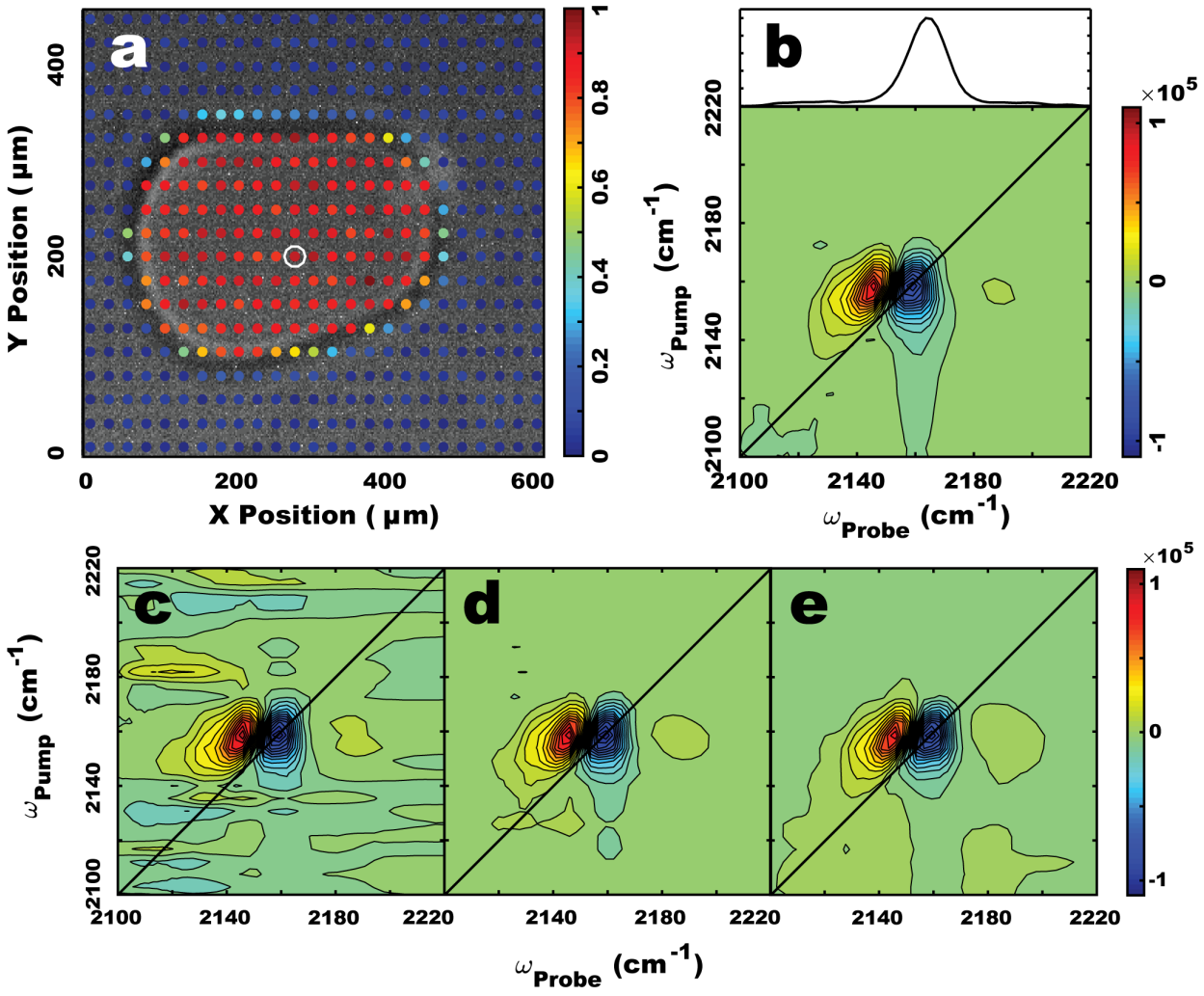

Figure 5.2 2D IR Microscopy Image

A point-scanning 2D IR microscopy image (a) with a 2D IR spectrum (b) representative of the bulk environment at the position of the white circle in (a). The intensity of points in the 2D IR image are determined by integrating the peak associated with the v=1→2 transition in the corresponding 2D IR spectrum. Comparison of data acquired under different collection schemes (c) a single 2D IR spectrum with no averaging, (d) a 2D IR spectrum generated by averaging 25 spectra, and (e) a 2D IR spectrum generated by averaging 250 spectra.

resolution along the pump-axis (ω_{pump}) is 4.7 cm^{-1}. Spectra were acquired using a four-step phase cycling scheme with 2000 cm^{-1} rotating frame for background and scatter removal. The full 2D IR microscopy image of the RTIL microdroplet, shown in Figure 2a, is comprised of a data set of 476 2D IR spectra fully averaged 500 times. 2D IR spectra were collected at 25 μm intervals along the X and Y axes (laboratory frame) at a waiting time (T_w) equal to 250 fs, by scanning the sample stage with a nanopositioner. In Figure 5.2a, the bright field image of the RTIL microdroplet is shown, where the points overlaid with the image indicate the spatial positions of the collected 2D IR spectra. The bright field image of the sample was collected using a visible beam splitter and a 2x imaging lens to project the image onto a visible camera. We correlated the position of the bright field image with the position at which the 2D IR spectra are collected by maximizing the IR throughput of the probe and pump beams through a pinhole at the focal plane. We then imaged the pinhole onto the visible camera and utilized the pinhole location as the location of our 2D IR collection. Figure 5.2b presents a 2D IR spectrum representative of the bulk environment position, indicated by the white circle in Figure 5.2a. The blue contours represent signals generated by v=0→1 transitions, while the yellow-red contours arise from v=1→2 transitions. The v=1→2 band is red shifted due to the vibrational anharmonicity of the asymmetric stretching vibrations of the TCM^-. The intensity of points in the 2D IR image are determined by integrating the peak associated with the v=1→2 transition in the 2D IR spectrum collected at each point. In this image the spectra collected were each an average of 500 2D IR spectra at a spectral acquisition rate of 1984 individual spectra per minute. A comparison was performed for data acquired under different averaging conditions at the position representative of the bulk environment. When comparing a single 2D IR spectrum, a spectrum generated by averaging 25 spectra, and 250 spectra as seen in Figure 5.2 (c-e), it can be seen that even with no

averaging the signal can be observed and the noise floor in the data does not overwhelm the spectral shape. Therefore, in future experiments one may choose to utilize different averaging schemes and use the 1984 spectra per minute acquisition rate to best suit the purpose of the experiment. The use of a Yb-based, 100 kHz laser system also allowed us to utilize pulse energies of 70 nJ/pulse, which were much lower than those typically used for 2D IR spectroscopy performed with Ti:sapphire systems at lower repetition rates. These signal-to-noise ratios and lower pulse intensities are a result of the use of a Yb laser source for the 100 kHz system instead of the Ti:sapphire systems typically used for 2D IR. It has been recently demonstrated that Ti:sapphire systems exhibit higher noise at all frequencies and has a significantly shorter shot to shot correlation time than Yb based gain media. The high time resolution inherent in 2D IR spectroscopy allows one to examine the response of a vibrational probe to its solvation environment and directly measure the time scales of motion related to the solvent molecules.[17–22] Using both the time and spatial resolution of 2D IR microscopy, dynamics information of different solvation regions across the microdroplet can be examined. In these experiments, the time delay (T_w) between the second and third pulses is varied and the solvent environment is allowed to evolve after pumping the system. A 2D IR microscopy experiment aimed at extracting the vibrational dynamics of the TCM^- probe was performed over a region of interest of the RTIL microdroplet, where at each point 2D IR data were collected as a function of increasing T_w. It can be observed that the diagonal elongation decreases and the 2D spectra become gradually spherical due to spectral diffusion as T_w increases.

We performed nodal line slope analysis[20–24] of the collected 2D IR spectra to characterize the spectral diffusion dynamics of TCM^- in an RTIL microdroplet. Spectral diffusion dynamics present some parameters, such as correlation times and the fluctuation amplitudes of the

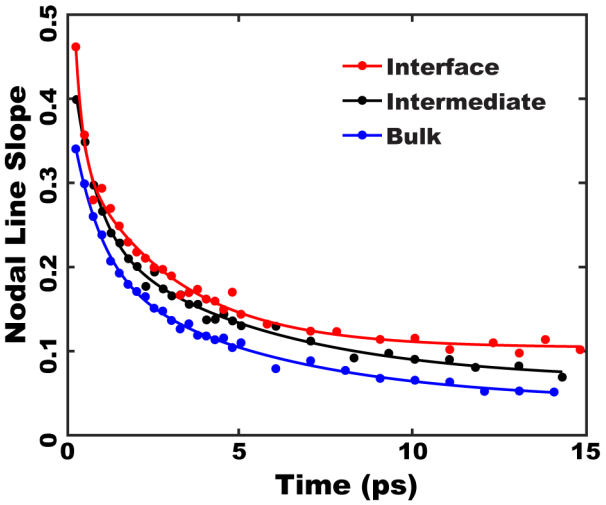

Figure 5.3 Comparison of the Dynamics in Different Environments in a RTIL Microdroplet

Comparison of slope decay data extracted for spatial points representative of the bulk environment, the interfacial environment, and the chemical environment between the bulk and interfacial regions. The points are the experimentally measured values and the lines indicate the biexponential fits to the data.

frequency fluctuation correlation functions (FFCFs).[4,22,23] In Figure 5.3, the nodal line slope values are plotted as a function of T_w, thus depicting the vibrational dynamics from different regions of the microdroplet—the interface, bulk, and intermediate region between the two. The slope values decay as T_w increases. The initial values of slopes suggest that a significant amount of the motionally narrowed component contributes to the FFCF. It can be seen in Figure 5.3 that the decay curves at bulk and interfacial regions are significantly different. In addition, the decay at intermediate regions exhibit a combined behavior of the bulk and the interface. The decays were fit to a biexponential function following the model,

$$C(T_W) = a_1 exp(-T_W/\tau_1) + a_2 exp(-T_W/\tau_2) + b \qquad (5.1)$$

The biexponential fit of the bulk region gives a τ_1 of 810 ± 100 fs and a τ_2 of 5.2 ± 1 ps. In contrast, the interface region produces a $\tau_1$of 210 ± 50 fs and a τ_2 of 2.8 ± 0.25 ps. Therefore,

the time components indicate that the dynamics of spectral diffusion is markedly faster at the interface than at the bulk environments within the RTIL microdroplets. The data representative of the intermediate region was collected at a position 5 μm from the interface, inside the microdroplet. This intermediate region exhibits a combination of bulk and interfacial behaviors, producing a τ_1 of 650 ± 100 fs and a τ_2 of 5.0 ± 0.6 ps. These results suggest that the structural rearrangement of the RTIL occurs on faster time scales at the interface compared to the interior region of the microdroplet. In the bulk environment of the microdroplet, the short time constant is most likely caused by ultrafast fluctuation of the first solvation shell of the ionic polar region, and the long time constant arises as a result of longer length scale motions involving dynamics from ionic and partly from nonionic domains, in agreement with earlier alkyl chain length dependent studies of RTILs.[3,25]

The chemical dynamics observed in this investigation reveal interesting characteristics of RTILs that are in contrast to other immiscible chemical systems. For example, previous simulation studies of water-organic nonpolar liquids[26–28] and the water-air interface[29] have reported that the structural relaxation dynamics and reorientation dynamics of interfacial water molecules are slower than the bulk water molecules. Moreover, recent experimental studies of the air-water interface using time resolved SFG spectroscopy show a slowing down of the vibrational relaxation of water at the interface compared to the bulk.[30] In the present study, the dynamics of structural relaxation at the microdroplet interface is expected to be slower than the bulk, taking into consideration the contribution of the nanoscale silicone oil-RTIL interface. The silicone oil is hydrophobic, inert and immiscible with the RTIL (EmimBF4/EmimTCM), and previously it has been used in microfluidics to provide a barrier against molecular cross talk between adjacent droplets.[31,32] The static dielectric constant (ϵ_0 ~2.4) and viscosity (η ~50 cP) of

the silicone oil are significantly different from the RTIL investigated here[33], ϵ_0 ~14 and η ~28 cP, respectively. Thus, the Si-O unit of the oil may have a minor interaction with the ionic component of the RTIL; however, the contribution of such an interaction on spectral diffusion is mostly insignificant. Therefore, the structural relaxation of the microdroplet interface is remarkably different than that of the polar liquid interfaces with organic nonpolar solvents.

Spectral diffusion dynamics in RTILs have been previously studied using linear vibrational probes thiocyanate (SCN^-) and selenocyanate ($SeCN^-$); the dynamics were observed to be slower than the present experiment.[2–7,25,34] For example, the fast time components were a few ps and the long time components were a few 10s of ps. In the present study, the structure of the vibrational probe, TCM^-, is trigonal planar and the charge density of the probe is smaller than the linear anionic vibrational probes, SCN^- or $SeCN^-$, owing to the delocalization of charge over the three CN groups. It is possible the slow spectral diffusion of a linear anionic probe in RTILs arises because of the higher charge density compared to the trigonal planar TCM^- anion. In addition, because the 2D IR spectra were collected in a cross-polarization geometry in this work, the measurements are sensitive to the fast time components of the dynamics, a point that will be discussed further in future work.

It is very clear from the nodal line slope decays presented in Figure 3 that the homogeneous contribution and spectral diffusion followed by a static inhomogeneity constitute the frequency fluctuations of the asymmetric CN stretching of TCM^- in the RTIL microdroplet. The homogeneous contribution is a large motionally narrowed component, which arises from very fast fluctuations due to low frequency librations[35] in the RTIL and dominates the spectral line shape. The slope values at the initial waiting time indicate that the amount of homogeneous contribution increases from the interfacial environment to the bulk environment. Moreover, at

the interfacial region, the 2D IR spectra are more inhomogeneously broadened than the bulk at all waiting times—a result nicely reflected in the decays of the nodal line slopes. Looking at the static offset of the different regions, the bulk and the interfacial regions show an offset of ~0.05 and ~0.10, respectively. The larger static offset at the interface is an indicator of greater static inhomogeneous contributions, which exhibit very slow relaxation of the FFCF in our experimental time window. The larger inhomogeneous contribution to the frequency fluctuation appears as a result of anisotropic orientation of ions in the RTIL microdroplet, which provides faster spectral diffusion dynamics at the interface. Nevertheless, further study is required to determine the mechanistic details of spectral diffusion in the RTIL microdroplet. The observation of distinctly different dynamic behaviors, along with homogeneous and inhomogeneous contributions to the frequency fluctuations underscore the importance of solute-solvent interactions in studying dynamics across the multitude of environments present in a RTIL microdroplet. Therefore, the present results of this 2D IR microscopy investigation are of high importance to the understanding of the RTIL microdroplet chemistry.

Now we can discuss the behavior in the intermediate region of the RTIL microdroplet in the light of interactions of various length scales proposed in RTILs. RTIL structures at interfaces and in confinement have been extensively studied by experiment and simulation.[4,9–12,36–44] It has been found that the presence of the interface can influence the local charge ordering, thus changing the structural properties of RTILs. While most studies report that such interactions occur on a few nanometer length scale, there are some recent experimental observations that are in stark contrast. Recent experimental observations indicate that the interface can induce much longer ranged effects that span several 10s of nanometers to a few micrometers in length scale.[4,11,12] For example, very recent 2D IR spectroscopic studies of supported ionic liquid

membranes with pore sizes of ~300 nm showed a significant retardation of RTIL structural dynamics compared to the bulk phase.[4] Another spectroscopic experiment reported the transition of TFSI anion-based RTIL films into long-ranged ordered structures that persist over 2 μm when the films are formed by applying a slow shear.[11] In the present work, the chemical dynamics and spectral line shapes observed are a combination of bulk-like and interface-like as deep as 5 μm to the interior of the microdroplet. Although the apparent spatial resolution of our technique is not small enough to observe such phenomena, because the 2D IR signal depends on the square of the intensity, it is able to provide spatial resolution that is better than the FWHM beam diameters suggest, similar in fashion to two-photon fluorescence microscopy.[45,46] Therefore, the perturbation of the interface to the bulk environment in this system is long-ranged.

5.3 Conclusion

In summary, we have for the first time, spatially resolved ultrafast chemical dynamics existing in a RTIL microdroplet. The advances in 2D IR microscopy demonstrated in this work provide the opportunity to explore the chemical dynamics in the inherently complex environment of a RTIL microdroplet. 2D IR microscopy experiments were performed across the RTIL microdroplet and a region of interest was selected to include the bulk (interior) environment, interfacial environments, and intermediate regions between the interfacial and the bulk environments. A series of waiting time, T_w, measurements made throughout the region of interest revealed the complex nature of the chemical dynamics in RTIL microdroplets; the homogeneous and inhomogeneous contributions to the vibrational frequency fluctuations of TCM^- are used to probe the nature of the chemical dynamics present in the RTIL microdroplet. Our study determined markedly faster structural dynamics at the droplet interface in comparison

to the bulk or interior of the microdroplet. Moreover, the dynamics observed in the regions intermediate to the bulk and interfacial environments are a combination of bulk-like dynamics and interfacial-like dynamics and shed light on the long-range effects that exist in these RTIL microdroplets. The results from this first ultrafast study of microdroplet chemical dynamics are of great importance to understand the striking features of these systems and provide a basis for further investigation. Finally, this work demonstrates the potential power of 2D IR microscopy performed with fast acquisition rates for revealing chemical dynamics in complex environments that are hidden in other chemical imaging techniques.

5.4 Additional Notes

This research was supported by BP Exploration Operating Company Ltd. and the Department of Energy (Grant DE-SC0016137).

References

(1) Baldelli, S. Interfacial Structure of Room-Temperature Ionic Liquids at the Solid–Liquid Interface as Probed by Sum Frequency Generation Spectroscopy. *J. Phys. Chem. Lett.* **2013**, *4* (2), 244–252.

(2) Tamimi, A.; Fayer, M. D. Ionic Liquid Dynamics Measured with 2D IR and IR Pump–Probe Experiments on a Linear Anion and the Influence of Potassium Cations. *J. Phys. Chem. B* **2016**, *120* (26), 5842–5854.

(3) Tamimi, A.; Bailey, H. E.; Fayer, M. D. Alkyl Chain Length Dependence of the Dynamics and Structure in the Ionic Regions of Room-Temperature Ionic Liquids. *J. Phys. Chem. B* **2016**, *120* (30), 7488–7501.

(4) Shin, J. Y.; Yamada, S. A.; Fayer, M. D. Dynamics of a Room Temperature Ionic Liquid in Supported Ionic Liquid Membranes Vs the Bulk Liquid: 2D IR and Polarized IR Pump–Probe Experiments. *J. Am. Chem. Soc.* **2017**, *139* (1), 311–323.

(5) Ren, Z.; Brinzer, T.; Dutta, S.; Garrett-Roe, S. Thiocyanate as a Local Probe of Ultrafast Structure and Dynamics in Imidazolium-Based Ionic Liquids: Water-Induced Heterogeneity and Cation-Induced Ion Pairing. *J. Phys. Chem. B* **2015**, *119* (13), 4699–4712.

(6) Dutta, S.; Ren, Z.; Brinzer, T.; Garrett-Roe, S. Two-dimensional Ultrafast Vibrational Spectroscopy of Azides in Ionic Liquids Reveals Solute-specific Solvation. *Phys. Chem. Chem. Phys.* **2015**, *17* (40), 26575–26579.

(7) Ren, Z.; Ivanova, A. S.; Couchot-Vore, D.; Garrett-Roe, S. Ultrafast Structure and Dynamics in Ionic Liquids: 2D-IR Spectroscopy Probes the Molecular Origin of

Viscosity. *J. Phys. Chem. Lett.* **2014**, *5* (9), 1541–1546.

(8) K. Kashyap, H.; J. Hettige, J.; R. Annapureddy, H. V.; J. Margulis, C. SAXS Anti-peaks Reveal the Length-scales of Dual Positive–negative and Polar–apolar Ordering in Room-temperature Ionic Liquids. *Chem. Commun.* **2012**, *48* (42), 5103–5105.

(9) Amith, W. D.; Hettige, J. J.; Castner, E. W.; Margulis, C. J. Structures of Ionic Liquids Having Both Anionic and Cationic Octyl Tails: Lamellar Vacuum Interface Vs Sponge-Like Bulk Order. *J. Phys. Chem. Lett.* **2016**, *7* (19), 3785–3790.

(10) Paredes, X.; Fernández, J.; Pádua, A. A. H.; Malfreyt, P.; Malberg, F.; Kirchner, B.; Pensado, A. S. Using Molecular Simulation to Understand the Structure of [C2C1im]+–Alkylsulfate Ionic Liquids: Bulk and Liquid–Vapor Interfaces. *J. Phys. Chem. B* **2012**, *116* (48), 14159–14170.

(11) Anaredy, R. S.; Shaw, S. K. Long-Range Ordering of Ionic Liquid Fluid Films. *Langmuir* **2016**, *32* (20), 5147–5154.

(12) Jurado, L. A.; Kim, H.; Arcifa, A.; Rossi, A.; Leal, C.; Spencer, N. D.; Espinosa-Marzal, R. M. Irreversible Structural Change of a Dry Ionic Liquid Under Nanoconfinement. *Phys. Chem. Chem. Phys.* **2015**, *17* (20), 13613–13624.

(13) Baiz, C. R.; Schach, D.; Tokmakoff, A. Ultrafast 2D IR Microscopy. *Opt. Express* **2014**, *22* (15), 18724–18735.

(14) Ostrander, J. S.; Serrano, A. L.; Ghosh, A.; Zanni, M. T. Spatially Resolved Two-Dimensional Infrared Spectroscopy via Wide-Field Microscopy. *ACS Photonics* **2016**, *3* (7), 1315–1323.

(15) Luther, B. M.; Tracy, K. M.; Gerrity, M.; Brown, S.; Krummel, A. T. 2D IR Spectroscopy at 100 kHz Utilizing a Mid-IR OPCPA Laser Source. *Opt. Express* **2016**,

24 (4), 4117–4127.

(16) Tracy, K. M.; Barich, M. V.; Carver, C. L.; Luther, B. M.; Krummel, A. T. High-Throughput Two-Dimensional Infrared (2D IR) Spectroscopy Achieved by Interfacing Microfluidic Technology with a High Repetition Rate 2D IR Spectrometer. *J. Phys. Chem. Lett.* **2016**, *7* (23), 4865–4870.

(17) Zheng, J.; Kwak, K.; Chen, X.; Asbury, J. B.; Fayer, M. D. Formation and Dissociation of Intra−Intermolecular Hydrogen-Bonded Solute−Solvent Complexes: Chemical Exchange Two-Dimensional Infrared Vibrational Echo Spectroscopy. *J. Am. Chem. Soc.* **2006**, *128* (9), 2977–2987.

(18) Khalil, M.; Demirdöven, N.; Tokmakoff, A. Coherent 2D IR Spectroscopy: Molecular Structure and Dynamics in Solution. *J. Phys. Chem. A* **2003**, *107* (27), 5258–5279.

(19) Remorino, A.; Korendovych, I. V.; Wu, Y.; DeGrado, W. F.; Hochstrasser, R. M. Residue-Specific Vibrational Echoes Yield 3D Structures of a Transmembrane Helix Dimer. *Science* **2011**, *332* (6034), 1206–1209.

(20) Hamm, P.; Zanni, M. *Concepts and Methods of 2D Infrared Spectroscopy*; Cambridge University Press, 2011.

(21) Koziński, M.; Garrett-Roe, S.; Hamm, P. Vibrational Spectral Diffusion of CN− in Water. *Chem. Phys.* **2007**, *341* (1-3), 5–10.

(22) Roberts, S. T.; Loparo, J. J.; Tokmakoff, A. Characterization of Spectral Diffusion from Two-dimensional Line Shapes. *J. Chem. Phys.* **2006**, *125* (8), 084502.

(23) Kwac, K.; Cho, M. Molecular Dynamics Simulation Study of N-methylacetamide in Water. II. Two-dimensional Infrared Pump–probe Spectra. *J. Chem. Phys.* **2003**, *119* (4), 2256–2263.

(24) Kuroda, D. G.; Singh, P. K.; Hochstrasser, R. M. Differential Hydration of Tricyanomethanide Observed by Time Resolved Vibrational Spectroscopy. *J. Phys. Chem. B* **2013**, *117* (16), 4354–4364.

(25) Brinzer, T.; Garrett-Roe, S. Temperature and Chain Length Dependence of Ultrafast Vibrational Dynamics of Thiocyanate in Alkylimidazolium Ionic Liquids: A Random Walk on a Rugged Energy Landscape. *J. Chem. Phys.* **2017**, *147* (19), 194501.

(26) Chowdhary, J.; Ladanyi, B. M. Hydrogen Bond Dynamics at the Water/Hydrocarbon Interface. *J. Phys. Chem. B* **2009**, *113* (13), 4045–4053.

(27) Benjamin, I. Hydrogen Bond Dynamics at Water/Organic Liquid Interfaces. *J. Phys. Chem. B* **2005**, *109* (28), 13711–13715.

(28) Chen, M.; Lu, X.; Liu, X.; Hou, Q.; Zhu, Y.; Zhou, H. Retardation of Water Reorientation at the Oil/Water Interface. *J. Phys. Chem. C* **2015**, *119* (29), 16639–16648.

(29) Ni, Y.; Gruenbaum, S. M.; Skinner, J. L. Slow Hydrogen-bond Switching Dynamics at the Water Surface Revealed by Theoretical Two-dimensional Sum-frequency Spectroscopy. *Proc. Natl. Acad. Sci.* **2013**, *110* (6), 1992–1998.

(30) Van der Post, S. T.; Hsieh, C.-S.; Okuno, M.; Nagata, Y.; Bakker, H. J.; Bonn, M.; Hunger, J. Strong Frequency Dependence of Vibrational Relaxation in Bulk and Surface Water Reveals Sub-picosecond Structural Heterogeneity. *Nat. Commun.* **2015**, *6*, 8384.

(31) Schoeler, A. M.; Josephides, D. N.; Sajjadi, S.; Lorenz, C. D.; Mesquida, P. Charge of Water Droplets in Non-polar Oils. *J. Appl. Phys.* **2013**, *114* (14), 144903.

(32) Ohashi, T.; Kuyama, H.; Hanafusa, N.; Togawa, Y. A Simple Device Using Magnetic Transportation for Droplet-based PCR. *Biomed. Microdevices* **2007**, *9* (5), 695–702.

(33) Singh, T.; Kumar, A. Static Dielectric Constant of Room Temperature Ionic Liquids:

Internal Pressure and Cohesive Energy Density Approach. *J. Phys. Chem. B* **2008**, *112* (41), 12968–12972.

(34) Yamada, S. A.; Bailey, H. E.; Tamimi, A.; Li, C.; Fayer, M. D. Dynamics in a Room-Temperature Ionic Liquid from the Cation Perspective: 2D IR Vibrational Echo Spectroscopy. *J. Am. Chem. Soc.* **2017**, *139* (6), 2408–2420.

(35) Mou, S.; Rubano, A.; Paparo, D. Broadband Terahertz Spectroscopy of Imidazolium-Based Ionic Liquids. *J. Phys. Chem. B* **2018**.

(36) Santos, C. S.; Baldelli, S. Gas–liquid Interface of Room-temperature Ionic Liquids. *Chem. Soc. Rev.* **2010**, *39* (6), 2136–2145.

(37) Hayes, R.; Warr, G. G.; Atkin, R. Structure and Nanostructure in Ionic Liquids. *Chem. Rev.* **2015**, *115* (13), 6357–6426.

(38) Bovio, S.; Podestà, A.; Lenardi, C.; Milani, P. Evidence of Extended Solidlike Layering in [Bmim][NTf2] Ionic Liquid Thin Films at Room-Temperature. *J. Phys. Chem. B* **2009**, *113* (19), 6600–6603.

(39) Hayes, R.; Borisenko, N.; Tam, M. K.; Howlett, P. C.; Endres, F.; Atkin, R. Double Layer Structure of Ionic Liquids at the Au(111) Electrode Interface: An Atomic Force Microscopy Investigation. *J. Phys. Chem. C* **2011**, *115* (14), 6855–6863.

(40) Mezger, M.; Ocko, B. M.; Reichert, H.; Deutsch, M. Surface Layering and Melting in an Ionic Liquid Studied by Resonant Soft X-ray Reflectivity. *Proc. Natl. Acad. Sci.* **2013**, *110* (10), 3733–3737.

(41) Antelmi, D. A.; Kékicheff, P.; Richetti, P. The Confinement-Induced Sponge to Lamellar Phase Transition. *Langmuir* **1999**, *15* (22), 7774–7788.

(42) Sieffert, N.; Wipff, G. Ordering of Imidazolium-Based Ionic Liquids at the α-Quartz(001)

Surface: A Molecular Dynamics Study. *J. Phys. Chem. C* **2008**, *112* (49), 19590–19603.

(43) Atkin, R.; Warr, G. G. Structure in Confined Room-Temperature Ionic Liquids. *J. Phys. Chem. C* **2007**, *111* (13), 5162–5168.

(44) Coasne, B.; Viau, L.; Vioux, A. Loading-Controlled Stiffening in Nanoconfined Ionic Liquids. *J. Phys. Chem. Lett.* **2011**, *2* (10), 1150–1154.

(45) Denk, W.; Strickler, J. H.; Webb, W. W. Two-photon Laser Scanning Fluorescence Microscopy. *Science* **1990**, *248* (4951), 73–76.

(46) Zipfel, W. R.; Williams, R. M.; Webb, W. W. Nonlinear Magic: Multiphoton Microscopy in the Biosciences. *Nat. Biotechnol.* **2003**, *21* (11), 1369–1377.

Chapter 6

Perspective: 2D IR Microscopy: A Path to Spatially Resolved Ultrafast Chemical Dynamics

This chapter is a manuscript currently in preparation discussing 2D IR Microscopy. 2D IR Microscopy opens up a new avenue for the visualization of structure and dynamics in chemical systems, which is made experimentally feasible using high repetition mid-IR sources.

6.1 Introduction

Chemical imaging techniques have been developed in order to effectively image resolve differences in the chemical components and environments in heterogeneous samples. The combination of chemical and spatial resolution has made imaging a useful tool for exploring a range of applications from biological and biomedical engineering, to materials and nanoscience. A wide array of different techniques are currently being used for chemical imaging. Coherent anti-stokes Raman (CARS)[1,2] and stimulated Raman spectroscopy (SRS) microscopy[3], second harmonic imaging microscopy (SHIM)[4,5], sum frequency generation (SFG) imaging microscopy[6–8], and Fourier transform infrared (FTIR) microscopy[9]. These microscopy techniques are all in effect linear spectroscopies spatially resolving a single optical property of the sample. However, none of these techniques have the temporal resolution necessary to access chemical dynamics.

One example of this problem lies in vibrational experiments such as FTIR microscopy. In FTIR microscopy, a FTIR spectrum is taken at each pixel of the image and then integrated for a particular vibrational mode, and the associated absorbance is plotted as the color scale.

Differences in the structure, hydrogen bonding, and environments of the molecules in the ensemble can contribute to line shape differences in the resultant FTIR spectrum in different regions throughout the image. However, FTIR microscopy cannot quantify the dynamics to uniquely determine the differences in dynamics of these environments.

2D IR spectroscopy is a nonlinear optical spectroscopy with the ability to characterize condensed phase chemical systems. It offers information regarding structure and dynamics of chemical systems. Ultrafast vibrational dynamics can be quantified using 2D IR spectroscopy, thus producing information about chemical structure and dynamics of molecules in the condensed phase. 2D IR spectroscopy typically uses with a focal region that can range from several tens to hundreds of micrometers to sample solutions and samples. Due to this large focal spot size, spatial averaging occurs over large regions within the sample making it hard to characterize structural and dynamic changes that occur on small length scales. There have been efforts made on the side of sample development to get around this issue of spatial averaging and observe 2D IR with some spatial resolution. However, in systems where correlating dynamics to specific, small regions on a sample is important, moving to technological advances like microscopy is beneficial.

Recent efforts have been made to spatially resolve the molecular structure and dynamics of heterogeneous samples, which shows the feasibility of ultrafast 2D IR microscopy. By integrating 2D IR spectroscopy with microscopy, it is possible to spatially resolving the time-dependent 2D IR signals to reveal regions of differing chemical structure and dynamics not observable using either FTIR microscopy or 2D IR spectroscopy.[10,11]

6.2 Implementation of 2D IR Microscopy

In optical microscopy, a number of different optical geometries can be implemented, all serving a specific function. In one method the sample is translated through the focal plane of the laser in order to collect an image, which is a collection of a range of points. Wide-field microscopy is a method where the entire area of interest is illuminated at once and the subsequent image is resolved onto a camera for collection. Another method commonly used is laser scanning confocal microscopy where a single focusing point of the laser itself is rapidly translated across a sample to image a thin optical slice of a thick specimen.

In the first implementation of 2D IR microscopy[10], Tokmakoff et al. utilizes the method the sample was scanned through the focal plane at a focal size near the diffraction limit. The experimental setup for the point-scanning microscope configuration consists of utilizing the mid-IR output of a 1 kHz amplified Ti:sapphire and optical parametric chirped pulse (OPA) based system with pulses of 100 fs centered at 5 μm. The probe pulse is split off using an uncoated CaF_2 wedge and delayed on a stage controlling the delay of the probe with respect to the pump pulses. The pump pulse is sent to a germanium based acousto optic modulator (AOM) that is used to generate two sets of pulse pairs from a single pulse in order to perform data acquisition in the time-domain. The probe pulse is rotated by a 90° polarization change so that the pump pulse and probe can be re-overlapped in wire-grid polarizer that transmits the pump pulses and reflects the probe allowing them to propagate in the collinear beam geometry. This configuration allows for only one possible polarization scheme, the crossed polarization (XXYY) geometry. This beam is then sent into a mid-IR microscope (Hyperion 2000, Bruker Optics) and can operate in both transmission or reflection mode depending on the configuration of the objectives. After the objective, an analyzing polarizer is used to block the pump pulses and transmit only the signal

and probe which are collimated and dispersed and sent to a 64 pixel mercury cadmium telluride (MCT) array detector that has another analyzer polarizer in front of it to further reduce residual probe light. In combination with the use of these polarizers to block residual probe light, an eight-frame phase cycling scheme consisting of phase cycling and chopping the probe in order to further reduce unwanted pulse interference with the signal.

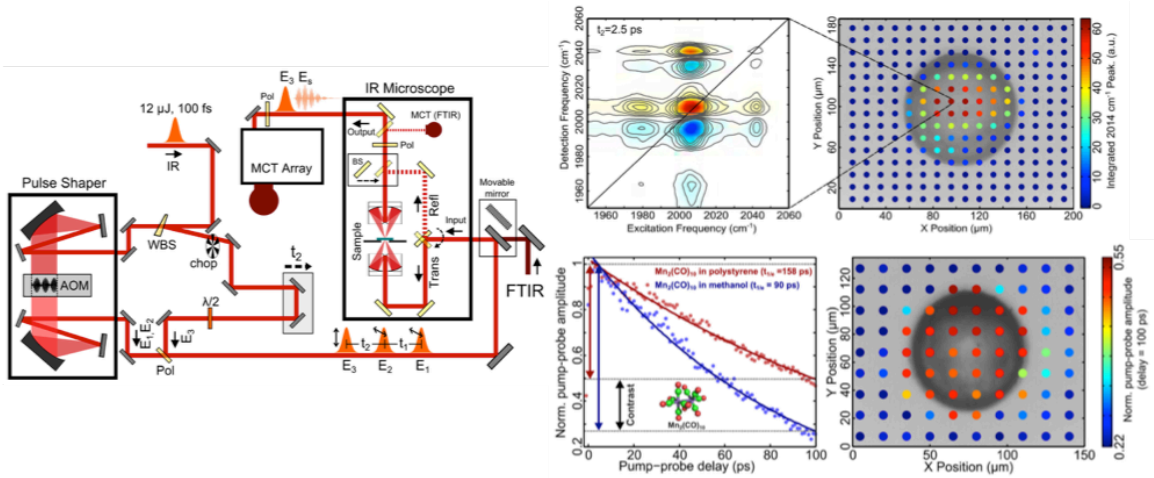

Figure 6.1 2D IR Point-Scanning Microscopy

2D IR point-scanning microscopy implemented by Tokmakoff et al. a. The experimental setup used, including both transmission and reflectance mode and coupling into a Bruker IR microscope. [10]

This method was employed in a proof of concept experiment that imaged a polystyrene bead swelled with a solution of $Mn_2(CO)_{10}$, metal-carbonyl molecules. Through measurement of different vibrational lifetimes they were able to detect the chemical contrast inherent in the different environments of the molecular probe, seen in Figure 6.1. When the metal-carbonyl was in the bulk liquid, it is sampling a fast moving, homogenous environment, which results in a shorter vibrational lifetime. This is then compared with the molecular probe that was adsorbed into the matrix of the polystyrene beads. In this case, the molecular probe is confined in an

inhomogeneous environment, so a variety of static contributions will result in longer vibrational life times. The differences in these different dynamic environments could be probed further using 2D IR waiting time experiments, but are currently confined to vibrational lifetime experiments due to concerns of acquisition times.

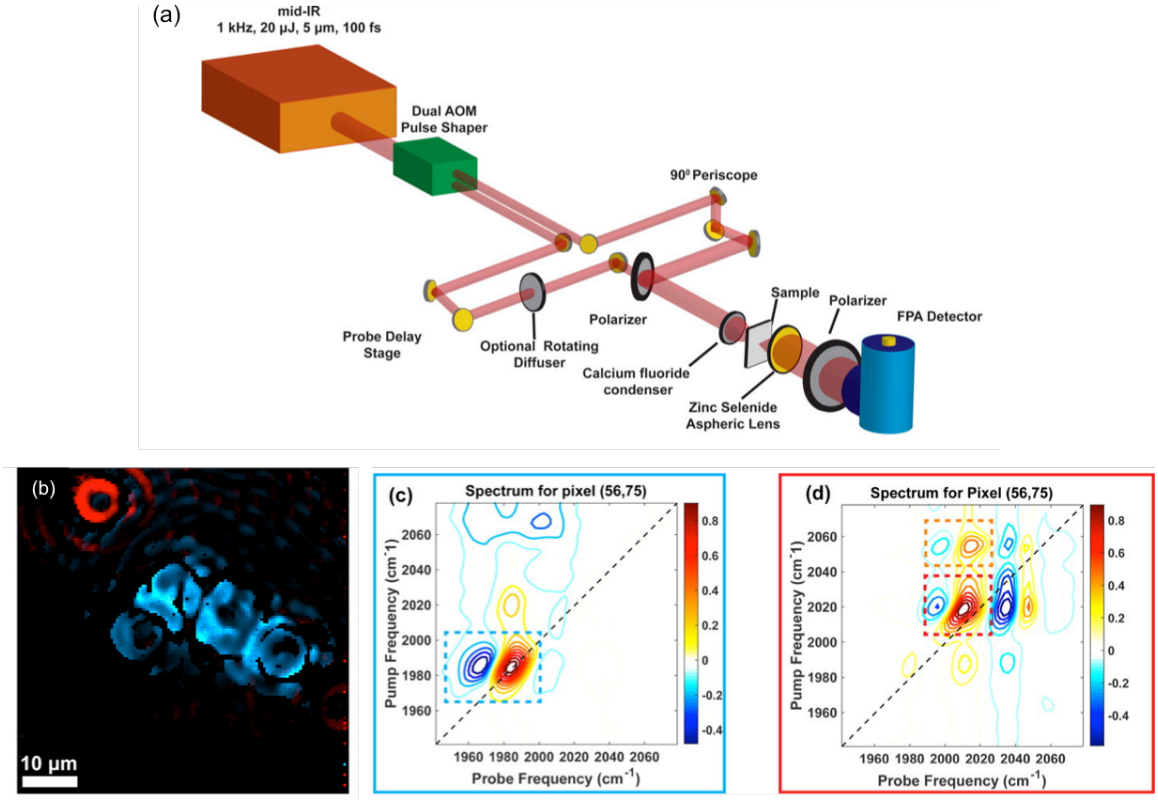

Figure 6.2 2D IR Wide-Field Microscopy

2D IR wide-field microscopy implemented by Zanni et al. a) Depicts the experimental set up. b) The chemical images generated mapping the polystyrene beads with DMDC (red) and WHC (blue). The 2D IR spectra of (c) WHC and (d) DMDS are depicted where the dashed boxes are the features used to generate the image.[11]

In the second implementation of 2D IR microscopy by Zanni et al[11], a wide-field imaging approach was implemented to improve upon spatial resolution and acquisition times associated with having to scan the sample point by point through the focal plane by collecting 16,000 2D IR

spectra simultaneously on a focal plane array detector (FPA), seen in Figure 6.2a. The experimental setup for the wide-field configuration consists of a dual acousto optic modulator (AOM) that is used to generate two sets of pulse pairs from a single OPA in order to perform data acquisition in the time-domain. The probe pulse is on a delay stage controlling the delay of the pump pulses with respect to the two probe pulses. The set of pump pulses undergoes a polarization change so that they are cross-polarized with the probe pulses and can be recombined in the collinear beam geometry using a polarizer. Using a calcium fluoride condenser the two beams are focused to a 100 μm spot size on the sample. A zinc selenide aspheric lens is used after the sample to recollect the pulses and signal and a polarizer is used to discard the pump pulses so the probe and signal can be imaged onto the FPA which resolves approximately 1.1 μm separated spots from the sample on each pixel.

This method was also employed as a proof of concept and characterized by imaging the metal-carbonyl compounds $Mn_2(CO)_{10}$ (DMDC) and $W(CO)_6$ (WHC) on polystyrene beads. The comparison of these two different metal-carbonyl compounds were observed. In the case of DMDC both a diagonal and cross peak pair are apparent in the 2D IR spectrum. However, in WHC only a single lower frequency on diagonal peak pair is present. When constructing the images of the labeled polystyrene beads, it was possible to distinguish the different metal-carbonyls based on these differences in vibrational characteristics.

The 2D IR microscopy work performed by both the Tokmakoff and Zanni groups are important proof of principle developments, however concerns of acquisition time and signal to noise levels need to be addressed to have the microscopy be broadly applied to chemical systems.

6.3 Moving to Higher Repetition Rates

In order for 2D IR microscopy to advance and become as broadly applied as more established microscopy techniques a number of technological advances need to be made for full utility. Acquiring data over an extended sampling area is important in applications of chemical microscopy where correlations of processes are spatially farther separated. Signal to noise that is comparable to 2D IR spectroscopy in the bulk is also important for experiments where information about chemical dynamics is extracted from the spectral shape. In order to perform the waiting time experiments necessary to extract interesting dynamics information, a large number of spectra need to be collected without increasing the measurement time to unfeasible lengths. Improvements in collection time would help to increase utility and address some of these issues. In that vain, there is currently a movement away from the traditional Ti:sapphire based laser systems and optical parametric systems that operate at one to several kHz typically used in 2D IR spectroscopy. By utilizing higher repetition rate sources and utilizing advances in diode pumped ytterbium (Yb) based oscillators and amplifiers[12–15], significant improvements to acquisition rates, shot-to-shot correlation times, and signal-to-noise ratios have been observed.[16,17]

The first implementation of a 100 kHz, mid IR source for use in 2D IR spectroscopy[18,19] and microscopy[20] was performed by Krummel et al using a 100 kHz, mid IR source based on optical parametric chirped-pulse amplification (OPCPA) in magnesium doped periodically poled lithium niobate (MgO:PPLN) and difference frequency generation (DFG) in zinc germanium diphosphide (ZGP), seen in Figure 6.3 and described in detail elsewhere. Briefly, in this system, an All Normal Dispersion (ANDI) Ytterbium-Fiber (Y-Fi) mode locked oscillator is used as the single source for the entire system. The output of the Y-Fi is separated and the majority is

compressed and serves as the pump for an optical parametric oscillator (OPO) generating the 1.68 μm seed for the OPCPA stages. The remainder of the uncompressed Y-Fi output is amplified in the cryogenically cooled, Yb:YAG based regenerative amplifier and two pass amplifier, generating the 1 μm pump for the OPCPA stages. The stretched 1.68 μm seed is amplified in three MgO:PPLN based OPCPA stages and a 2.67 μm idler is generated. These two outputs of the OPCPA stages are compressed and recombined in a ZGP DFG stage to generate the final 3 μJ of 4.65 μm mid-IR output with 220 fs pulse durations that are sent to the 2D IR microscopy experiment.

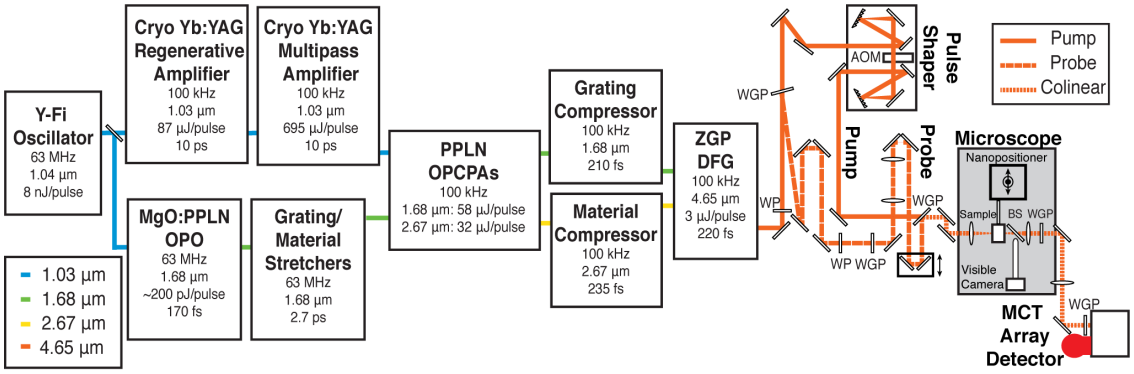

Figure 6.3 100 kHz, 2D IR Microscope Setup
2D IR spectroscopy at 100 kHz implemented by Luther et al.[20] The experimental set up is depicted here.

Another implementation of a 100 kHz mid-IR source was performed by Donaldson et al[17]. This system was based on dual, 100 kHz, Yb:KGW regenerative amplifier and optical parametric amplification (OPA) technology and is described in detail elsewhere. The system consists of two separate Yb:KGW regenerative amplifiers, that are both seeded by the same source. The lower energy amplifier is used to pump two white light continuum seeded OPAs that

separately generate probe pulses that are widely tunable across the wavelength range from 4.5 to 15 μm at pulse energies of 0.2 to 0.3 μJ. The higher energy amplifier is used to pump a third OPA that generates wavelength tunable pump pulse tunable from 4.5 to 10 μm with higher energies between 1.7 and 0.7 μJ, that is sent to a high repetition rate pulse shaper to generate the pump pulse pair.

Characterization of the shot-to-shot stability and the signal to noise ratios achievable with the Yb based regenerative amplification system, indicate that there is significant improvement over the performance of a Ti:sapphire based system. Donaldson et al. observed a root mean square (rms) noise in the measured mid-IR intensity over one second (10^5 laser shots) of approximately 0.15% and a ~10 μOD peak-to-peak noise observed in the probe spectrum after 5 ms (5000 laser shots). These noise measured here is comparable to well optimized 1-10 kHz Ti:sapphire system, but due to the shorter acquisition time, which inherently improves signal to noise up to 10 times over a traditional system. It as also found that these Yb based sources have a higher-degree of long term stability. An analysis and comparison of Yb and Ti:sapphire laser systems was also performed by Zanni et al.[16] by examining 2^{14} laser shots at 651 nm measured at 1 kHz, Figure 6.4a. They directly compared the two laser systems that were at 100 kHz and 1 kHz respectively by only using 1 out of every 100 laser shots in the Yb system. They were able to observe that the Ti:sapphire system has higher noise levels at all frequencies and the correlation between laser shots is longer for Yb than for Ti:sapphire. The long term stability associated with the Yb based systems is therefore greater, and because acquisition time is improved by 10 to 100 times it allows for the data to be collected before the loss of correlation between laser shots begins to occur.

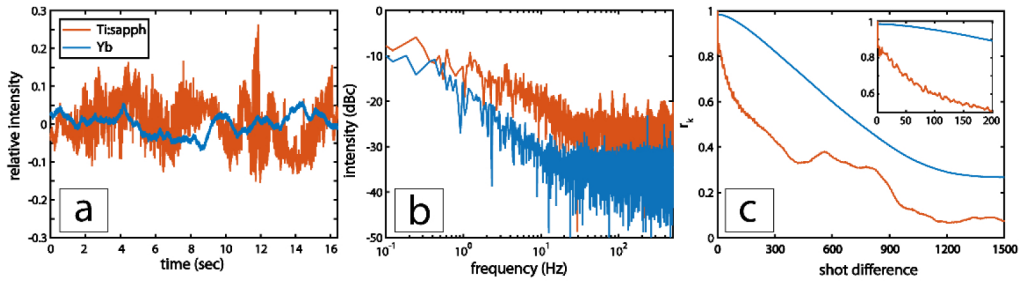

Figure 6.4 Comparison of Yb vs Ti:sapphire Noise

Direct comparison of data on the noise of Yb (blue) and Ti:sapphire (red) based continua at 1 kHz. a) Comparison of relative intensity. b) Fourier transform of 16,384 sequential shots at 651 nm on a log scale. c) Statistical autocorrelation computed for 2^{14} sequential shots.[16]

6.4 Extracting Dynamics Information Using High Repetition Rate Sources

A 2D IR microscopy experiment that spatially resolved, ultrafast chemical dynamics experiment was performed by Krummel et al.[20] using the 100 kHz, mid IR source discussed above, which allowed a fast acquisition rate of 1984 spectral points per minute. They studied a microdroplet formed with the RTIL, 1-ethyl-3-methylimidazolium tetrafluoroborate (EmimBF4) doped with 1-ethyl-3-methylimidazolium tricyanomethanide (EmimTCM), where TCM^- acted as the vibrational probe. A series of waiting time experiments were employed to characterize the chemical dynamics across a RTIL microdroplet in a region of interest, and was able to distinguish the bulk environment, interfacial environment, and an intermediate region between the two environments.

By time resolving the 2D IR microscope image with a series of waiting time, T_w, measurements distinctly different dynamic behavior was observed, including differences in homogeneous and inhomogeneous contributions to the spectral line shape at the bulk and interface of the RTIL microdroplet, seen in Figure 6.5. Significantly faster structural dynamics were observed at the droplet interface when compared to both the bulk and interface of the RTIL

microdroplet, seen in Figure 6.5. Significantly faster structural dynamics were observed at the droplet interface when compared to both the bulk and interior of the microdroplet. It was also found that the dynamics associated with the intermediate region, 5 μm from the interface, was a combination of both the bulk and interfacial dynamics.

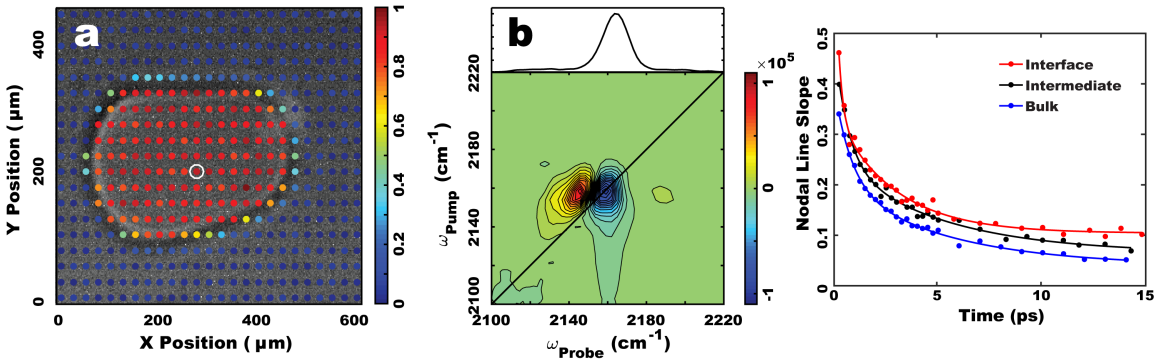

Figure 6.5 100 kHz 2D IR Microscopy Image and Extracted Dynamics

A point-scanning 2D IR microscopy image (a) with a 2D IR spectrum (b) representative of the bulk environment at the position of the white circle in (a). The intensity of points in the 2D IR image are determined by integrating the peak associated with the v=1→2 transition in the corresponding 2D IR spectrum. The third panel shows a comparison of dynamics associated with the bulk environment, the interfacial environment, and the chemical environment between the bulk and interfacial regions. The points are the experimentally measured values and the lines indicate the biexponential fits to the slope decay data extracted.[20]

6.5 Conclusion

The development 2D IR microscopy currently allows for the spatial resolution of time-dependent 2D IR signals to reveal regions of differing chemical structure and dynamics not observable using either FTIR microscopy or 2D IR spectroscopy. These observations of the chemical dynamics associated with a complex chemical system demonstrate the future potential for 2D IR microscopy experiments being used to observe the dynamics and structure in complex heterogeneous systems that are not accessible by other chemical imaging techniques. The

utilization of higher repetition rates is what opened up access to spatially resolving dynamics information. Current detection schemes used in 2D IR spectroscopy and microscopy that require MCT detectors do not allow for higher repetition rates beyond 100 kHz. However, the sources being used have the potential to go beyond 100 kHz. Therefore, using new means of detection such as up-conversion in conjunction with faster detectors may allow to extend the repetition rates beyond 100 kHz, further improving both signal to noise and collection times.

References

(1) Zumbusch, A.; Holtom, G. R.; Xie, X. S. Three-Dimensional Vibrational Imaging by Coherent Anti-Stokes Raman Scattering. *Phys. Rev. Lett.* **1999**, *82* (20), 4142–4145.

(2) Duncan, M. D.; Reintjes, J.; Manuccia, T. J. Scanning Coherent anti-Stokes Raman Microscope. *Opt. Lett.* **1982**, *7* (8), 350–352.

(3) Freudiger, C. W.; Min, W.; Saar, B. G.; Lu, S.; Holtom, G. R.; He, C.; Tsai, J. C.; Kang, J. X.; Xie, X. S. Label-Free Biomedical Imaging with High Sensitivity by Stimulated Raman Scattering Microscopy. *Science* **2008**, *322* (5909), 1857–1861.

(4) Freund, I.; Deutsch, M.; Sprecher, A. Connective Tissue Polarity. Optical Second-harmonic Microscopy, Crossed-beam Summation, and Small-angle Scattering in Rat-tail Tendon. *Biophys. J.* **1986**, *50* (4), 693–712.

(5) Campagnola, P. J.; Millard, A. C.; Terasaki, M.; Hoppe, P. E.; Malone, C. J.; Mohler, W. A. Three-dimensional High-resolution Second-harmonic Generation Imaging of Endogenous Structural Proteins in Biological Tissues. *Biophys. J.* **2002**, *82* (1 Pt 1), 493–508.

(6) Hoffmann, D. M. P.; Kuhnke, K.; Kern, K. Sum-frequency Generation Microscope for Opaque and Reflecting Samples. *Rev. Sci. Instrum.* **2002**, *73* (9), 3221–3226.

(7) Kuhnke, K.; Hoffmann, D. M. P.; Wu, X. C.; Bittner, A. M.; Kern, K. Chemical Imaging of Interfaces by Sum-frequency Generation Microscopy: Application to Patterned Self-assembled Monolayers. *Appl. Phys. Lett.* **2003**, *83* (18), 3830–3832.

(8) Flörsheimer, M.; Brillert, C.; Fuchs, H. Chemical Imaging of Interfaces by Sum Frequency Microscopy. *Langmuir* **1999**, *15* (17), 5437–5439.

(9) Katon, J. E.; Pacey, G. E.; O'Keefe, J. F. Vibrational Molecular Microspectroscopy. *Anal. Chem.* **1986**, *58* (3), 465A–481A.

(10) Baiz, C. R.; Schach, D.; Tokmakoff, A. Ultrafast 2D IR Microscopy. *Opt. Express* **2014**, *22* (15), 18724–18735.

(11) Ostrander, J. S.; Serrano, A. L.; Ghosh, A.; Zanni, M. T. Spatially Resolved Two-Dimensional Infrared Spectroscopy via Wide-Field Microscopy. *ACS Photonics* **2016**.

(12) Chong, A.; Buckley, J.; Renninger, W.; Wise, F. All-normal-dispersion Femtosecond Fiber Laser. *Opt. Express* **2006**, *14* (21), 10095–10100.

(13) Brauch, U.; Giesen, A.; Karszewski, M.; Stewen, C.; Voss, A. Multiwatt Diode-pumped Yb:YAG Thin Disk Laser Continuously Tunable Between 1018 and 1053 Nm. *Opt. Lett.* **1995**, *20* (7), 713–715.

(14) Kawanaka, J.; Yamakawa, K.; Nishioka, H.; Ueda, K. 30-mJ, Diode-pumped, Chirped-pulse Yb:YLF Regenerative Amplifier. *Opt. Lett.* **2003**, *28* (21), 2121–2123.

(15) Akahane, Y.; Aoyama, M.; Ogawa, K.; Tsuji, K.; Tokita, S.; Kawanaka, J.; Nishioka, H.; Yamakawa, K. High-energy, Diode-pumped, Picosecond Yb:YAG Chirped-pulse Regenerative Amplifier for Pumping Optical Parametric Chirped-pulse Amplification. *Opt. Lett.* **2007**, *32* (13), 1899–1901.

(16) Kearns, N. M.; Mehlenbacher, R. D.; Jones, A. C.; Zanni, M. T. Broadband 2D Electronic Spectrometer Using White Light and Pulse Shaping: Noise and Signal Evaluation at 1 and 100 kHz. *Opt. Express* **2017**, *25* (7), 7869–7883.

(17) Donaldson, P. M.; Greetham, G. M.; Shaw, D. J.; Parker, A. W.; Towrie, M. A 100 kHz Pulse Shaping 2D-IR Spectrometer Based on Dual Yb:KGW Amplifiers. *J. Phys. Chem. A* **2018**, *122* (3), 780–787.

(18) Luther, B. M.; Tracy, K. M.; Gerrity, M.; Brown, S.; Krummel, A. T. 2D IR Spectroscopy at 100 kHz Utilizing a Mid-IR OPCPA Laser Source. *Opt. Express* **2016**, *24* (4), 4117–4127.

(19) Tracy, K. M.; Barich, M. V.; Carver, C. L.; Luther, B. M.; Krummel, A. T. High-Throughput Two-Dimensional Infrared (2D IR) Spectroscopy Achieved by Interfacing Microfluidic Technology with a High Repetition Rate 2D IR Spectrometer. *J. Phys. Chem. Lett.* **2016**, *7* (23), 4865–4870.

(20) Tracy, K. M.; Guchhait, B.; Tibbetts, C. A.; Luther, B. M.; Krummel, A. T. Visualizing Chemical Dynamics in an Ionic Liquid Micro-droplet Using Ultrafast 2D IR Microscopy.

Chapter 7

Conclusions/Future Work

7.1 Conclusions

100 kHz, 2D IR spectroscopy and microscopy were both demonstrated for the first time using a source system based on diode pumped Yb gain materials, a three stage MgO:PPLN based OPCPA, and a ZGP DFG stage. An ANDi Yb fiber oscillator serves as the source for both the seed and pump beams of a three stage OPCPA. Part of the ANDi output is used as a seed source for the cryogenically cooled, Yb:YAG regenerative amplifier. This takes advantage of both gain narrowing to remove the need for chirped pulse amplification and the single source to remove the need for electronic timing control for the generation of the OPCPA pump. The OPCPA stages generate short pulses of the seed and idler and DFG between these two pulses in ZGP generates 100 kHz, short, mid-IR pulses at 4.65 μm. Using this high repetition rate, mid-IR source in conjunction 100 kHz pulse shaping and data collection results in millisecond 2D IR spectral acquisition times.

With this high-repetition rate system, it was possible to demonstrate the first successful integration of IR compatible microfluidic device technology with a 2D IR spectrometer in order to accomplish high throughput 2D IR data acquisition. Utilizing microfluidics, the sensitivity of the cyanate vibrational response in mixed solvent environments was efficiently mapped. The results that were found revealed that the vibrational response of the cyanate vibrational probe is sensitive to the details of the local solvent structure surrounding the cyanate anion. This shows

that there is a more complex nature to the mixed solvent environments not taken into account in current studies where cyanate is used to probe complex environments, such as protein dynamics.

The high-repetition rate, mid-IR source also allowed the first demonstration of spatially resolved ultrafast chemical dynamics existing in a RTIL microdroplet. This work presents advances in 2D IR microscopy that provide the opportunity to explore the chemical dynamics in inherently complex environments. 2D IR microscopy experiments were performed across the RTIL microdroplet to investigate the dynamics inherent in different regions of the microdroplet including the bulk environment, interfacial environments, and intermediate regions between the interfacial and the bulk environments. Through a series of waiting time, T_w, measurements the complex nature of the chemical dynamics in RTIL microdroplets was explored, and it was determined that markedly faster structural dynamics occur at the droplet interface in comparison to the bulk or interior of the microdroplet. It was also possible to observe that the dynamics observed in the regions intermediate to the bulk and interfacial environments are a combination of bulk-like dynamics and interfacial-like dynamics and shed light on the long-range effects that exist in these RTIL microdroplets.

Finally, this work as a whole demonstrates the power of using high-repetition rate mid-IR sources for both 2D IR spectroscopy and microscopy. Experiments performed with this source allow for a greater breadth of experiments due to the improved signal to noise and acquisition times when compared to typical 2D IR spectroscopy sources. Interfacing this source with 2D IR microscopy allows for the observation of chemical dynamics in complex environments that are hidden in other chemical imaging techniques.

7.2 Future Work

There are a number of different areas in which this work can be continued. First, there are a number of areas where there is a potential for future improvements of the high-repetition rate mid-IR source. The two greatest limitations of the 100 kHz source currently are the pulse durations that are over 200 fs which prevent the investigation of short timescale dynamics associated with samples such as water; the other limitation is the lack of tunability in the system which greatly limits the samples that can be examined as only a small bandwidth of vibrational frequencies can be probed. The Y-Fi bandwidth supports sub-100 fs pulses; therefore, improvement of compression of this output could improve the pulse durations throughout the whole system. Continuum generation using the 2.67 μm MgO:PPLN idler should allow for tunability and larger output bandwidths from the ZGP DFG in the future.

There is also a wide range of experiments examining different chemical systems that can be performed using the system without any need for further improvements. The studies investigating the dynamics of cyanate in mixed solvent environments in Chapter 4 Section 2 revealed the sensitivity and complex nature of cyanate vibrational response in mixed methanol:DMF solvent environments. In order to continue these studies and investigate the nature of the local solvent environments that give rise to these vibrational dynamics, it would be beneficial to compare both the FTIR and 2D IR results of tetrabutylammonium cyanate in a range of solvent mixtures of DMF and methanol. Using a bulky counter cation, it may be possible to eliminate the shoulder arising from the contact ion pair and investigate whether or not the solvent environment still does not appear additive. This may also help eliminate the static offset seen in the waiting time experiments, and would give information about the cyanate

dynamics without the need to de-convolve the dynamics associated with two peaks that are too close to separate effectively when analyzing the data.

Another pathway to continue this work in the future, is utilizing the 2D IR microscope to investigate a range of complex heterogeneous systems. Current work in the lab is being conducted to probe the dynamics of a liquid electrolyte solution in a working electrochemical cell using an IR probe molecule, methyl thiocyanate. The ultimate goal of this future work would be to spatially resolve dynamics of a cycling battery to provide insight and further understanding of the solid electrolyte interface.

Appendix I

Alignment Procedures

A1.1 Turning on the Laser

1. Check that the pressure on the ion pumps for the regenerative amplifier (regen) and multi-pass amplifier. If either is less than 10^{-6} do not turn on. You will need to pump down the cryohead whose pressure is too high.
2. Turn on the water chiller, the two cryohead chillers, and the dry air (all in the closet).
3. Turn the dry air purging the box on the table
4. Check that the OPO is tracking at 1675 nm,
    a. If it is not tracking, recover with the stage and the Avantes spectrometer
5. Check the stability of the OPO output on the oscilloscope using the photodiode, the standard deviation mean should be less than 2%.
6. Check the temperature of the chiller water circulating through the system on the Arryo Instruments Laser Diode Controller 6340, the temperature should be ~ 16 – 18 C
    a. If 7 is true,
        i. Turn on the two Pockels cells
        ii. Turn on the Pulse Shaper- PhaseTech
        iii. If the red light is on, turn off the pulse shaper immediately
7. Check the temperature of the cryohead, they both should be at ~ -240 C
8. If both 6 and 7 are true then you are free to proceed to turning on the regen.
9. Place the power meter in front of the multi-pass to record the power out of the regen

10. Turn on the regent's fiber pump,
    a. If the S/D light is red – push button for interlock on the timing chip (above the OPO)
11. Turn up the regen pump to 23.6 A (should get out ~ 5.5 W on the power meter)
    a. As you turn this up make sure that the power begins increasing at 10 A. If it does not turn it back to 0A before shutting off.
    b. Wait ~30 minutes for the fiber that is pumping the laser to warm up and record power out of the regen.
12. Move the power meter to the pump line for the 2nd PPLN stage
    a. Do not remove the beam block until the power meter is in place
    b. Check that the waveplate controlling the power being sent to the 3rd PPLN stage is at 146 degrees
    c. Use the 2nd waveplate to maximize power to the power meter
    d. Then use the same waveplate to check minimized power to the 3rd stage by minimizing the green dot on the lollipop
    e. Use the 1st waveplate to check minimized power to the 1st PPLN stage look at green dot on a lollipop until it disappears
13. Turn up the current on the multi-pass until there is 10 W of output measured on the power meter
    a. Use the 2nd waveplate to turn down the power reaching second stage to 1W
    b. Then turn the current up to ~ 41 amps (check the yellow tape for exact value)
    c. Record the daily multi-pass output after waiting ~ 30 min

A1.2 Aligning the PPLN OPCPA Stages

1. Place the long-pass filter (to remove light below1 μm) in front of the 1st stage 1030 nm entrance hole
    a. This is to remove the "halo" when aligning.
2. Using the IR viewer, align to the PPLN 1 irises
    a. Align to the iris right after PPLN 1 with the second mirror on the translation stage and to the iris before PPLN 1 with the mirror right after the box hole.
3. Remove long-pass filter and make sure 100 maw of pump going to first stage
    a. Check back reflection onto the iris in front of PPLN 1
    b. Check that PPLN 1 is on the 3rd period.
        i. Check the green scatter on a card before the first turning mirror after PPLN 1
        ii. Translate the crystal in x and y direction, finding the far edge and then adjusting to the center (there are 5 periods total)
            1. Only ever adjust the side and top knobs NOT the front knob that controls the z direction.
4. Place the power meter in front of the PPLN 1 and adjust power to ~ 650 mW with the waveplate controlling PPLN 1 pump
5. Block everything
6. Put power meter in front of PPLN 2 check that power there is ~ 0 W
    a. Open 1675 nm light (should be ~ 8 - 10 mW)
    b. Open 1030 nm light (should be ~ 60 mW)

c. Use translation stage position to maximize timing and the last 1675 nm mirror before the PPLN to maximize overlap with 1675 nm

d. Record PPLN 1 output and then block pump and 1675 to PPLN 1

7. Turn down the 1030 nm pump going to PPLN 2 from 3 W to 100 mW
8. Using IR viewer to align onto PPLN 2
    a. Align to the iris right after PPLN 2 with the second mirror on the translation stage and to the iris before PPLN 2 with the mirror right after the box hole.
    b. Put power meter back in front of PPLN 2 and turn power of pump to 3.75 W on 1030 nm
    c. Move power meter to after PPLN 3 collimating lenses
    d. Unblock pump and probe to PPLN 1
    e. Unblock pump power to PPLN 2
    f. Use translation stage position to maximize timing and the last 1675 nm mirror before the PPLN 2 to maximize overlap with 1675 nm
    g. Record PPLN 2 output and then block pump and probe for PPLN 1 and 2
9. Using IR viewer to align onto PPLN 3
    a. Using the viewer align the 1675 nm light amplified in PPLN 1 and 2 onto the two irises before and after PPLN 3 with the two turning mirrors for 1675 nm light following PPLN 2
    b. Using the viewer align 1030 nm onto the same two irises used in step 9a with the two mirrors on the translation stage (Check the below bullets FIRST)
        i. Block the 2nd stage with the foam & the 1st stage
        ii. Block 1675 nm with the notecard stand

iii. Minimize the waveplate controlling the 1030 nm light getting to the 3rd stage to 146 degrees.

c. Unblock the 1675 nm probe and 1030 nm pump to the 1st & 2nd stages.

d. Maximize the 1030 nm light being sent to PPLN 3 by adjusting waveplate to 100 from 146 degrees

e. Adjust the translation stage for timing to maximize PPLN 3 output

f. Record PPLN 3 output and then turn the 1030 nm pump down by changing the waveplate position from 100 to 140 degrees

A1.3 Aligning the Compression and ZGP DFG

1. Aligning the 1675 nm light
    a. Place 1 μm long-pass filter after the first turning mirror following PPLN3 & check the back reflection onto the mirror to make sure it is put in straight
    b. Using the IR viewer, align the 1675 nm onto the two compressor irises with the two turning mirrors following PPLN 3.
    c. Remove the long pass filter
    d. Align the 1675 nm onto the translation stage using the two irises before the stage
2. Aligning 2.67 μm light
    a. Turn up the pump power to PPLN 3 (~136 degrees on Waveplate 2)
    b. Using the IR card (the one on the copper block) align into the Si rod with the two 2.67 μm turning mirrors following PPLN 3
    c. Next align using two turning mirrors following the Si rod straight towards the final two turning mirrors before the ZGP

3. Place power meter after the ZGP in front of the 3.6 μm long pass filter (allows light > 3.6 μm through) and block both the 1675 nm and 2.67 μm light
4. Place mount on stage with the ZGP to slide pinhole into beam path
5. Align the 1675 nm light into the onto the pinhole by maximizing the throughput of the 1675 nm light onto the power meter with the final 1675 nm mirror before the ZGP and using the IR viewer to align onto the final iris using the 2nd to last mirror before the ZGP
6. Use the last 2.67 μm mirror to align the 2.67 μm through the pinhole, checking by looking at the power meter for the maximized value.
7. Use the second to last 2.67 μm mirror, and close the iris before the ZGP and the IR card to check that the beam is not being clipped (for 2.67 μm light)
8. Maximize the pump light to PPLN 3 (Turn waveplate 2 to 100 degrees) and then shut the box to let it begin purging.
9. Adjust timing using the translation stage and then adjust the ball drivers to maximize overlap/pointing.
10. Shut box and allow to dry for ~ 1 hour.

A1.4 Aligning the Pump and Probe Beams for the 2D IR Microscope Experiment

1. For the pump line alignment up to the recombination at the wire grid polarizer:
    a. Turn on the pulse shaper:
        i. Set to basic
            1. Amplitude : 0.30 V
            2. Masklength : 8000 s

3. Hit update masks and update AWG

b. Take everything out of the line (wire grid polarizer and turning mirrors that are on magnetic mounts)

c. Switch to small heat sensitive card and turn the first mid-IR waveplate so all the power is sent to the pump line.

d. Align positions coming out of the box using the two mirrors following the pulse shaper

e. Turn down power with first waveplate

f. Align the at the two positions closest to the microscope objective with the two preceding turning mirrors using the card to block and unblock

2. For the probe line alignment up to the recombination at the wire grid polarizer:

a. After drying, repeat timing and pointing adjustment from A1.3 step 9

b. Align the 4.65 μm light coming into the next section of the box along the probe line

i. Using the ball drivers outside the box to check the position close to the box and then the first mirror outside the box to align to the position before the manual translation stage on the probe line.

c. Switch to small heat sensitive card and turn down the first mid-IR waveplate (sending the power to pump line)

d. Using a flash card block and unblock the probe line before the chopper while aligning positions up to the sample

i. Align to the position right after the turning mirror and then before the next set of turning mirrors using a flashlight and align based on the card reflection onto the box wall.

ii. Align the line coming back from the set of turning mirrors right after the chopper (be sure not to use the sharpie line for the card, instead place on the row of holes closer).

e. Check that the line going to the parabolic mirror is aligned and then place polarizer back in place

f. Align the at the two positions closest to the microscope objective with by moving the wire grid polarizer stage and pointing

A1.5 Overlapping the Pump and Probe Beams at the Sample

1. Looking at the visible microscope, using the LabView Program, MicroscopeLabviewe.vi
2. Block everything and then place the heat sensitive card into the sample holder to align the pump & probe in same spot
    a. Align pump first:
        i. Use the waveplate to adjust maximum light to the probe
        ii. Put the visible beam splitter in
        iii. Hit: start camera on the LabView code
        iv. Change scale on graph to see better
        v. Use the flashlight to illuminate from behind the sample
        vi. Look for bright ring on screen

vii. Center cursors on the ring

b. Then block and begin aligning the probe:

i. Put the OD 1 Mid IR filter in

ii. Make sure waveplate adjusted to the pump line

iii. Use flashlight to light from behind the sample

iv. Unblock

v. Look for bright spot on the graph

vi. If not overlapped with the cursors from the pump then adjust the (removable) polarizer for alignment

3. Remove the heat sensitive card and replace with the pinhole to align with the HeNe beam

a. Illuminate from behind with flashlight

b. Focus the HeNe through the pinhole center

c. Stop the camera

4. Place the power meter behind the pinhole – put on the shorter base

a. Adjust the waveplate to the pump line

b. Change the X and Y positions in increments of 10 (then 5) to maximize the power seen on the power meter

c. Repeat with the probe line, adjusting the polarizer & waveplates to maximize, not the stage position

5. Fill the MCT detector with liquid nitrogen

6. Maximize IR light into the pump line with the first mid-IR waveplate

7. Turn on the FPAS

8. Open the LabView Program Single Pixel 2D Spectrometert.vi
    a. Initialize the FPAS and load the startup.txt configuration file on the desktop
    b. Initialize iHR320
    c. Set the spectrometer parameters
        i. Grating 1
        ii. Stage at zero
        iii. Entrance: front
        iv. Entrance slit: 0.25 mm
        v. Exit: front
        vi. Exit Slit: 0.00
        vii. Desired wavelength: 4650 nm
        viii. Wavelength step: 1.000
        ix. Hit send command (do this twice)
    d. On scan Controls hit start scan
9. Check probe alignment
    a. Place silicon lens after the pinhole
    b. Use the magnetic mirror after the lens to check alignment
    c. Adjust mirror going into the spectrum looking at the program
    d. Block the probe
    e. Insert waveplate before the light hits the detector
    f. Minimize, then add 45 to waveplate position
10. Find time zero using fringes
    a. Unblock both pump and probe

b. Move stage far off zero position and take background

c. Use interferometer to scan and look at fringes

d. Find time zero and reset stage position to 250 fs off time zero

11. Insert the two waveplates before the spectrometer to minimize pump beam.

A1.6 Calibration Procedure for the FPAS

1. Samples: first make a sample of 50 mM KOCN in DMF with 10% acetonitrile
    a. Make the sample LMR1 with 100 μm spaces
    b. Put in 100 μL of solution in
2. Take an FTIR of the sample and record the position of the three peaks, one associated with the acetonitrile and the peak and shoulder associated with the KOCN in DMF
3. Using the 64 element calibration program with in the LabView Program Single Pixel 2D Spectrometert.vi
    a. First take the spectrum of the probe pulse with no sample
    b. Then put in the sample and retake the spectrum
    c. Then using these two spectra you are able to calibrate by assigning the different peaks with the values obtained in the FTIR
    d. Save the 64 element calibration

A1.7 Turning off the Laser

1. Turn off the FPAS
2. Turn off the dry air to the table
3. Turn waveplate controlling the pump for PPLN 3 to 146 degrees

4. Block the pump for PPLN 2
5. Block the pump for PPLN 1
6. Block the 1675 nm light for PPLN 1
7. Turn down the current pumping the multi pass amplifier
8. Turn down the current pumping the regen amplifier
9. Turn off both Pockles cells
10. Turn off the pulse shaper
11. Turn of the water chiller, the two cryohead chillers, and the dry air (all in the closet).

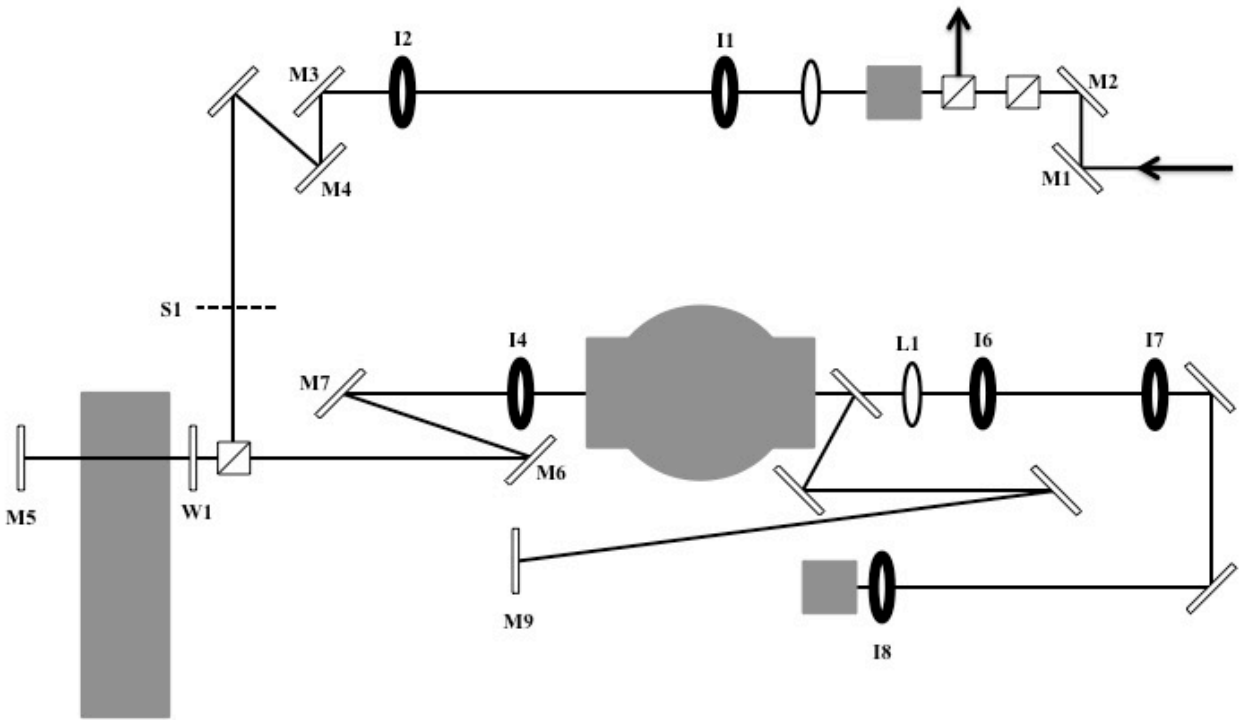

Figure A1.1 Regenerative Amplifier Setup

A1.8 Alignment of the Regenerative Amplifier

1. Align the seed beam onto the irises I1 and I2 using mirrors M1 and M2 (designations are from Figure A1.1.
    a. Sometimes it is easier to see if you put a card to block the beam after M4.
2. Align the seed beam back onto iris I1 in the other direction using M5
    a. May need to change the waveplate W1 so you can see it.
3. Check that pump is going onto I8 and then put in I7 and I6 irises.
4. Align pump onto I7 and I6 irises using M8 and M7 mirrors (may need to close down I8 to see on I7).
    a. Then close I8 so you only see on Iris 6 without it being closed
5. Use L1 to put pump onto I4 (close down I7 and check it is still aligned on I6 first)
6. Use mirrors M6 and M7 to get seed onto I4 and I7 irises
    a. To see seed through I7 irises put a card behind the irises and look for it going through
    b. After this check that the seed is still going through I6
7. Use M9 to send seed back to I1 iris
8. Check lasing threshold by putting lollipop at spot S1 and turning up pump until you see green.
    a. Before doing this remove I6 and I7
    b. Use M9 and M5 to maximize the signal and decrease lasing threshold, also use L1 to maximize
        i. Iterative processes of stepping with M5 and scanning M9 for the maximum in both x and y direction.

9. Make sure I2 iris is closed down enough to catch back reflection
10. Check output of regenerative amplifier
    a. Can tweak M2 slightly to maximize seed pointing into cavity.

A1.9 Alignment of the Multi Pass Amplifier

1. Turn the waveplate after the exit of the regenerative amplifier from 340 to 300 degrees
2. Use the two mirrors following the second Pockels cell to align onto the two irises following them using the IR viewer to view the beams.
3. Place a card at position in multi pass after the big lens and before the waveplate.
4. Use two mirrors before the cryohead to align onto the two irises before the cryohead
5. Remove card and check in the other direction onto the first iris before the cryohead using the mirror after the cryohead.
6. Align to the two irises leading to the waveplates that separate the PPLN pump lines using the two mirrors before them.
7. Partially close the final iris before the waveplates controlling the pump to the PPLN stages
8. Turn the waveplate back to 340
9. Check all irises are open
10. Close the box

1.10 Abridged Alignment Procedure for the OPCPA and DFG Stages

1. Make sure the waveplate controlling the PPLN 3 pump is at 146 degrees
2. Place the power meter in front of PPLN 1
3. Adjust the power to ~ 650 mW using the 1st waveplate

4. Block everything
5. Put power meter in front of PPLN 2
    a. Open 1675 nm light
    b. Open 1030 nm light to first stage
    c. If low on power meter use timing to maximize
    d. Record power
6. Block all and open pump to PPLN 2
7. Using the waveplate controlling pump to PPLN 2, turn power to 3.75 W
8. Put power meter after PPLN 3
9. Unblock power to the first stage (1675 nm first) then second stage
10. Block 1030 nm to the 3rd stage
11. Record power meter reading
12. Place the power meter after the second turning mirror after PPLN 3
13. Using IR viewer to align onto PPLN 3
    a. Using the viewer align the 1675 nm light amplified in PPLN 1 and 2 onto the two irises before and after PPLN 3 with the two turning mirrors for 1675 nm light following PPLN 2
    b. Using the viewer align 1030 nm onto the same two irises used in step 9a with the two mirrors on the translation stage (Check the below bullets FIRST)
        i. Block the 2nd stage with the foam & the 1st stage
        ii. Block 1675 nm with the notecard stand
        iii. Minimize the waveplate controlling the 1030 nm light getting to the 3rd stage to 146 degrees.

c. Unblock the 1675 nm probe and 1030 nm pump to the 1st & 2nd stages.

d. Maximize the 1030 nm light being sent to PPLN 3 by adjusting waveplate to 100 from 146 degrees

e. Adjust the translation stage for timing to maximize PPLN 3 output

f. Record PPLN 3 output

14. Place the power meter after ZGP

15. Close box

16. Let purge for ~1 hour

17. Adjust the timing using the translation stage and position with ball drivers outside of the box

A1.11 Collecting 2D IR of Microfluidics

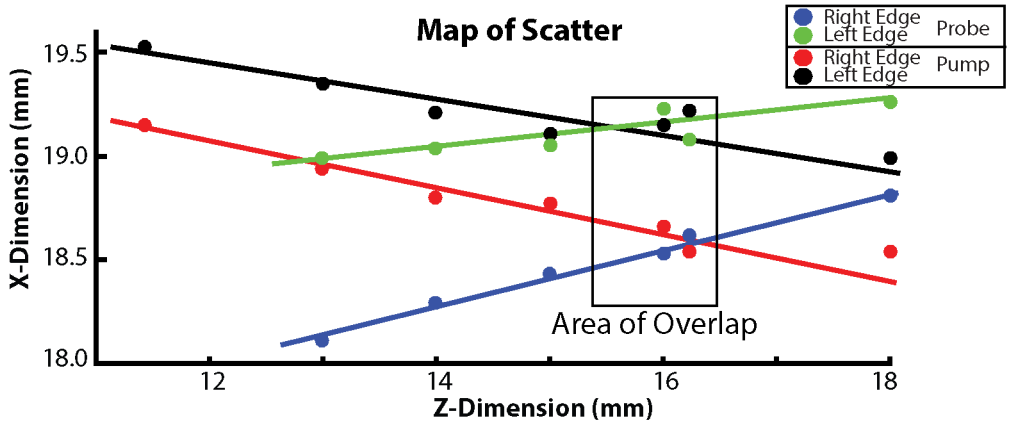

Figure A1.2 Mapping Area of Pump Probe Overlap in a Microfluidic Device

1. The graph above charts the positions of the sample stage when scatter is observed off of the channel wall for both the pump and probe beams used to find the area of overlap.

2. After getting laser system up and aligned to the sample holder put pinhole that is fitted with microfluidic device into sample holder
3. Find position of probe beam maximized through the 100 μm pinhole and then find the probe beam maximized through the pinhole at that z-location.
4. Guide pump through pinhole at new probe position using the final mirror into the parabolic.
5. Put actual microfluidic device with 50 mM KOCN in methanol going through it.
6. Using the linear spectrum transmitting through the device, find the x positions where the pump and probe beams are on the channel edges.
7. Repeat step 5 at steps of z axis of 0.25 mm until you find z position where the two edges of the pump and probe overlap (see Figures A1.2)
8. Use the center between the two edges at this z constant as your new x position.
9. Keeping x and y position constant and collect 2D IR with four phase cycling, 100 spectra average, 0.7 volts on the pulse shaper, and 7 fs steps out to 2499 fs with 358 delays
    a. Do this while stepping z position in 0.01 mm steps to find where 2D IR looks best
        i. In example shown in figures this was ~ 0.1 mm from the z found in method above
10. Check increasing amplitudes on pulse shaper for best signal
11. Begin flowing both fluids and begin collecting
    a. Collected across the channel while flowing both fluids at 9 μL/min

b. Slightly faster flow rate was better to minimize bubbles, which interfered with signal.

Appendix II

MATLAB Programs

A2.1 MATLAB Program Used to Plot 2D IR Spectra

This example code is for plotting a 2D IR spectrum that was previously Fourier transformed and saved in LabView. In this example, a rotating frame of 2000 cm^{-1} was utilized. A calibration file for the probe wavelength axis is also imported from LabView.

Plot2DIR.m

```
clear all, close all, clear hold

Data1= importdata('240 um xxxx'); %Import FT file saved in LabView
WL= importdata('64 array calibration'); %Import WL calibration file saved in LabView

WN=10000000./WL; %convert to Wavenumbers

%generating the diagonal line
x = linspace(min(WN),max(WN),1000);
y = x;

RotatingFrame=(Data1(2,:))+2000; %Adjust for Rotating Frame, if none set to '+0'
PumpAxis=RotatingFrame(1,:);

figure ()
TData=Data1(3:66,:)'.*-1;
hold on
contourf(WN,PumpAxis,TData,25) %Changing the number on the end will change the number
of contours
plot(x,y,'k','LineWidth',2)
hold off
set(gca,'YDir','normal')
ylim([2100,2220])
xlim([2100,2220])
zlim([-20000 20000])
colormap(jet)
```

```
axis square
box on
% title('30 mM KOCN in Methanol 0 fs')
xlabel('\omega_{Probe} (cm^{-1})')
ylabel('\omega_{Pump} (cm^{-1})')
```

A2.2 MATLAB Program Used to Extract CLS Data

This example code is for extracting a slice of the 2D IR spectrum that was previously Fourier transformed and saved in LabView. The slice is extracted and then fit using another MATLAB program seen in A2.2.1 and the information is input to this program to create the center line slope curve.

Plot2DIR_CLS.m

```
clear all, close all, clear hold

Data1= importdata('XXXX 4 ps'); %Import FT file saved in LabView
WL= importdata('64 array calibration'); %Import WL calibration file saved in LabView

WN=10000000./WL; %convert to Wavenumbers

%generating the diagonal line
x = linspace(min(WN),max(WN),1000);
y = x;

RotatingFrame=(Data1(2,:))+2000;%Adjust for Rotating Frame, if none set to '+0'
PumpAxis=RotatingFrame(1,:);

TData=Data1(3:66,:)'*-1;

figure ()
hold on
contourf(WN,PumpAxis,TData,25) %Changing the number on the end will change the number
of contours
plot(x,y,'k','LineWidth',2)
hold off
set(gca,'YDir','normal')
ylim([2100,2220])
xlim([2100,2220])
```

```
zlim([-20000 20000])
colormap(jet)
axis square
% box on
% title('30 mM KOCN in Methanol 0 fs')
xlabel('\omega_{Probe} (cm^{-1})')
ylabel('\omega_{Pump} (cm^{-1})')

%% Taking Slices

z=550;
slices(1,1:64)=TData(z,:)';
norm_slices(1,:)=(slices(1,:))./abs(min((slices(1,1:37)))); %make sure you
%are using the same peak to normalize, so region of the positive peak

hold on
%figure()
plot(WN,norm_slices(1,:));


Slice_Meth0ps(1,:) = WN;
Slice_Meth0ps(2,:) = norm_slices(1,:);
dlmwrite('SliceMeth0ps.asc', Slice_Meth0ps)

%% Max points of negative peak fit
%plotting what has been determined to be the positive peak position of the
%different slices from the fitting code: fitting.m


points_cls(:,1)=PumpAxis(1,544:549);
points_cls(:,2)=[2158.85 2157.91 2158.22 2160.22 2163.25 2165.72]';


figure ()
hold on
%Changing the number on the end will change the number of contours
contourf(WN,PumpAxis,TData,25)
plot(points_cls(:,2),points_cls(:,1),'k','LineWidth',2)
hold off
set(gca,'YDir','normal')
ylim([2100,2220])
xlim([2100,2220])
zlim([-200000 200000])
colormap(jet)
axis square
% box on
```

```
% title('Benzo carb+ring 9fs step')
xlabel('\omega_{Probe} (cm^{-1})')
ylabel('\omega_{Pump} (cm^{-1})')

%% Linear Fit of Max Points
clear x; clear y;
x=points_cls(:,2);
y=points_cls(:,1);
p = polyfit(x,y,1) %p(1) is the slope and p(2) is the intercept of the linear predictor
yfit =  p(1) * x + p(2) %the fit equation
yresid = y - yfit; %Compute the residual values as a vector of signed numbers
SSresid = sum(yresid.^2); %Square the residuals and total them to obtain the residual sum of
squares
SStotal = (length(y)-1) * var(y); %Compute the total sum of squares of y by multiplying the
variance of y by the number of observations minus 1
rsq = 1 - SSresid/SStotal %Compute R2

figure ()
hold on
plot(points_cls(:,2),points_cls(:,1),'k','LineWidth',2)
plot(x,yfit,'r','LineWidth',2)
hold off
axis square
xlabel('\omega_{Probe} (cm^{-1})')
ylabel('\omega_{Pump} (cm^{-1})')

figure()
hold on
contourf(WN,PumpAxis,TData,25)
%plot(x,y,'k','LineWidth',2)
plot(x,yfit,'k','LineWidth',2)
hold off
set(gca,'YDir','normal')
ylim([2100,2220])
xlim([2100,2220])
zlim([-200000 200000])
colormap(jet)
axis square
xlabel('\omega_{Probe} (cm^{-1})')
ylabel('\omega_{Pump} (cm^{-1})')
%% %% Calculating CLS

slope=(1/p(1)) %Plot this for each Tw and fit to exponential, this CLS plot is equal to the
normalized Tw-dependent portion of the FFCF
%% Plotting CLS
```

```
Time(:,1)= [0.2500 0.5000  0.7500  1.0000  1.2500  1.5000  1.7500  2.0000  2.2500  2.5000
2.7500  3.0000  3.2500  3.5000  3.7500  4.0000  4.2500  4.5000  5.0000];
Slope(:,1)=[0.4875 0.4802  0.4644  0.3848  0.3839  0.3650  0.3073  0.2794  0.3466  0.3693
0.3786  0.3169  0.2755  0.2809  0.2479  0.2052  0.1907  0.1998  0.2197]';

figure()
plot(Time,Slope,'b')
xlabel('Time (ps)')
ylabel('Slope')

CLS(1,:) = Time;
CLS(2,:) = Slope;
dlmwrite('CLSfit.asc', CLS);
```

A2.2.1 MATLAB Program Used to Fit Slices Used for CLS

This example code is for fitting a slice of the 2D IR spectrum that was previously Fourier transformed and saved in LabView. This same program is also used to fit FTIR spectra with Gaussian or lorentzian curves, and was adapted from a code written by Dr. Amber Krummel. The SubVIs used are seen in sections A2.2.2.

Fitting.m

```
clear all; close all;
%% Importing Data
FTIR = importdata('SliceMeth0ps.asc')';

plot(FTIR(:,1), FTIR(:,2))
%% peak fitting

    clear hold;
    format long e; % this should prevent any truncating of these values or rounding to get more
exact values
    E01 = 2140; %peak location (eigen energy)
    E02 = 2160;
    E03 = 0;
    gamma1 = 20; %FWHM
    gamma2 = 20;
    gamma3 = 0;
    height1 = 0.99;
    height2 = -0.99;
```

```
height3 = 0;
offset = 0.01; %vertical offset from baseline
variable_hold = [1 1 0 0 0 0 0 0 0 1]; %lets the values for E, gamma, and height to be
altered with the fit, but holds the vertical offset to zero
            %[1 2 3 1 2 3 1 2 3 x]
shape = 'g'; %will fit the peak with a Gaussian

x = FTIR(:,1);  absorp = FTIR(:,2);

fitFTIR2

E01 = par(1); E02 = par(2); E03 = par(3);
gamma1 = par(4); gamma2 = par(4); gamma3 = par(6);
height1 = par(7); height2 = par(8); height3 = par(9);
offset = par(28); %replaces my estimates for each parameter with those found in the fit

if shape=='l'
   y1 = lorenz(x, gamma1, E01, height1, offset);
   y2 = lorenz(x, gamma2, E02, height2, offset);
   y3 = lorenz(x, gamma3, E03, height3, offset);
   y4 = lorenz(x, gamma4, E04, height4, offset);
   y5 = lorenz(x, gamma5, E05, height5, offset);
   y6 = lorenz(x, gamma6, E06, height6, offset);
   y7 = lorenz(x, gamma7, E07, height7, offset);
   y8 = lorenz(x, gamma8, E08, height8, offset);
   y9 = lorenz(x, gamma9, E09, height9, offset);
else
   y1 = gauss1(x, gamma1, E01, height1, offset);
   y2 = gauss1(x, gamma2, E02, height2, offset);
   y3 = gauss1(x, gamma3, E03, height3, offset);
   y4 = gauss1(x, gamma4, E04, height4, offset);
   y5 = gauss1(x, gamma5, E05, height5, offset);
   y6 = gauss1(x, gamma6, E06, height6, offset);
   y7 = gauss1(x, gamma7, E07, height7, offset);
   y8 = gauss1(x, gamma8, E08, height8, offset);
   y9 = gauss1(x, gamma9, E09, height9, offset);
end


%       grid on
```

A2.2.2 MATLAB Program SubVI for Fitting FTIR

This example code is for fitting a slice of the 2D IR spectrum that was previously Fourier transformed and saved in LabView. This same program is also used to fit FTIR spectra with

Gaussian or lorentzian curves, and was adapted from a code written by Dr. Amber Krummel. The SubVIs used are seen in section A2.2.2.

fitFTIR2.m

```
%This is used to fit linear spectra

x0=[E01,E02,E03,gamma1,gamma2,gamma3,height1,height2,height3,offset];

clear fhold
clear fpar
s=0;
for k=1:length(variable_hold)
   if (variable_hold(k)==1)
      s=s+1;
      fpar(s)=x0(k);
      fhold(k)=-1;
   else
      fhold(k)=x0(k);
   end
end

options(1)=1;
options(14)=4000;

xx=fminsearch('subFTIR2',fpar,options,[],fhold,x,absorp,shape,0);

s=0;
s=0;
for k=1:length(fhold)
   if (fhold(k)==-1)
      s=s+1;
      par(k)=xx(s);
   else
      par(k)=fhold(k);
   end
end

clear fhold
clear fpar
s=0;
for k=1:length(variable_hold)
   if (variable_hold(k)==1)
      s=s+1;
```

```
      fpar(s)=par(k);
      fhold(k)=-1;
   else
      fhold(k)=par(k);
   end
end

subFTIR2(fpar,options,fhold,x,absorp,shape,0)
par
```

subFTIR2.m

```
%This is a subroutine used in fitting linear spectra

%function out=DNAsub(fpar,hold,x,K42smooth,shape,graph)
function out=DNAsub(fpar,options,hold,x,absorp,shape,graph)


s=0;
for k=1:length(hold)
   if (hold(k)==-1)
      s=s+1;
      par(k)=fpar(s);
   else
      par(k)=hold(k);
   end
end

E01=par(1);
E02=par(2);
E03=par(3);
gamm1=par(4);
gamm2=par(5);
gamm3=par(6);
height1=par(7);
height2=par(8);
height3=par(9);
offset=par(10);

%s=0;
%for k=x
%s=s+1;
%y(s)=lorenz(n,gamma,E0,height,offset);
%%y(s)=gauss(n,gamma,E0,height,offset);
%end
```

```
if (shape=='l')
   y1=lorenz(x,gamm1,E01,height1,offset);
   y2=lorenz(x,gamm2,E02,height2,offset);
   y3=lorenz(x,gamm3,E03,height3,offset);
else
   y1=gauss1(x,gamm1,E01,height1,offset);
   y2=gauss1(x,gamm2,E02,height2,offset);
   y3=gauss1(x,gamm3,E03,height3,offset);
end

if (graph==0)
%x=1580:2.5:1680;
figure(85)
plot(x,absorp,x,y1,'--',x,y2,'--',x,y1+y2,'--',x,absorp-y1-y2,'--')%
legend('linear absorption','fit1','fit2','total fit','Difference')
xlim([2100 2220])
ylim([-0.01 1.1])
axis tight

%absint=sum(K37GCPRS(:,2)*absheight-absoffset)
areafit=sum(y1);
%stop
%ratio=lorint/absint
%fitint=sum(y-(K37GCPRS(:,2)*absheight-absoffset))
%plot(x,K37GCPRS(:,2)*absheight-absoffset,x,y,'--')
%title('DNA in D2O, absorption spectrum fit to a lorentzian')
%legend('linear absorption','fit')
end

out=sum((y1+y2+y3-absorp).^2);
%out=sum((y1+y2-K42smooth).^2);
%out=sum(y'-(K37GCPRS(:,2)*absheight-absoffset)).^2);
```

lorenz.m

```
function out2=lorenz(x,gamma,wo,height,offset)

out2=gamma/2/pi*(1./((x-wo).^2+gamma^2/4))*height+offset;
```

gauss1.m

```
function yval=mgauss(x,gamm,E0,height,offset)
gamm=gamm/(2*sqrt(2*log(2)));
height=height;%/30; % just so has same peak intensity as lorentzian
yval=height*exp(-(x-E0).^2/(2*(gamm)^2))+offset;
```

A2.2.3 MATLAB Program Fitting Exponential Decay of CLS

This example code is for fitting the exponential decay of the CLS data points extracted in Plot2D_CLS. This program was adapted from the code fitting.m written by Dr. Amber Krummel.

fitting_exponential.m

```
%% Importing Data
CLS = importdata('CLSfit.asc');

plot(CLS(1,:),CLS(2,:))

%% peak fitting

    clear hold;
    format long e; % this should prevent any truncating of these values or rounding to get more exact values
    Delta_omega1 = 0.529; %linewidth (sigma) in *radians* / ps !
    Delta_omega2 = 0.144;
    tau1 = 1.41; % correlation time in ps
    tau2 = 11.84;
    offset = 0.274; %vertical offset from baseline
    variable_hold = [0 1 0 1 0]; %lets the values for Delta_omega and tau to be altered with the fit, but holds the vertical offset
                %[1 2 1 2 1]
    shape = 'e'; %will fit the peak with a biexponential

    x=CLS(1,:);  absorp = (CLS(2,:));

fitFTIRexponential

    Delta_omega1 = par(1);  Delta_omega2 = par(2); tau1 = par(3); tau2 = par(4); offset = par(5); %replaces my estimates for each parameter with those found in the fit

    y1 = ((Delta_omega1)*exp(-x/tau1))+((Delta_omega2)*exp(-x/tau2))+offset;

    xlim([0,40])
    ylim([0.2,0.6])
    xlabel('Time (ps)')
    ylabel('CLS')
```

```
%      grid on
```

A2.2.3 MATLAB SubVIs for Fitting Exponential Decay of CLS

These example codes are the SubVIs for fitting the exponential decay of the CLS data points extracted in Plot2D_CLS.

fitFTIRexponential.m

```
%This is used to fit exponential curves

x0=[E01,E02,E03,E04,E05,E06,E07,E08,E09,gamma1,gamma2,gamma3,gamma4,gamma5,gam
ma6,gamma7,gamma8,gamma9,height1,height2,height3,height4,height5,height6,height7,height8
,height9,offset];

clear fhold
clear fpar
s=0;
for k=1:length(variable_hold)
   if (variable_hold(k)==1)
      s=s+1;
      fpar(s)=x0(k);
      fhold(k)=-1;
   else
      fhold(k)=x0(k);
   end
end

options(1)=1;
options(14)=4000;

xx=fminsearch('subFTIRexponential',fpar,options,[],fhold,x,absorp,shape,0);

s=0;
s=0;
for k=1:length(fhold)
   if (fhold(k)==-1)
      s=s+1;
      par(k)=xx(s);
   else
      par(k)=fhold(k);
   end
end
```

```
clear fhold
clear fpar
s=0;
for k=1:length(variable_hold)
   if (variable_hold(k)==1)
      s=s+1;
      fpar(s)=par(k);
      fhold(k)=-1;
   else
      fhold(k)=par(k);
   end
end

subFTIRexonential(fpar,options,fhold,x,absorp,shape,0)
par
```

subFTIRexponential.m

```
%This is a subroutine used in fitting exponential curves

function out=subFTIRexponential(fpar,options,hold,x,absorp,shape,graph)


s=0;
for k=1:length(hold)
   if (hold(k)==-1)
      s=s+1;
      par(k)=fpar(s);
   else
      par(k)=hold(k);
   end
end

E01=par(1);
E02=par(2);
E03=par(3);
E04=par(4);
E05=par(5);
E06=par(6);
E07=par(7);
E08=par(8);
E09 =par(9);
gamm1=par(10);
gamm2=par(11);
gamm3=par(12);
```

```
gamm4=par(13);
gamm5=par(14);
gamm6=par(15);
gamm7=par(16);
gamm8=par(17);
gamm9=par(18);
height1=par(19);
height2=par(20);
height3=par(21);
height4=par(22);
height5=par(23);
height6=par(24);
height7=par(25);
height8=par(26);
height9=par(27);
offset=par(28);

%s=0;
%for k=x
%s=s+1;
%y(s)=lorenz(n,gamma,E0,height,offset);
%%y(s)=gauss(n,gamma,E0,height,offset);
%end
if (shape=='e')
   y1=exponential(x,gamm1,E01,height1,offset);
   y2=exponential(x,gamm2,E02,height2,offset);
   y3=exponential(x,gamm3,E03,height3,offset);
   y4=exponential(x,gamm4,E04,height4,offset);
   y5=exponential(x,gamm5,E05,height5,offset);
   y6=exponential(x,gamm6,E06,height6,offset);
   y7=exponential(x,gamm7,E07,height7,offset);
   y8=exponential(x,gamm8,E08,height8,offset);
   y9=exponential(x,gamm9,E09,height9,offset);
else
   y1=gauss1(x,gamm1,E01,height1,offset);
   y2=gauss1(x,gamm2,E02,height2,offset);
   y3=gauss1(x,gamm3,E03,height3,offset);
   y4=gauss1(x,gamm4,E04,height4,offset);
   y5=gauss1(x,gamm5,E05,height5,offset);
   y6=gauss1(x,gamm6,E06,height6,offset);
   y7=gauss1(x,gamm7,E07,height7,offset);
   y8=gauss1(x,gamm8,E08,height8,offset);
   y9=gauss1(x,gamm9,E09,height9,offset);
end

if (graph==0)
```

```
%x=1580:2.5:1680;
figure(85)
plot(x,absorp,x,y1,'--',x,y2,'--',x,y1+y2+y3+y4+y5+y6+y7+y8+y9,'--')
legend('linear absorption','fit1','fit2','total fit')%,'fit4','fit5','fit6','fit7','fit8','fit9')
axis tight

%absint=sum(K37GCPRS(:,2)*absheight-absoffset)
areafit=sum(y1);
%stop
%ratio=lorint/absint
%fitint=sum(y-(K37GCPRS(:,2)*absheight-absoffset))
%plot(x,K37GCPRS(:,2)*absheight-absoffset,x,y,'--')
%title('DNA in D2O, absorption spectrum fit to a lorentzian')
%legend('linear absorption','fit')
end

out=sum((y1+y2+y3+y4+y5+y6+y7+y8+y9-absorp).^2);
%out=sum((y1+y2-K42smooth).^2);
%out=sum(y'-(K37GCPRS(:,2)*absheight-absoffset)).^2);
```

exponential.m

```
function out2=lorenz(x,gamma,wo,height,offset)

out2=(height*exp(x/gamma))+offset;
```

A2.3 MATLAB Program Used to Plot 2D IR Microscope Image

This example code is for plotting a 2D IR microscope image with the 2D IR intensity data overlaid with the bright field image. Each 2D IR spectrum is individually imported and the sum of intensity over three slices is recorded. This is then input into an excel file for all of the points on the 2D IR microscope image. This intensity data is then reimported and plotted with the bright field image.

Plot2DIRMicro.m

```
% clear all, close all, clear hold

Data1= importdata('Full Scan_1_ 1_7_ _300X_ _200Y_ft','\t'); %Import FT file saved in
```

```
LabView
WL= importdata('64 array calibration'); %Import WL calibration file saved in LabView

WN=10000000./WL; %convert to Wavenumbers

%generating the diagonal line
x = linspace(min(WN),max(WN),1000);
y = x;

RotatingFrame=(Data1(2,:))+1982; %Adjust for Rotating Frame, if none set to '+0'
PumpAxis=RotatingFrame(1,:);

figure ()
TData=Data1(3:66,:)'.*-1;
hold on
contourf(WN,PumpAxis,(TData./500),25) %Changing the number on the end will change the
number of contours
plot(x,y,'k','LineWidth',2)
set(gcf,'renderer','Painters')
hold off
set(gca,'YDir','normal')
ylim([2100,2220])
xlim([2100,2220])
zlim([-20000 20000])
colormap(jet)
axis square
box on
% title('30 mM KOCN in Methanol 0 fs')
xlabel('\omega_{Probe} (cm^{-1})')
ylabel('\omega_{Pump} (cm^{-1})')
%% Integrating over the probe axis from 2124 to 2151 cm^-1 taking 3 slices on pump axis at
2154, 2159, 2163
close all

figure()
plot(WN,(TData(551,:)-TData(551,1)));
IData1=TData(551,22:34)-TData(551,1);
SumData1=sum(IData1);

figure()
plot(WN,(TData(552,:)-TData(552,1)));
IData2=TData(552,22:34)-TData(552,1);
SumData2=sum(IData2);

figure()
plot(WN,(TData(550,:)-TData(550,1)));
```

```
IData3=TData(550,22:34)-TData(550,1);
SumData3=sum(IData3);

TotalSum=SumData1+SumData2+SumData3

%% %% Plot Intensity as 3D Scatter Plot

Bead2 = importdata('IntensityData2.xlsx');
xvector = Bead2(:,1);
yvector = Bead2(:,2);
C = Bead2(:,3);

figure ()
hold on
scatter(xvector,yvector,125,C,'filled')
hold off
colormap(jet)
ylim([-10,460])
xlim([-10,610])
xlabel('X Position (\mum)')
ylabel('Y Position (\mum)')
zlabel('Integrated Diagonal Peak (a.u.)')
%% Plot Brightfield Image

Data2 = importdata('img2')';

xscale = [0:1:1279].*1.875;
yscale = [0:1:959].*1.875;

figure ()
hold on
imagesc(xscale,yscale,Data2)
hold off
colormap(gray)
ylim([222,692])
xlim([255,875])
xlabel('X Position (\mum)')
ylabel('Y Position (\mum)')
zlabel('Integrated Diagonal Peak (a.u.)')
%% Plot of Brightfield with Scatter Overlayed
figure ()
hold on
imagesc(xscale,yscale,Data2)
scatter(xvector,yvector,200,(C./max(max(C))).*20,'filled')
hold off
colormap(jet)
```

```
% ylim([150,750])
% xlim([130,730])
xlabel('X Position (\mum)')
ylabel('Y Position (\mum)')
zlabel('Integrated Diagonal Peak (a.u.)')
%% Plot Intensity Image

Bead=importdata('Bead1_080917_data.xlsx');

%x-axis
xax=[-200:20:200];

%y-axis
yax=fliplr([-100:20:200]);%because in the excel file we start with 200 on top and go down to -
100

figure ()
hold on
imagesc(xax,yax,Bead)
hold off
colormap(jet)
ylim([-100,200])
xlim([-200,200])
xlabel('X Position (\mum)')
ylabel('Y Position (\mum)')
zlabel('Integrated Diagonal Peak (a.u.)')
%% 549
Data4= importdata('spot1_1_ 1_7__Analyzed').*-1;
TData4=Data4(3:66,:)';
Data5= importdata('spot50_1_ 1_7__Analyzed').*-1;
TData5=Data5(3:66,:)';

plot(WN,TData4(549,:),WN,TData5(549,:))

%clim)
```

Appendix III

Chapter 4 Supplemental Materials

The layout of the 2D IR spectrometer, and 2D IR spectra of static samples, and tunability of the gradients in the microfluidics devices are included in the supporting information.

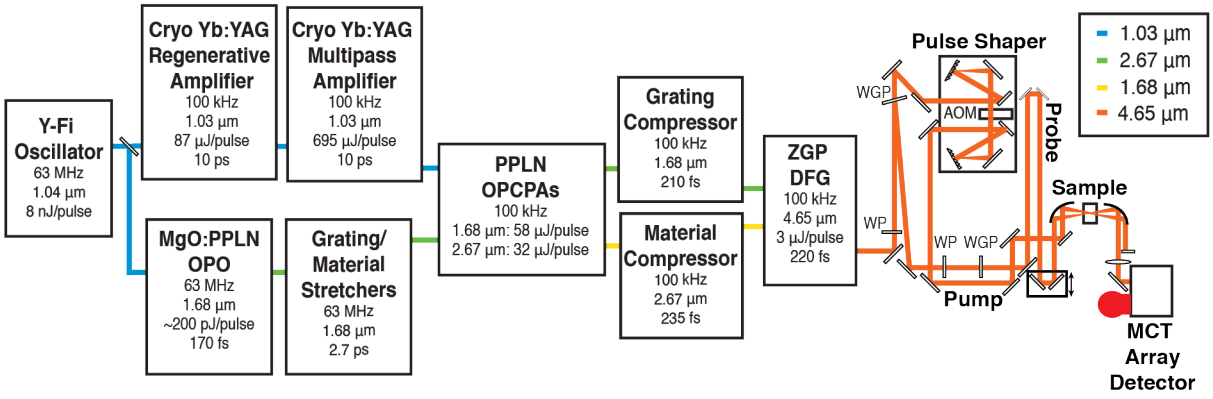

Figure S4.1 The General Layout of the 2D IR Spectrometer

The plots presented in Figure S4.2 show the relationship between the total flow rates or ratio of flow rates and the concentrations of the fluids at each point across the channel in the serpentine device. All flow rates are in units of µL/min and the channel is 300 µm across. The intensity is found by flowing sodium fluorescein and water in the channel and collecting fluorescence microscopy images in order to generate the intensity profiles across the channel. The intensity profiles represent the concentration of the two fluids at each point across the device. Alpha, α, is the ratio of flow rates between stream 1 and stream 2. At α=1, the flow rates in the two streams are equal and the 2 fluids meet in the center of the channel and have an

equal concentration change on both sides. As the total flow rate decreases the slope of the lines following the intensities decrease as well, which indicates the gradient spanning more of the device laterally. When the flow rates have an alpha = 3, the slope of the lines on each side have roughly the same slope; however, as total flow rate increases the meeting point of the 2 lines shifts farther to one side of the channel. This characteristic allows for one fluid to reside in a larger percentage of the channel than the other. It is expected that the tunability of the gradient generator shown here will be maintained, so long as the fluids are fully miscible and the viscosity contrast between the fluids is less than 10.[1]

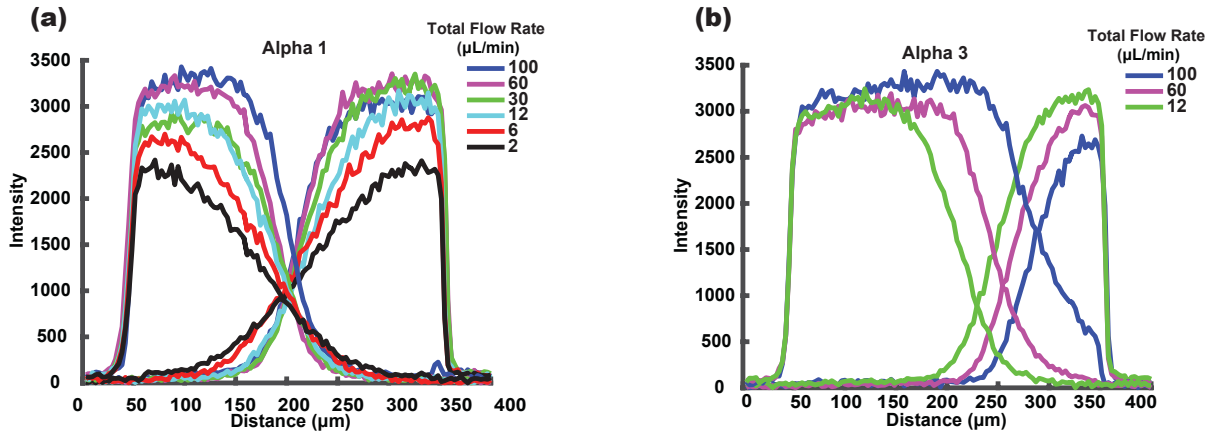

Figure S4.2 Characterization of Gradient Generation on Chip

(a)For alpha = 1, the gradient across the channel is even and as flow rate decreases the gradient widens. (b) For alpha = 3, the gradient shifts closer to one side of the channel as total flow rate increases. This allows one fluid to be more abundant in the channel.

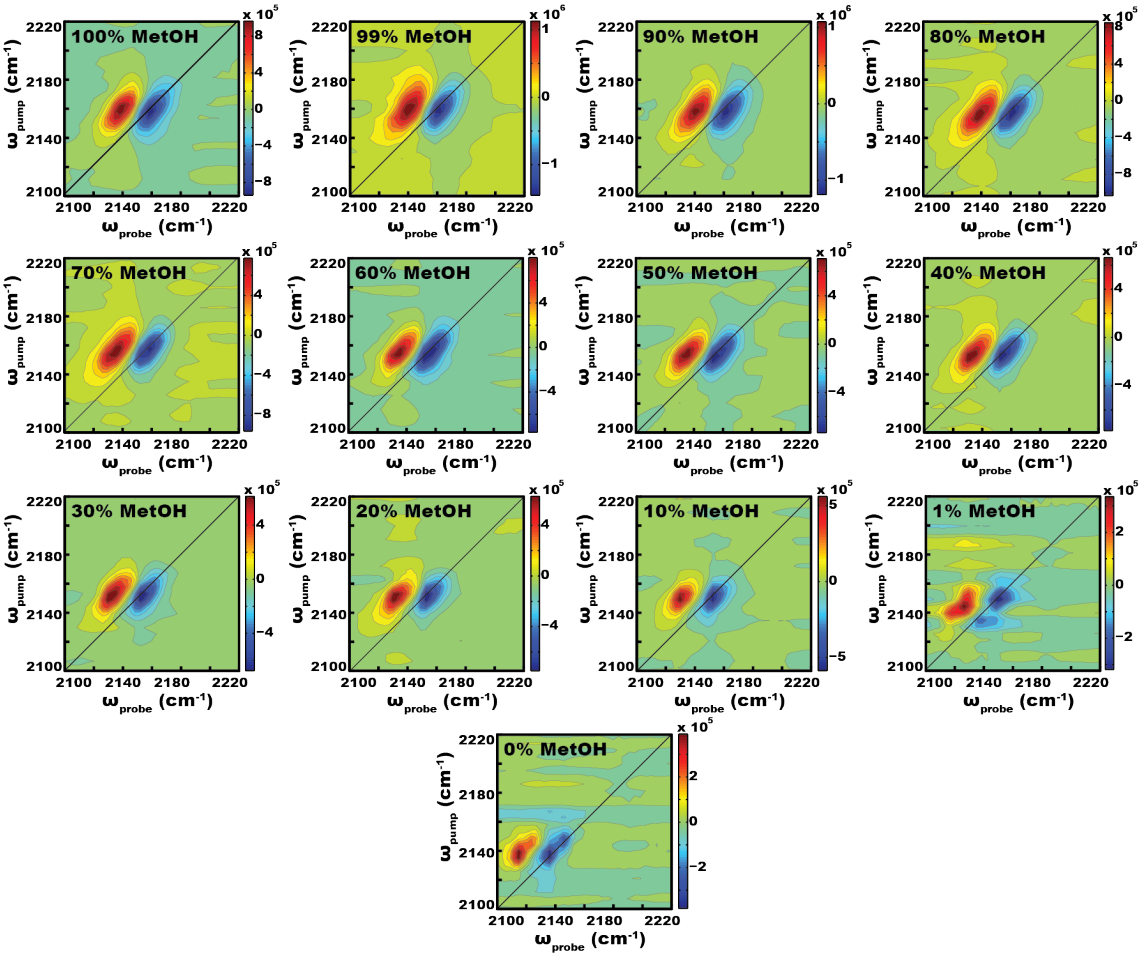

Figure S4.3 2D IR Spectra of KOCN in Static Sample For Comparison

2D IR spectra of KOCN in a range of mixed solvent environments collected in a static sample cell.

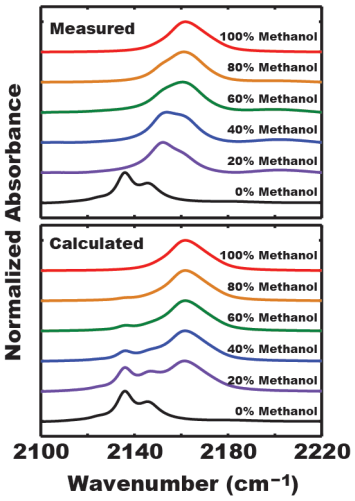

Figure S4.4 Calculated vs Measured FTIR of KOCN in a Range of Solvent Mixtures

The measured FTIR of 50 mM KOCN moving from 100% methanol to 100% DMF are compared to the calculated FTIR expected. The optical densities of the samples ranged from OD = 0.10 to 0.56, depending on the solvent environment.

References

(1) Sudarsan, A.P., Ugaz, V.M. Multivortex Micromixing. *PNAS* **2006**, *103*, 7228 – 7233.

Chapter 5 Supplemental Materials

The supplemental information includes details of sample preparation and details of the 2D IR microscopy experiments used in this work.

S5.1 Experimental Methods

S5.1.1 Sample Preparation

The samples utilized in both the 2D IR and FTIR microscopy experiments were RTIL microdroplets in silicon oil. The droplets consisted of 1-ethyl-3-methylimidazolium tetrafluoroborate ($EmimBF_4$) and 1-ethyl-3-methylimidazolium tricyanomethanide (EmimTCM) RTILs. The EmimTCM is doped into the EmimBF4 in a 1:500 volume ratio where TCM^- acts as a vibrational probe. The dimethyl silicone oil was obtained from Thomas Scientific, SF96/50. $EmimBF_4$ and EmimTCM (Iolitec) were dried under vacuum for 24 hours. All experiments were performed at room temperature; the samples were placed between two CaF_2 plates using 50-μm or 100-μm thick Teflon spacers. A roughly spherical droplet is formed when a very small amount of RTIL (10-20 nL) is casted in silicon oil. The droplet becomes a pancake in shape when placed in between two CaF_2 substrates. The oil is used for stabilization of the RTIL microdroplet as well as removing scatter from the interface because the refractive index of the silicon oil is similar to the RTIL microdroplet.

A Bruker Hyperion 3000 FTIR microscope was used to take the FTIR chemical image. It utilizes a 64 x 64 element FPA detector and a 15x objective to give a 7.6 x 7.6 μm^2 spatial resolution. The FTIR microscope image was taken in transmission mode and was processed using OPUS software (Bruker Optics).

S5.2 2D IR Microscopy

The 2D IR microscopy was performed with a 100 kHz, mid-IR source based on optical parametric chirped-pulse amplification (OPCPA) in magnesium doped periodically poled lithium niobate (MgO:PPLN) and difference frequency generation (DFG) in zinc germanium diphosphide (ZGP), which generates 3 μJ of 4.65 μm mid-IR output with 220 fs pulse durations. This source has been described in previous work.[34]

The 2D IR microscope is detailed in Figure 1. The IR output is split into two lines using a λ/2 waveplate and wire grid polarizer. The polarizer reflects the probe pulse whose polarization is rotated by 90°, creating S-polarization. The P-polarized pump line passes through the polarizer and is sent to a high speed, mid-IR pulse shaper to generate the pump pulse pair with a variable delay at 100 kHz. The pump and probe pulses are recombined using a polarizer that transmits the pump pulses and reflects the probe pulse to create a collinear geometry where 2D IR data is collected in the cross polarization (XXYY) configuration. The three pulses are focused into the sample by a Ge/Si achromatic lens and then re-collimated using a Si lens and sent to the detector. The spot size was measured by scanning a 10 μm pinhole in the X and Y direction at the focal plane and recording the integrated intensity. The full width at half maximum (FWHM) beam diameter was measured to be 19.5 μm in the Y direction and 14.2 μm in the X direction. The Rayleigh range of focus in the direction of propagation is approximately 140 μm. The two polarizers before the detector are used to block the pump pulses and transmit the probe and signal. The probe and signal fields are then passed through a monochromator and collected on a 1x64 element, mercury cadmium telluride (MCT) linear array detector operating at the speed limit of detection of 100 kHz. A 100 lines/mm grating was used in the monochromator. Considering the physical dimensions of the monochromator, MCT element dimensions, and the

gratings, the resolution along the probe axis (ω_{probe}) of the 2D IR spectra collected is 3.3 cm^{-1}. The 2D IR spectra were all collected using a series of 510 pump pulse pairs delayed from 0 to 3.57 ps in 7 fs steps. Thus, the spectral resolution along the pump-axis (ω_{pump}) is 4.7 cm^{-1}. Spectra were acquired using a four-step phase cycling scheme with 2000 cm^{-1} rotating frame for background and scatter removal. The full 2D IR microscopy image of the RTIL microdroplet, shown in Figure 2a, is comprised of a data set of 476 2D IR spectra fully averaged 500 times. The pulse energies utilized were 70 nJ/pulse.

The sample was held in a lens mount, which has been mounted to a 2-axis translational stage. Control of the position of the sample in the direction of propagation is obtained by controlling the Ge/Si lens position with a manual stage. The sample position across the focusing area in the X and Y direction is controlled by a nanopositioner and two micropositioners (Nano-3D200 and MMP, Mad City Labs Inc.) with a 200 μm range of motion and a 25 mm range of motion, respectively. To collect the 450 μm x 600 μm image seen in Figure 2a, 25 μm steps were taken in the X and Y directions. The step size utilized is much larger than the resolution of the stages; the nanopositioner has 1 nm resolution and the micropositioner has 50 nm resolution and repeatability of less than 100 nm. A bright field image of the sample was collected using a visible beam splitter and a 2x imaging lens to project the image onto a visible camera. We correlated the position of the bright field image with the position at which the 2D IR spectra are collected by maximizing the IR throughput of the probe and pump beams through a pinhole at the focal plane. We then imaged the pinhole onto the visible camera and utilized the pinhole location as the location of our 2D IR collection. Under these conditions the image seen in Figure 2a was acquired in 120 minutes; thus, producing an acquisition rate of 1984 individual 2D IR spectra per minute.

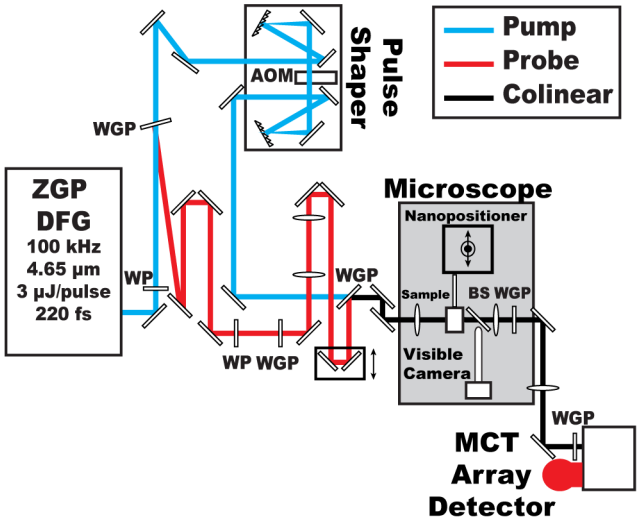

Figure S5.1 2D IR Microscope Setup

Block Diagram of the 100 kHz repetition rate 2D IR spectrometer and microscope.

List of Abbreviations

Abbreviations	Full Name
2D IR	**Two-dimensional infrared**
3D IR	**Three-dimensional infrared**
ANDi	**All Normal Dispersion**
AOM	**Acousto-optic modulator**
AWG	**Arbitrary waveform generator**
CaF_2	**Calcium fluoride**
CLS	**Center line slope**
CPA	**Chirped pulse amplification**
d_{eff}	**Effective nonlinear coefficient**
DFG	**Difference frequency generation**
DMDC	**Dimanganese decacarbonyl**
DMF	**Dimethylformamide**
Emim BF_4	**1-ethyl-3-methylimidazolium tetrafluoroborate**
EmimTCM	**1-ethyl-3-methylimidazolium tricyanomethanide**
FFCF	**Frequency frequency correlation function**
FOD	**Fourth order dispersion**

Abbreviations	Full Name
FROG	Frequency resolved optical gating spectroscopy
FTIR	Fourier transform infrared
FWHM	Full width half max
GaSe	Gallium Selenide
GDD	Group Delay Dispersion
GVD	Group velocity dispersion
HHG	High harmonic generation
KOCN	Potassium Cyanate
MCT	Mercury cadmium telluride
MgO:PPLN	Magnesium doped periodically poled lithium niobate
mid-IR	Mid-infrared
OCN-	Cyanate
OD	Optical density
OPA	Optical parametric amplification
OPCPA	Optical parametric chirped pulse amplification
OPG	Optical parametric generation
OPO	Optical parametric oscillator
PPLN	Periodically Poled Lithium Niobate
PDMS	Polydimethyl Siloxane

Abbreviations	Full Name
SCN^-	Thiocyanate
$SeCN^-$	Selenocyanate
TCM^-	Tricyanomethanide
TOD	Third order dispersion
SNLO	Select Nonlinear Optics
RTILs	Room temperature ionic liquids
VSFG	Vibrational sum frequency generation
WGP	Wire grid polarizer
WHC	Tungsten hexacarbonyl
WP	Wave plate
Y-Fi	Ytterbium-Fiber
Yb	Ytterbium
Yb:YAG	Yb:Yttrium aluminum garnet
ZGP	Zinc Germanium Phosphide